Hermann Edlbauer, BSc

Chemical Defects and Charge-Injection Barriers at Metal / Organic Semiconductor Interfaces

---

Master's Thesis

to achieve the university degree

Diplom-Ingenieur

Master's degree programme: Technical Physics

submitted to

Graz University of Technology

Supervisor:

Dipl.-Ing. Dr.techn. Oliver Hofmann
Institute of Solid State Physics

Co-Supervisor:

Ao.Univ.-Prof. Dipl.-Ing. Dr.techn. Egbert Zojer
Institute of Solid State Physics

Graz, September 2015

Affidavit

I declare that I have authored this thesis independently, that I have not used other than the declared sources/resources, and that I have explicitly indicated all material which has been quoted either literally or by content from the sources used. The text document uploaded to TUGRAZonline is identical to the present master‘s thesis dissertation.

Date

Signature

Acknowledgement

Especially I would like to thank my supervisors, Oliver Hofmann and Egbert Zojer, who guided and supported my work. Further I'd like to thank Shashank Harivyasi, Elisabeth Wruss, Thomas Taucher and the other members of Egbert Zojer's group for helpful discussions. Philipp Hermann (Humboldt Universität zu Berlin, Germany) supported me with very useful information regarding *ab initio* thermodynamics. Funding by the EU Marie Curie Actions ITN THINFACE (FP7/2007-2013/607232) is gratefully acknowledged. The computational results presented have been achieved using the Vienna Scientific Cluster (VSC). A part of the calculations have been performed using the D-cluster of the scientific computing department at Graz University of Technology.

Abstract

The efficiency of organic electronic devices is strongly affected by charge-injection barriers at the interface of the organic semiconductor and the metal electrode. One approach for the reduction of charge-injection barriers is based on the modification of the work function of the metal contact by adsorbing a monolayer of deliberately chosen organic molecules undergoing charge-transfer reactions. However, small particles such as hydrogen can diffuse to this charge-injection layer and electrochemically react with the adsorbate leading to chemical defect formation. Here we investigate how successive introduction of such chemical defects affects the work function, Φ, and the transport levels of the overlying adsorbate, which determine charge-injection barriers. We describe the system via density functional theory (DFT), which proved to be powerful tool for the simulation of many-body-systems containing hundreds of atoms and model the interface by the well-established repeated slab approach. In particular we consider a monolayer of the molecule tetrafluoro-1,4-benzoquinone (TFBQ) adsorbed on (111)-surfaces of coinage metal electrodes. In these layers chemical defects of the species tetrafluoro-1,4-benzenediol (TFBD) are introduced via electrochemical reaction with hydrogen. To motivate the choice of the organic adsorbate, first we compare the physical properties of TFBQ and TFBD to other possible species. We then proceed with a study of the limiting cases of homogeneous adsorbates, where the surface is either fully covered by TFBQ or TFBD to understand the adsorption mechanisms present. Employing a supercell approach we then investigate mixed monolayers with gradually increased fractions of chemical defects. In this context we analyze two factors affecting charge-injection barriers: The work function, Φ, and in the electron-potential, $U(\vec{r})$, in the immediate vicinity of the surface. For full coverage of TFBQ we find a strong increase in Φ, whereas for TFBD we observe a decrease. The changes of work-function modification, $\Delta\Phi$, with varying mixing ratio extend over an energy range of 1 eV. Furthermore, we observe that the introduction of TFBD strongly affects the electron-potential above the adsorbate with a maximum corrugation of 0.2 to 0.4 eV for TFBD fractions of 12.5 % and 87.5 %. Employing *ab initio* thermodynamics, we finally show that the TFBD fraction and, thus, the effects on charge-injection barriers can be continuously tuned via pressure control of a surrounding hydrogen gas phase.

Kurzfassung

Die Effizienz von Organischer Elektronik wird wesentlich durch Ladungsinjektionsbarrieren an den Grenzflächen der Metalle und organischen Halbleiter beeinflusst. Eine Methode zur Verringerung jener Barrieren basiert auf der Modifikation der Austrittsarbeit der Metallelektrode durch Adsorption einer Monolage sorgfältig ausgewählter organischer Moleküle die zu Ladungsübertragungsreaktionen führen. Jedoch kann es dazu kommen, dass Atome oder Moleküle wie Wasserstoff an die Grenzfläche der Metallelektrode und des organischen Halbleiters diffundieren und dort mit dem Adsorbat chemisch reagieren, was zu Defekten in der Ladungsinjektionsschicht führt. Hier untersuchen wir wie die sukzessive Einbringung solcher chemischer Defekte die Ladungsinjektionsbarrieren beeinflusst, welche näherungsweise durch die Differenzen der Fermi-Energie, E_F, zu den Energien der Transportniveaus des organischen Halbleiters bestimmt sind. Wir beschreiben das System mittels Dichtefunktionaltheorie (DFT), die sich als mächtiges Werkzeug zur Simulation von Vielteilchensystemen erwiesen hat, die auch hunderte von Atomen beinhalten können. Insbesondere betrachten wir eine Monolage des Moleküls Tetrafluoro-1,4-Benzochinon adsorbiert auf (111)-Oberflächen von Münzmetall-Elektroden, in weche chemische Defekte der Spezies Tetrafluoro-1,4-Dihydroxybenzol durch elektrochemische Reaktion mit Wasserstoff eingebracht werden. Um die Wahl des organischen Adsorbats zu motivieren, werden wir hier erst die physikalischen Eigenschaften von TFBQ und TFBD mit anderen möglichen molekularen Spezies vergleichen. Anschließend wenden wir uns den Grenzfällen von homogenen Adsorbaten zu, bei denen die Oberfläche entweder voll mit TFBQ oder mit TFBD bedeckt ist, um die jeweils vorliegenden Adsorptions-Mechanismen zu verstehen. Mittels Superzellen untersuchen wir schließlich gemischte Monolagen mit graduell ansteigendem Anteil an chemischen Defekten und analysieren zwei Faktoren, welche Ladungsinjektionsbarrieren beeinflussen: Die Austrittsarbeit, Φ, und das Elektronen-Potential, $U(\vec{r})$, überhalb des Adsorbats und Adsorbens. Für die volle Bedeckung mit TFBQ finden wir eine starke Erhöhung von Φ, wogegen wir für TFBD eine Verminderung beobachten. Die Bereiche der errechneten Austrittsarbeitsmodifikationen, $\Delta\Phi$, erstrecken sich über einen Energiebereich von 1 eV mit variierendem Mischungsverhältnis. Des Weiteren finden wir, dass die Einführung von TFBD auch $U(\vec{r})$ überhalb der Oberfläche stark beeinflusst, mit einem maximalen ”Berg-Tal-Gefälle”von 0.2 bis 0.4 eV bei TFBD Konzentrationen von 12.5 % und 87.5 %. Schließlich zeigen wir mittels *ab initio* Thermodynamik, dass der TFBD Anteil und somit der Effekt auf Ladungsinjektionsbarrieren mittels Druckkontrolle einer umgebenden Wasserstoff-Gas-Phase kontinuierlich eingestellt werden kann.

Contents

List of Abbreviations

BD	1,4-benzenediol
BQ	1,4-benzoquinone
CIL	charge-injection layer
DFT	density functional theory
DOS	density of states
e	elementary charge, $\mathrm{e} \approx 1.60 \cdot 10^{-19}$ As
EA	electron affinity
E_F	Fermi energy
f	fraction of TFBD molecules in a mixed monolayer
fcc	face-centered-cubic
FHI-*aims*	Fritz Haber Institute *ab initio* molecular simulations
GGA	generalized gradient approximation
h	Planck's constant, $\mathrm{h} \approx 6.63 \cdot 10^{-34}$ Js
HB	hydrogen bond
HOMO	highest occupied molecular orbital
HOPS	highest occupied π-states
IP	ionization potential
k_B	Boltzmann constant, $\mathrm{k}_B \approx 1.38 \cdot 10^{-23}$ J/K
LCAO	linear combination of atomic orbitals
LDA	local density approximation
LUMO	lowest unoccupied molecular orbital
LUPS	lowest unoccupied π-states
MML	mixed monolayer
MODOS	density of states projected on molecular orbitals
PBE	Perdew-Burke-Ernzerhof
PTCDA	3,4,9,10-perylene-tetracarboxylic-dianhydride
PQ	6,13-pentacenequinone
PT	5,7,12,14-pentacenetetrone
SCF	self-consistent field
θ	sub-monolayer coverage of a surface
TCNE	tetracyanoethylene
TFBD	tetrafluoro-1,4-benzenediol
TFBQ	tetrafluoro-1,4-benzoquinone
VASP	Vienna *Ab Initio* Simulation Package
vdW	van der Waals
VL	vacuum level
XC	exchange-correlation
ZORA	zero order relativistic approximation

Remark of the Author: Some results of this thesis led to the manuscript "*Post*-Adsorption Work Function Tuning via Hydrogen Pressure Control" – see Edlbauer et al. [1] –, which was written in close collaboration with my supervisors Oliver Hofmann and Egbert Zojer. Sections containing contents of this manuscript are explicitly indicated at the headline via footnotes.

1 Introduction[1]

With their rise in electronics, organic semiconductors became an important topic of recent research. The processablitly of those semiconductors from solutions makes organic electronic devices cheap, adaptable and even flexible. In form of light emitting diodes (OLED), photovoltaic devices (OPV) and thin film transistors (OTFT) they already entered the market. But the performance of organic electronic devices is strongly diminished by certain factors. One of those is the charge-injection / extraction efficiency at the interface of a metal electrode and an organic semiconductor – compare Wöll [2, chapter 11.2]. Similar to a Schottky contact with inorganic semiconductors, charge-injection barriers are built up at those interfaces, which exponentially affect the current density – compare Peng et al. [3]. The extent of those barriers can be approximated by the offset between the Fermi energy, E_F, and the transport levels, which nearly match the lowest unoccupied and highest occupied molecular orbitals (LUMO and HOMO) of the organic material for electron and hole transport.

A reduction of charge-injection barriers can be accomplished by adjusting the work function of the electrode, Φ [4]. To this aim, several strategies have been developed, including the deposition of thin layers of alkali-halides [5, 6], alkali/alkaline earth metals [7, 8], ultrathin oxide films [9, 10] or dipolar self-assembled monolayers [11–15]. Another particular promising approach is the deposition of organic molecules undergoing charge-transfer reactions [16, 17]. This method bears the advantage of allowing for continuous Φ-tuning by choosing the coverage of the adsorbed organic (sub-) monolayer [18, 19]. Employing this approach, enhancements of electro-luminance and power efficiency, as well as lower operating voltages were reported for OLEDs [20].

However, for such an electrode with organic adsorbate undergoing charge-transfer reactions it has to be expected that small molecules as hydrogen can diffuse to the interface. By operation or just thermal activation those molecules can react chemically with the organic adsorbate and form chemical defects. The changes in

---

[1] This section contains contents of Edlbauer et al. [1, Section 1, Introduction].

the adsorbate layer then affect Φ as well as the LUMO and HOMO of the overlying organic layers and, thus, are crucial for charge-injection at the interface.

In this work we investigate the introduction of chemical defects via hydrogenation of monolayers of acenequinones adsorbed on the coinage metal surfaces Cu(111) and Ag(111). The electron accepting character of this organic species results from the quinoid-to-aromatic transition acting as driving force for charge transfer [21]. Upon adsorption on coinage metal surfaces, they induce pronounced increases in Φ [22]. In particular we focus on the molecule tetrafluoro-1,4-benzoquinone (TFBQ), which suits well for the investigation due to its high electron affinity (EA) and its small size. By reaction with hydrogen quinones get reduced, forming diols [23]. The reaction of TFBQ with hydrogen gives the molecule tetrafluoro-1,4-benzenediol (TFBD) acting as chemical defect. In contrast to the quinone case, for diols no charge-transfer reactions with coinage metals are expected. Rather, as any inert material [24–26], they should induce a work-function decrease due to the Pauli-pushback-effect [27].

Here we describe the metal / organic interface via density functional theory (DFT). To analyze the adsorption mechanisms and properties we first investigate the limiting cases of homogeneous monolayers of TFBQ and TFBD adsorbed on the coinage metal surfaces. By a supercell approach we then describe adsorbates containing chemical defects: Mixed monolayers of TFBQ and TFBD. We analyze the Φ dependence on the TFBD fraction, f, and compare the results to the corresponding sub-monolayer cases and to a semi-electrostatic model. Further, we take a look at the electron potential distributions, $U(\vec{r})$, above the coinage metal surfaces with mixed monolayer adsorbates of TFBQ and TFBD and discuss the effects of its corrugation on the transport levels of overlying organic semiconductor layers.

Having investigated the energy level-alignment at the charge injection layer for different conformations of mixed monolayers of TFBQ and TFBD on Cu(111) and Ag(111), a further question arises: Which fraction of chemical defects has to be expected under certain deposition conditions of the charge injection layer undergoing charge transfer reactions? To answer this question we employ *ab initio* thermodynamics and analyze how the TFBD fraction, f, in a mixed monolayer depends on hydrogen pressure of a surrounding gas phase, p_{H_2}, and temperature, T.

2 Fundamentals

Here we describe the theoretical concepts that are used in the course of this thesis. First the focus is laid on DFT: a powerful theory that allows the numerical calculation of ground state energies and electron densities of quantum systems containing hundreds of atoms. Its central premises and ways to handle exchange correlation terms are described. Then the vdW$^{\text{surf}}$-approach is introduced that is used to consider dipole-dipole-interactions arising from correlated fluctuations of the electrons. Further the Mulliken partitioning scheme is explained, which will be used to account for the charges of certain atomic ensembles. Then the focus will shift to general properties of metal / organic semiconductor interfaces: The charge-injection mechanisms that are generally present at such interfaces are described and the importance of the energy level alignment for efficient charge-injection is pointed out. Further, Fermi-level-pinning and the Pauli-pushback effect are introduced. These affect charge-injection barriers via interface dipole formation. Finally the concept of *ab initio* thermodynamics for the description of interfaces is introduced, which allows to build a bridge from the quantum mechanical calculations to macroscopic measurable quantities as temperature and pressure.

2.1 Density Functional Theory

A time-independent quantum mechanical system consisting of M nuclei and N electrons is described by the stationary Schrödinger equation:

$$\hat{H}\Psi(\vec{r}_1,\ldots,\vec{r}_N,\vec{R}_1,\ldots,\vec{R}_M) = E_i\Psi_i(\vec{r}_1,\ldots,\vec{r}_N,\vec{R}_1,\ldots,\vec{R}_M) \tag{2.1}$$

The Hamilton operator, $\hat{H}$, acting on a wave-function, $|\Psi\rangle$, gives a real eigenenergy, E, if Ψ is an eigenfunction of the system. By neglecting the quantized magnetic moments of the elementary particles and fixing the position of the atomic cores (Born-Oppenheimer approximation) the Hamilton operator, $\hat{H}$, in equation 2.1 in atomic units can be written as – compare Jensen [28, equation B.8]:

$$\hat{H} = -\sum_{i=1}^{N}\frac{1}{2}\hat{\nabla}_i^2 - \sum_{A=1}^{M}\sum_{i=1}^{N}\frac{Z_A}{|R_A - \hat{r}_i|} + \sum_{i=1}^{N}\sum_{i=1}^{N}\frac{1}{|\hat{r}_j - \hat{r}_i|} = \hat{T} + \hat{U}_{en} + \hat{U}_{ee} \tag{2.2}$$

Z_A and R_A indicate the atomic number and fixed position of atom A. $r_{i/j}$ is the position of electron i/j.

For a system of interacting electrons the kinetic energy, $\hat{T}$, and the potential energy from the electron-electron interaction, $\hat{U}_{ee}$, increases the complexity of the problem such that so far no exact solution for this many problem was found. To find approximate solutions different approaches were developed: wave-function based methods

– such as the Hartree-Fock method – and density functional methods, on which we focus in this chapter.

2.1.1 Hohenberg-Kohn Theorems

In DFT instead of the $3N$ spatial coordinates of the wave function one uses the electron density, $\rho(\vec{r})$, As a first example of a DFT method one can mention the Thomas-Fermi model [29, 30] that was published in 1928 – two years after the formulation of the Schödinger-equation. There the ground state energy of a single particle in a uniform electron gas is calculated by completely neglecting exchange-correlation and the assumption, that the energy can be expressed in terms of the electron density, $\rho(\vec{r})$. This assumption was confirmed three decades later by two theorems of Hohenberg and Kohn (HK) [31]:

1. > ”For a non-degenerate ground state, the electron potential, $U(\vec{r})$, is (to within a constant) a unique functional of ρ; since, in turn, $U(\vec{r})$ fixes the Hamiltonian $\hat{H}$ also the full many-particle ground state is a unique functional of $\rho(\vec{r})$.” [31]

   Thus, the energy can be written as functional of the charge density ρ:

   $$E_{\mathrm{DFT}}[\rho] = \underbrace{\int \rho(\vec{r})U_{en}(\vec{r})d^3r}_{E_{\mathrm{en}}[\rho]\text{... ext. pot. of the nuclei}} + \underbrace{\frac{1}{2}\iint \frac{\rho(\vec{r})\rho(\vec{r'})}{|\vec{r}-\vec{r'}|}\, d^3r\; d^3r'}_{E_{\mathrm{ee,cl}}[\rho]\text{... classical el.-el. interaction}} + G[\rho] \tag{2.3}$$

   The functional $G[\rho]$ contains the kinetic energy term, $T_{\mathrm{s}}[\rho]$, and a non-classical exchange-correlation term, $E_{\mathrm{ee,xc}}[\rho]$.

2. Due to the variational principle the functional $E_{\mathrm{DFT}}[\rho]$ gives the ground state energy, E_0, of the system only, if the input density, ρ, is the true ground state density, ρ_0 – compare Jenson [28]:

   $$E_0 = E_{\mathrm{DFT}}[\rho_0] = \min_{\rho} E_{\mathrm{DFT}}[\rho] \tag{2.4}$$

   With the boundary condition of particle number conservation:

   $$\int \rho(\vec{r})d^3r = N \tag{2.5}$$

The first HK-theorem can be shown by *reductio ad absurdum*: two different electron potentials cannot result in the same electron density, ρ – see Jenson [28, appendix B.2]. The second HK-theorem stems from the fact, that the energy evaluated by a trial wave function always lies above the true energy, which one would obtain with the true many body wave function – compare Hohenberg and Kohn [31, chapter 2].

This gives an exact result, if an explicit form of $G[\rho]$ exists. However, the functionals $T_\mathrm{s}[\rho]$ and $E_\mathrm{ee,xc}[\rho]$ are unknown.[2] Hence, the discovery of explicit forms for those functionals is the main challenge for developing DFT.

2.1.2 Kohn-Sham Approach[3]

One year after the HK-theorems were published, Kohn and Sham (KS) [33] introduced a mean field approach allowing the iterative calculation of the charge density minimizing the total energy with an additional functional approximating the effects of exchange and correlation. Instead of a interacting system they proposed to investigate the stationary Schrödinger equation of a non-interacting particle in an effective potential caused by the surrounding nuclei and electrons of the system giving the same electron density:

$$\underbrace{\left[-\frac{1}{2}\nabla^2 + v_\mathrm{eff}(\vec{r})\right]}_{\hat{f}_\mathrm{KS}(\vec{r})\text{... Hamiltonian of the KS-approach}} \qquad \psi_i(\vec{r}) = \epsilon_i \psi_i(\vec{r}) \tag{2.6}$$

To find the minimum of the energy functional they applied the Euler-Lagrange formalism:

$$\nabla_\rho E_\mathrm{DFT}[\rho] - \lambda \cdot \left(\int \rho(\vec{r}) d^3r - N \right) = 0 \tag{2.7}$$

The Lagrange-parameter λ accounts for the boundary condition of particle number conservation. With the HK-theorems they derived the following expression for the effective potential, $v_\mathrm{eff}(\vec{r})$:

$$v_\mathrm{eff}(\vec{r}) = U_{en}(\vec{r}) + \frac{1}{2}\int \frac{\rho(\vec{r}')}{|\vec{r}-\vec{r}'|} d^3r' + U_\mathrm{xc}[\rho(\vec{r})] \tag{2.8}$$

The single-electron wave functions ψ_i – the so called Kohn-Sham (KS) orbitals – have no physical meaning.[4] In a DFT-calculation those KS-orbitals are expanded in a set of orthonormal basis functions ϕ_μ:

$$\psi_i = \sum_{\mu}^{M_{basis}} c_{\mu i}\phi_\mu, \qquad \langle \phi_i | \phi_j \rangle = \delta_{i,j} \tag{2.9}$$

By insertion of this expansion into equation 2.6, multiplication with a basis function ϕ_μ and integration over space

$$\sum_{\nu}^{M_{basis}} c_{\nu i} \underbrace{\int \phi_\mu \hat{f}_\mathrm{KS}(\vec{r}) \phi_\nu d\vec{r}}_{\hat{F}^\mathrm{KS}_{\mu\nu}\text{... Kohn-Sham matrix el.}} = \epsilon_i \sum_{\nu}^{M_{basis}} c_{\nu i} \underbrace{\int \phi_\mu \phi_\nu d\vec{r}}_{\hat{S}_{\mu\nu}\text{... overlap matrix el.}} \tag{2.10}$$

---

[2] Except for special cases as the uniform electron gas. [28]

[3] This chapter is mainly based on Koch and Holthausen [32, chapter 7.1].

[4] Except for the HOMO giving the negative ionization potential – compare section 4.2.

one obtains a matrix equation that can be numerically solved for a given KS-Hamiltonian, $\hat{f}_{\mathrm{KS}}(\vec{r})$ – compare Koch and Holthausen [32, equation 7-11]:

$$\hat{F}^{\mathrm{KS}}\hat{C} = \hat{S}\hat{C}\hat{\epsilon} \tag{2.11}$$

With the HK-theorems the KS-approach enables iterative, self-consistent calculation of the expansion coefficients, $\hat{C}$, and, thus, the charge density:

$$\rho(\vec{r}) = \sum_i |\psi_i(\vec{r})|^2 = \sum_i \sum_{\mu\nu}^{M_{basis}} c_{\mu i} c_{\nu i} \phi_\mu \phi_\nu \tag{2.12}$$

A schematic representation of such a self-consistent (SC) cycle is shown in figure 1. From an initial guess of the charge density, ρ, the effective potential $v_{\mathrm{eff}}(\vec{r})$ is calculated. By this then one can obtain the KS-matrix. Solving the set of algebraic KS-equations then gives the expansion coefficients, $\hat{C}$, for the next iteration. This is repeated, until the convergence criteria – regarding energy, charge density or eigenvalues – of the SC-loop are fulfilled.

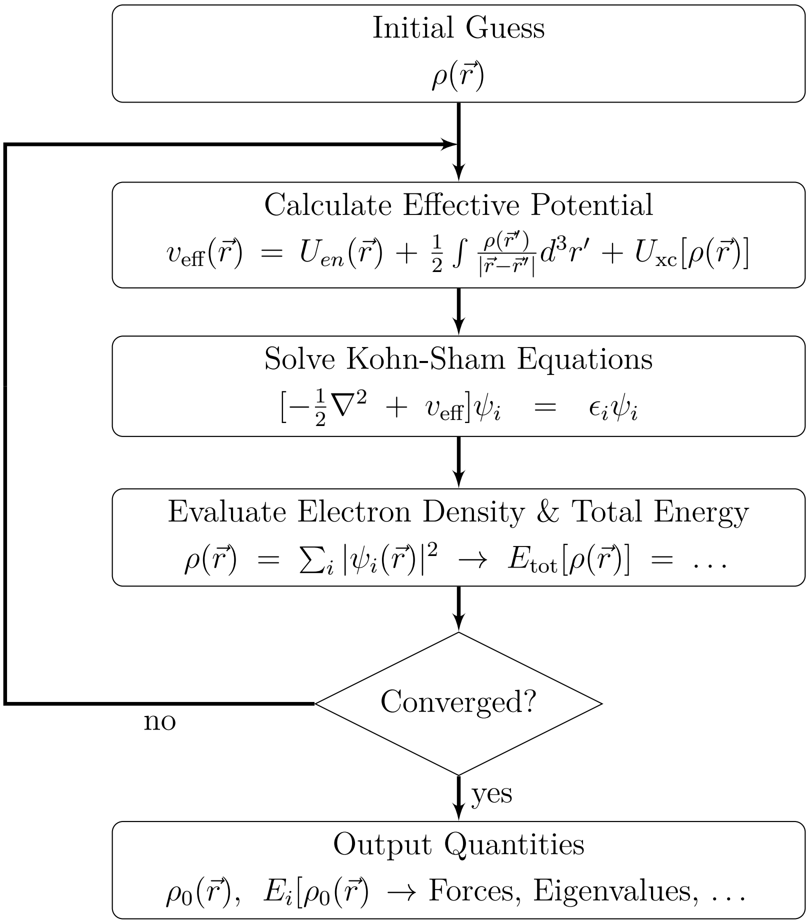

Figure 1: SC-iteration scheme of a DFT calculation. Figure after Gös [34, Figure 3.4]. Permission for use was kindly granted by Wolfgang Gös.

Depending on the particular DFT implementation various types of basis function sets, $\phi_\mu(\vec{r})$, are used: the programs Gaussian [35] or Dalton [36] for instance use Gaussian type basis functions, whereas VASP [37] employs plane-wave basis functions. In FHI-*aims* [38], which is used throughout this thesis, numeric atom-centered basis functions are used.

2.1.3 Exchange-Correlation Functionals[5]

The mapping of interacting particles on a non-interacting system necessitates the introduction of an exchange-correlation functional, $U_{\mathrm{xc}}[\rho]$, for which so far no exact explicit form was found. However, by simulation of exchange-correlation effects via artificial $U_{\mathrm{xc}}[\rho]$-expressions it is possible to calculate ground state energies and charge densities that approximate the exact result very well. Here, we discuss general approaches and a few explicit forms for $U_{\mathrm{xc}}[\rho]$, which enabled DFT to mark as capable tool for the calculation of properties of molecules and solid compounds and the simulation of physical effects on the nanoscopic scale. In the approaches presented in the following, the exchange-correlation energy functional, $E^{\mathrm{LDA}}_{\mathrm{ee,xc}}[\rho]$, is written in terms of separated contributions from exchange and correlation:

$$E_{\mathrm{ee,xc}}[\rho] = \int \rho(\vec{r}) \cdot U_{\mathrm{xc}}[\rho(\vec{r})]\ d^3r = \underbrace{\int \rho(\vec{r}) \cdot U_{\mathrm{x}}[\rho(\vec{r})]\ d^3r}_{E_{\mathrm{x}}[\rho]} + \underbrace{\int \rho(\vec{r}) \cdot U_{\mathrm{c}}[\rho(\vec{r})]\ d^3r}_{E_{\mathrm{c}}[\rho]} \tag{2.13}$$

Local Density Approximation (LDA): This approxmation describes exchange as functional depending on the local charge density $\rho(\vec{r})$:

$$E^{\mathrm{LDA}}_{\mathrm{x}}[\rho] = \int \rho(\vec{r}) \cdot U^{\mathrm{LDA}}_{\mathrm{x}}[\rho(\vec{r})]\ d^3r \tag{2.14}$$

Derived from the situation of an uniform electron gas, $U^{\mathrm{LDA}}_{\mathrm{x}}$ is given by the Dirac formula [28, equation 6.32]:

$$U^{\mathrm{LDA}}_{\mathrm{x}}[\rho] = -\frac{3}{4} \cdot \left(\frac{3}{\pi}\right)^{\frac{1}{3}} \cdot \rho(\vec{r})^{\frac{1}{3}} \tag{2.15}$$

If the densities for different spin polarizations, α and β, are unequal, LDA is replaced by the local spin density approximation (LSDA), where the exchange functional is calculated by the sum of the spin-polarized densities raised to the power of $\frac{4}{3}$. In terms of the spin-polarization function

$$\zeta = \frac{\rho_\alpha - \rho_\beta}{\rho} \tag{2.16}$$

---

[5] This chapter is based on Jensen [28, chapter 6.5].

the LSDA exchange functional can be expressed as – compare Jensen [28, equation 6.34]:

$$U_{\mathrm{x}}^{\mathrm{LSDA}}[\rho] = -\frac{3}{4} \cdot \left(\frac{3}{\pi}\right)^{\frac{1}{3}} \cdot \rho(\vec{r})^{\frac{1}{3}} \cdot \frac{1}{2} \cdot \left[(1+\zeta)^{\frac{4}{3}} + (1-\zeta)^{\frac{4}{3}}\right] \tag{2.17}$$

For the correlation energy functional, $E_{\mathrm{c}}^{\mathrm{LSDA}}[\rho]$, no explicit form is known. However, for intermediate densities correlation energies have been determined by Monte Carlo methods. To use those results interpolation formulas were constructed by Vosko, Wilk and Nusair (VWN) [39] and Perdew and Wang (PW) [40]. With this treatment of the correlation energy LSDA is an exact DFT method for the uniform electron gas [28, pages 246-248].

Generalized Gradient Approximation (GGA): Additional to the local charge density, $\rho(\vec{r})$, here the local gradient of the charge density, $\nabla\rho(\vec{r})$, is considered for the exchange term:

$$E_{\mathrm{x}}^{\mathrm{GGA}}[\rho] = \int \rho(\vec{r}) \cdot U_{\mathrm{x}}[\rho(\vec{r}), \nabla\rho(\vec{r})]\; d^3r \tag{2.18}$$

The first GGA exchange functional was proposed by Becke (B or B88) as correction to the LSDA exchange energy:

$$U_{\mathrm{x}}^{\mathrm{B88}}[\rho, \nabla\rho] = U_{\mathrm{x}}^{\mathrm{LSDA}}[\rho] - \beta \cdot \rho(\vec{r})^{\frac{1}{3}} \cdot \frac{x^2}{1 + 6 \cdot \beta \cdot x \cdot \sinh^{-1} x}, \qquad x = \frac{|\nabla\rho(\vec{r})|}{\rho(\vec{r})^{\frac{4}{3}}} \tag{2.19}$$

It improved the LSDA exchange energy error significantly.

Further improvements are obtained by the exchange-correlation functional proposed by Perdew, Burke and Ernzerhof (PBE) [40], which is also used in the DFT calculations performed in the course of this thesis. Here the LSDA exchange functional is multiplied by an enhancement factor [28, equation 6.41] with the dimensionless parameter x of equation 2.19:

$$U_{\mathrm{x}}^{\mathrm{PBE}}[\rho, \nabla\rho] = U_{\mathrm{x}}^{\mathrm{LSDA}} \cdot \left(1 + a - \frac{a}{1 + b \cdot x^2}\right) \tag{2.20}$$

The PBE correlation functional is a correction term to $U_{\mathrm{c}}^{\mathrm{LSDA}}$:

$$U_{\mathrm{c}}^{\mathrm{PBE}}[\rho, \nabla\rho] = U_{\mathrm{c}}^{\mathrm{LSDA}} + c \cdot f_3^3 \ln\left[1 + d \cdot t^2 \cdot \frac{1 + A \cdot t^2}{1 + A \cdot t^2 + A^2 \cdot t^4}\right] \tag{2.21}$$

with

$$A = d \cdot \left[\exp\left(-\frac{U_{\mathrm{c}}^{\mathrm{LSDA}}}{c \cdot f_3^3}\right) - 1\right]^{-1} \quad ,$$

$$t(\Delta\rho) = [2 \cdot (3 \cdot \pi^3)^{\frac{1}{3}} \cdot f_3]^{-1} \cdot x(\Delta\rho) \quad \text{and}$$

$$f_3 = \frac{1}{2} \cdot [(1+\zeta)^{\frac{2}{3}} + (1-\zeta)^{\frac{2}{3}}] \quad .$$

The parameters a, b, c and d are fitted such that several of the fundamental properties of a exchange-correlation functional – see [28, pages 244-245] – are fulfilled at its best. ζ is the spin-polarization function – see equation 2.16.

Beyond GGA – Hybrid Functionals and More: The main deficiency of (semi-)local functionals as LDA and GGA is the self-interaction error causing non-linearities in the total energy dependence on the electron number, N, and a delocalization of the electron density, ρ – compare Hofmann et al. [41]. In Hartree-Fock theory – compare Jensen [28, chapter 3 and chapter 6.5.4] – this error does not occur, because there the exchange-term

$$E_{\mathrm{x}}^{\mathrm{HF}} = -\frac{1}{2} \sum_{i,j} \int \frac{\psi_i^*(\vec{r})\psi_j(\vec{r})\psi_j^*(\vec{r}')\psi_i(\vec{r}')}{|\vec{r} - \vec{r}'|} \, d^3r \, d^3r' \tag{2.22}$$

cancels with the Coulomb-term for $i = j$. One possibility to mitigate the self-interaction error of DFT is the use of hybrid functionals: There $E_{\mathrm{x}}^{\mathrm{HF}}$ is introduced via a mixing parameter, α:

$$E_{\mathrm{x}}^{\mathrm{hyb}} = \alpha \cdot E_{\mathrm{x}}^{\mathrm{HF}} + (1 - \alpha) \cdot E_{\mathrm{x}}^{\mathrm{DFT}} \tag{2.23}$$

A common choice for the mixing parameter in hybrid functionals such as PBE0 [42] or HSE06 [43] is $\alpha = \frac{1}{4}$.[6] However, the evaluation of $E_{\mathrm{x}}^{\mathrm{HF}}$ is computationally expensive, which is especially crucial for large many-body-systems. Moreover via the additional mixing parameter the *ab initio* character of the simulations may get questionable.

Another approach beyond GGA is the generalized random phase approximation (GRPA) witch also treats vdW-interactions – compare Perdew et al. [44] – and "systematically improves the results towards the exact limit, but inherits also the wave function disadvantages of a slow convergence with respect to basis set size." [28, page 254].

2.1.4 Van Der Waals Interactions[7]

Generally vdW-forces arise out of interactions of electrical dipoles. One distinguishes between three different kinds of vdW-interactions:

- Keesom interactions describe interactions of permanent dipoles.
- Debye interactions describe the interaction of a permanent dipole with a non-polar particle. The permanent dipole induces a dipole moment of opposite direction in the latter.

---

[6] Further usually an additional parameter, ω, is introduced that confines the spatial range for the usage of the hybrid functional.

[7] This introduction to vdW-interactions is based on the general overview in Parsegian [45].

- London interactions describe the interaction of non-polar but polarizeable particles. They are much weaker than covalent or ionic bonds, but often are responsible for the formation of noble-gas crystals or the physisorption of molecules on surfaces. Usually the term vdW-interactions refers just to this kind of interactions.

To perform DFT calculations approximations to the exchange-correlation term are necessary. By application of those – for example LDA or GGA – weak long range interactions and, thus, London interaction (often just referred to as vdW-interactions) are neglected. One possibility to account for those is to reinvent them by an adding a vdW-term E_{vdW} to the energy of the system:

$$E_{\mathrm{sys}} = E_{\mathrm{DFT}} + E_{\mathrm{vdW}}, \tag{2.24}$$

with the energy from the DFT calculation with exchange-correlation functional denoted as E_{DFT}. For the description of molecules adsorbed on metal surfaces by comparison to experimental results it turned out that the approach of Tkatchenko and Scheffler [46] (TS) for the vdW-term is very useful:

$$E_{\mathrm{vdW}} = -\frac{1}{2}\sum_{\mathrm{A,B}} f_{\mathrm{damp}}(R_{\mathrm{A,B}}, R^0_{\mathrm{A}}, R^0_{\mathrm{B}}) \cdot C_{6\mathrm{A,B}}[\rho] \cdot R^{-6}_{\mathrm{A,B}}, \tag{2.25}$$

with the distances, $R_{\mathrm{A,B}}$, between two atoms A and B, $C_{6\mathrm{A,B}}$-coefficients to consider the effect of the environment and a damping function f_{damp}, which is introduced to avoid singularities at small distances and which is dependent on the vdW-radii R^0_{A} and R^0_{B} of the involved atoms.

To include screening effects Ruiz et al. [47] combined the aforementioned TS-approach with Lifshitz-Zaremba-Kohn (LZK) theory. They recovered the LZK-formula for the C_3-coefficient by summation over the pair potentials, what allowed the recalculation of $C^{\mathrm{LZK}}_{6\mathrm{a,b}}$ coefficients based on the polarizability of an adsorbed atom and the dielectric function of the solid. Further they disentangled the heteronuclear $C^{\mathrm{LZK}}_{6\mathrm{a,b}}$ into homonuclear coefficients $C_{6\mathrm{a,a}}$ and $C^{\mathrm{LZK}}_{6\mathrm{b,b}}$:

$$C^{\mathrm{LZK}}_{6\mathrm{a,b}} = \frac{2 \cdot C_{6\mathrm{a,a}} \cdot C^{\mathrm{LZK}}_{6\mathrm{b,b}}}{\frac{\alpha^{\mathrm{LZK}}_{\mathrm{b}}}{\alpha^0_{\mathrm{a}}} \cdot C_{6\mathrm{a,a}} + \frac{\alpha^0_{\mathrm{a}}}{\alpha^{\mathrm{LZK}}_{\mathrm{b}}} \cdot C^{\mathrm{LZK}}_{6\mathrm{b,b}}}, \tag{2.26}$$

with the effective polarizabilities α^0_{a} and $\alpha^{\mathrm{LZK}}_{\mathrm{b}}$ of an adsorbate atom and an atom in the solid. Further the vdW-radii, $R^{\mathrm{LZK}}_{\mathrm{b}}$, of the bulk-atoms were adapted to restrict the summation regarding equation 2.25 via the damping function f_{damp}. The values of $C^{\mathrm{LZK}}_{6\mathrm{b,b}}$, $\alpha^{\mathrm{LZK}}_{\mathrm{b}}$ and $R^{\mathrm{LZK}}_{\mathrm{b}}$ that they obtained for coinage metals are quoted in table 1.[8]

---

[8] Those values were also used for the vdW$^{\mathrm{surf}}$ calculations performed within this thesis.

Table 1: Screened $C_{\mathrm{6b,b}}^{\mathrm{LZK}}$ coefficients (Hartree · Bohr^6), polarizability $\alpha_{\mathrm{b}}^{\mathrm{LZK}}$ (in Bohr^3) and vdW radii $R_{\mathrm{b}}^{\mathrm{LZK}}$ (in Bohr) for coinage metal substrates. Values taken from Ruiz et al. [47, Table I]

Substrate	$C_{\mathrm{6b,b}}^{\mathrm{LZK}}$	$\alpha_{\mathrm{b}}^{\mathrm{LZK}}$	$R_{\mathrm{b}}^{\mathrm{LZK}}$
Cu	59	10.9	2.40
Ag	122	15.4	2.57
Au	134	15.6	2.91

2.1.5 Population Analysis by the Mulliken Scheme[9]

Besides the energy from the electronic wave function many other properties can be determined. By partitioning the wave functions in therms of the basis functions fractional charges can be attributed to the atoms of the studied system.
The electron density ρ_i (probability of finding an electron) at a certain position $\vec{r}$ from a single molecular orbital containing one electron is given as the square of the molecular orbital wave-function, ψ_i:

$$\rho_i(\vec{r}) = \psi_i(\vec{r})^2 \tag{2.27}$$

If the molecular orbital is expanded in a set of normalized, but non-orthogonal, basis functions χ:

$$\psi_i(\vec{r}) = \sum_{\mu}^{M_{basis}} c_{\mu i}\phi_\mu \tag{2.28}$$

equation 2.27 can be rewritten as:

$$\rho_i(\vec{r}) = \sum_{\mu\nu}^{M_{basis}} c_{\mu i}c_{\nu i}\phi_\mu\phi_\nu \tag{2.29}$$

Integrating over space and summing up over all occupied molecular orbitals gives the total number of electrons, N_{elec}:

$$\sum_{i}^{N_{occ}} \int \rho_i(\vec{r})\mathrm{d}r = \sum_{i}^{N_{occ}} \sum_{\mu\nu}^{M_{basis}} c_{\mu i}c_{\nu i} \cdot \underbrace{\int \phi_\mu\phi_\nu \mathrm{d}r}_{=S_{\mu\nu}\dots\text{ overlap integral}} = \sum_{i}^{N_{occ}} \sum_{\mu\nu}^{M_{basis}} c_{\mu i}c_{\nu i}S_{\mu\nu} = N_{elec} \tag{2.30}$$

This expression can be generalized by introducing an occupation number, n_i, for

---

[9] The following description of the population analysis scheme of Mulliken [48] follows the book of Jensen [28, chapter 9.1].

each molecular orbital:

$$\sum_{i}^{N_{orb}} n_i \int \rho_i(\vec{r})\mathrm{d}r = \sum_{\mu\nu}^{M_{basis}} \underbrace{\left(\sum_{i}^{N_{occ}} n_i c_{\mu i} c_{\nu i}\right)}_{=D_{\mu\nu}\text{... density matrix element}} S_{\mu\nu} = \sum_{\mu\nu}^{M_{basis}} D_{\mu\nu} S_{\mu\nu} = N_{elec} \tag{2.31}$$

For a single-determinant wave function, n_i will be either 0, 1 or 2, while it may be a fractional number for a correlated wave function.

In the scheme proposed by Mulliken the products of the density and overlap matrix elements $D_{\mu\nu}S_{\mu\nu}$ are distributed into atomic contributions. The diagonal elements of this element-wise product matrix $D_{\mu\mu}S_{\mu\mu}$ give the number of electrons in the atomic orbital μ . The off-diagonal elements $D_{\mu\nu}S_{\mu\nu}$ give the number of electrons shared by the atomic orbitals μ and ν. To find the number of electrons associated with a certain atom A, the contributions from all atomic orbitals located at the atom are summed up:

$$\rho_A = \sum_{\mu \in \mathrm{A}}^{M_{basis}} \sum_{\nu}^{M_{basis}} D_{\mu\nu} S_{\mu\nu} = N_{elec} \tag{2.32}$$

Finally the gross charge on atom A is calculated by subtracting the nuclear charge, Z_A:

$$Q_A = Z_A - \rho_A \tag{2.33}$$

Certain problems arise with such a population analysis, where the wave function is partitioned in terms of basis functions – compare Jensen [28, page 295]: Diagonal elements may get larger than two, violating the Pauli principle, and off-diagonal elements may get negative, which is physically impossible. Further the results strongly depend on the chosen basis functions.

Alternative partitioning schemes are based on the electrostatic potential (ESP) – see Jensen [28, chapter 9.2] –, the charge density (Q) – see Jensen [28, chapter 9.3] – or natural bond orbitals (NBO) – see Jensen [28, chapter 9.6].

2.2 Metal / Organic Semiconductor Interfaces

In organic electronic devices metal / organic semiconductor interfaces are omnipresent. They strongly affect charge-injection and, thus, the performance of the devices – see Koch [4]. A comprehensive understanding of the underlying mechanisms for the energy level alignment at the interface, therefore is a necessity to enable further improvements in organic electronics.

For an applied voltage the central charge-injection mechanism at a metal / organic semiconductor interface is thermionic emission – for high voltages also tunnelling can occur. The current density depends exponentially on charge-injection barriers that are determined by the alignments of the energy levels at the interface – compare Peng [3]. Corresponding to the Schottky effect a modification of charge-injection barrier occurs depending on the applied voltage – compare [49, Page 147]. Depending on the metal electrode and the species of the organic semiconductor, charge-injection can be enhanced by the use of a deliberately chosen charge-injection layer lying in between the metal and the organic semiconductor. This additional layer allows a modification of the energy level alignment at the interface adjusting charge-injection barriers.

2.2.1 Energy Level Alignment and Charge-Injection Barriers

The band diagram of a metal / organic semiconductor interface is sketched in figure 2. For the following discussion we denote z the direction perpendicular to the interface plane spanned by the directions x and y. Due to interface dipole formation and band bending the VL below and above the system differ – compare Ishii et al. [50, chapter 2.3.1].[10] The transport levels of the organic semiconductor are determined by the corresponding EA and IP of the organic species and can be approximated by the LUMO and HOMO.

The hole injection barrier , Φ_B^h, can be approximated by the energy difference of the Fermi energy, E_F, to the HOMO, while the electron injection barrier, $\Phi_B^{e^-}$, is determined by the energy gap between E_F and the LUMO. The approximative character of this definition stems from the fact that molecular orbitals are an approximation and from the broadening of the states upon adsorption. The charge-injection layer (CIL) deposited upon the metal surface modifies the work function by $\Delta\Phi$ via interface dipole formation. This modification affects the value of E_F relative to VL' above the surface.[11]

---

[10] For infinite distance the VL above and below the system converge to a common VL(∞)

[11] VL' corresponds to the situation where just the charge-injection layer (CIL) leading to $\Delta\Phi$ is deposited on the metal surface.

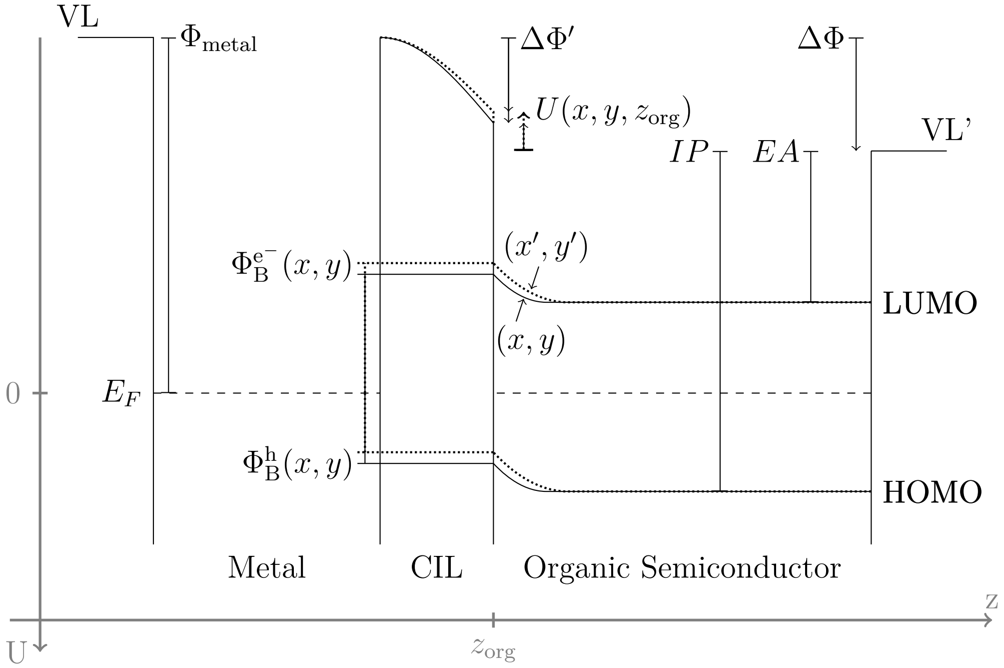

Figure 2: Band diagram at a metal / organic semiconductor interface. The interface dipole formed upon adsorption of the charge-injection layer (CIL) shifts the vacuum level such that a decrease of the work function by $\Delta\Phi$ occurs. The energy levels are bent by the charge redistribution in the first organic layers to achieve electrical equilibrium – compare Ishii et al. [50, Caption of Figure 6]. For details see text. The image is adapted from Ishii et al. [50, Figure 6b].

With the aforementioned definition, electron and hole injection barriers can be written as – compare Ishii et al. [50, Equations 3 and 4]:

$$\Phi_{\text{B}}^{\text{h}} = |IP - (\Phi_{\text{metal}} + \Delta\Phi')| \tag{2.34}$$

$$\Phi_{\text{B}}^{\text{e}^-} = |EA - (\Phi_{\text{metal}} + \Delta\Phi')| \tag{2.35}$$

However, for an organic monolayer the electron potential distribution, $U(\vec{r})$, which determines the positions of the HOMO and LUMO relative to E_F, is not homogeneous at the position, z_{org}, of the first layer of the organic semiconductor above the CIL. For different positions (x, y) and (x', y') in the interface plane above the CIL the electron potential $U(\vec{r})$ can vary.[12] Due to the corrugation of the electron potential above the CIL, $U(x, y, z_{\text{org}})$, the band bending[13] in the organic semiconductor and, hence, charge-injection barriers become a function of position in the (x-y) plane of

---

[12] The courses of $U(z)$ at different locations in the interface plane (x, y) and (x', y') are indicated by the solid and dotted lines for in figure 2.

[13] The charge-rearrangements induced by adsorption of the CIL cause an electric field that shifts the energy levels in the overlying organic layers.

the interface.[14] Including this to the definition of charge-injection barriers equations 2.34 and 2.35 may be rewritten as:

$$\Phi_{\mathrm{B}}^{\mathrm{h}}(x,y) = |IP - (\Phi_{\mathrm{metal}} + \Delta\Phi) - U(x,y,z_{\mathrm{org}})| \tag{2.36}$$

$$\Phi_{\mathrm{B}}^{\mathrm{e}^-}(x,y) = |EA - (\Phi_{\mathrm{metal}} + \Delta\Phi) - U(x,y,z_{\mathrm{org}})| \tag{2.37}$$

Besides $\Delta\Phi$ with this definition besides x and y z_{org} gets important for the magnitude of $U(x,y,z_{\mathrm{org}})$. It can be expected that for most cases the magnitude of $U(x,y,z_{\mathrm{org}})$ is much smaller than for $\Delta\Phi$. At an applied voltage, however, due to the (x,y)-dependence of charge-injection barriers it can come to regions of increased current density from thermionic emission.

2.2.2 Work Function Modification via Interface Dipoles

The energy level alignment at the interface is strongly determined by the chemical properties of organic molecules forming the first layer adsorbed upon the metal electrode. The adsorbate causes the aforementioned work function modification, $\Delta\Phi$, via interface dipole formation affecting charge-injection barriers. An overview of possible factors leading to $\Delta\Phi$ is shown in figure 3.

$\Delta\Phi$ is caused by interface dipole formation that is composed out molecular dipoles, which are determined by the distribution of the partial charges of a polar molecule, and bond dipoles, which are caused by charge rearrangements upon adsorption. With the corresponding potential shifts ΔE_{mol} and ΔE_{bond} the work function modification is written as:

$$\Delta\Phi = \Delta E_{\mathrm{mol}} + \Delta E_{\mathrm{bond}} \tag{2.38}$$

The distortion and alignment of a polar molecule upon adsorption, determines the distribution of the partial charges. This can lead to a dipole field perpendicular to the surface shifting the vacuum level. For polar molecules, molecular dipoles can give significant contributions to $\Delta\Phi$.

Charge rearrangements upon adsorption and hence bond dipoles are caused by a couple of effects. With the simple electrostatic model of an infinitely extended plate capacitor the bond dipole, ΔE_{bond}, can be approximately calculated via the solution of the one-dimensional Poisson equation – compare Koch [4] and Romaner et al. [52]:

$$\Delta E_{\mathrm{bond}} = -\frac{\mathrm{e}}{\epsilon_0} \cdot \frac{\mu}{A} \tag{2.39}$$

$\mu = d \cdot Q$	molecular dipole that can be approximated as a point dipole with the adsorption distance, d, and the charge transfer, Q.
A	area of the two-dimensional unit cell of the adsorbed molecules.

---

[14] The corrugation and convergence of $U(\vec{r})$ strongly depends on the spacing of the adsorbed molecules in the CIL as shown by Natan et al. [51].

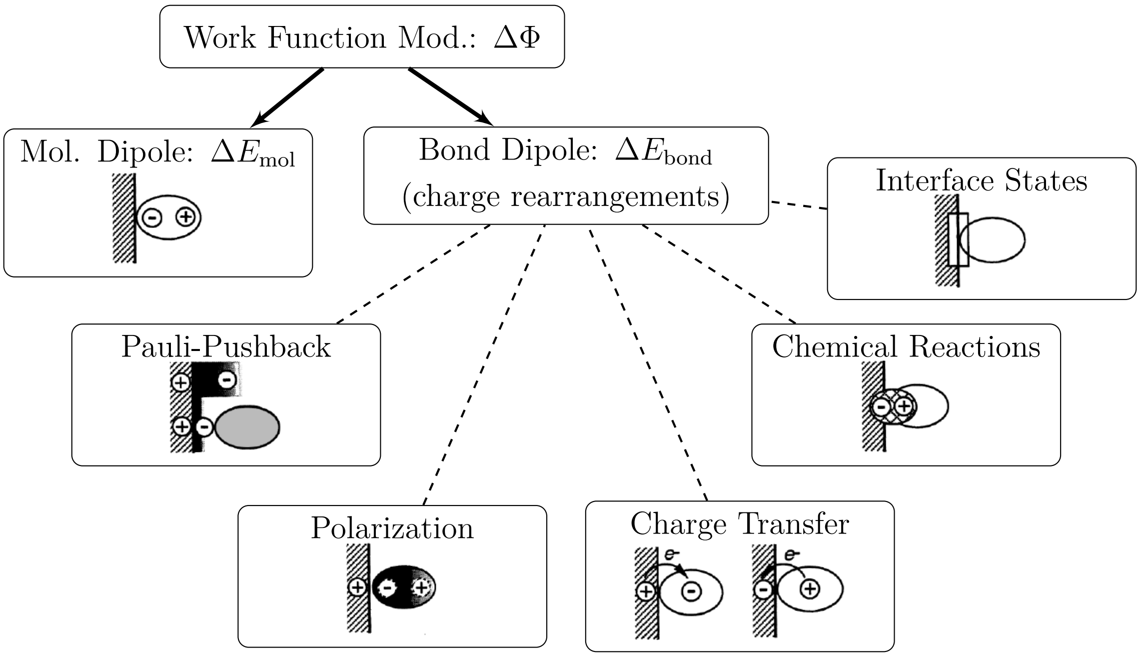

Figure 3: Scheme of the main contributions (arrows) to the work function modification, $\Delta\Phi$. Possible mechanisms leading to charge rearrangements are indicated via dashed lines. The sketches inside the nodes are taken from Ishii et al. [50, Figure 16]. Permission for use was kindly granted by Hisao Ishii.

At any interface the Pauli-pushback effect is present: This effect includes no charge transfer with the molecule. Here the charge rearrangements are caused by the modification of the electron density by the metal spilling out into vacuum. An overlap of the wave-functions of the metal and the molecule would violate the Pauli exclusion principle. Upon adsorption due to attractive forces – such as vdW-interaction, covalent bonds or ionic bonds – and Pauli repulsion electron-density above the metal-surface is pushed back by the adsorbed molecule. The reduced electron-spill-out results in a net positive charge at the adsorption site forming a dipole with the repelled charge giving a negative contribution to $\Delta\Phi$. Examples of systems, where ΔE_{bond} is dominated by Pauli pushback are benzene or cyclohexane on Cu(111) or Ag(111) – compare Witte et al. [53].
Another possible effect leading to bond dipole formation decreasing $\Delta\Phi$ roots in a polarization of the molecule to stabilize the electron density above the molecule.
For strong electron-acceptors or -donors charge transfer to or from the adsorbate has to be expected leading to an in- or decrease of $\Delta\Phi$. Depending on the underlying situation different concepts are suitable for the description of charge transfer at the interface. For passivated surfaces for instance the integer charge transfer model is used – see Braun et al. [54]. For adsorption of small, π-conjugated organic

molecules on non-passivated metal surfaces, on the other hand fractional charge transfer takes place stemming from rearrangements of the electron-density upon adsorption. Charge transfer between the organic adsorbate and the metal is often encountered if chemical reactions occur.

Through interaction with the wave-function of the metal the molecular states can hybridize and broaden so strong that they reach beyond E_F and, thus, get partially depopulated or occupied, depending on whether one is dealing with a HOMO or a LUMO state.

For strong electron-acceptors also Fermi-level-pinning can occur. Considering the separated systems of the adsorbate and the metal electrode, one finds that due to the high EA of the adsorbed molecules the energy of the LUMO is lower than E_F. Upon adsorption, hence, the LUMO gets filled forming a dipole. This dipole field shifts the LUMO up in energy until it approaches E_F, where it gets depopulated until equilibrium conditions are reached. As a consequence, the LUMO gets pinned at E_F.

Fermi-level-pinning can also occur for molecules of high ionization potential: In the Schottky-Mott limit there the HOMO lies above E_F. Upon adsorption it gets depopulated forming a dipole that shifts it down in energy.

However, the aforementioned factors do not occur separately. Charge transfer for instance can occur in both directions simultaneously: One example is the strong electron-acceptor tetrafluoro-tetracyanoquinodimethane (F4TCNQ), which chemically bonds to Cu(111). There the charge transfer to the molecule from the Fermi-level-pinned LUMO is mitigated by strong hybridization of deeper lying occupied states triggering back-transfer of the charges – compare Romaner et al. [16]. Additionally, the mechanisms leading to interface dipole formation can also affect each other. In Fermi-level-pinned systems for instance only the molecular dipole above the pinning-induced charge-transfer region contributes to $\Delta\Phi$, whereas its contributions below that region get compensated by the bond-dipole – compare Hofmann et al. [55].

2.3 Ab Initio Thermodynamics for Surfaces[15]

Here a theory is presented, which builds a bridge from the microscopic (electronic) states to macroscopically measurable quantities by the combination of results from DFT calculations and thermodynamic principles. It allows to determine the most stable geometry and composition at an interface of a solid and a gas. To keep the discussion simple, here a solid crystal[16] is considered that is in contact with a homogeneous gas phase[17] of diatomic gas molecules (as hydrogen). A schematic representation of the interface is shown in figure 4.

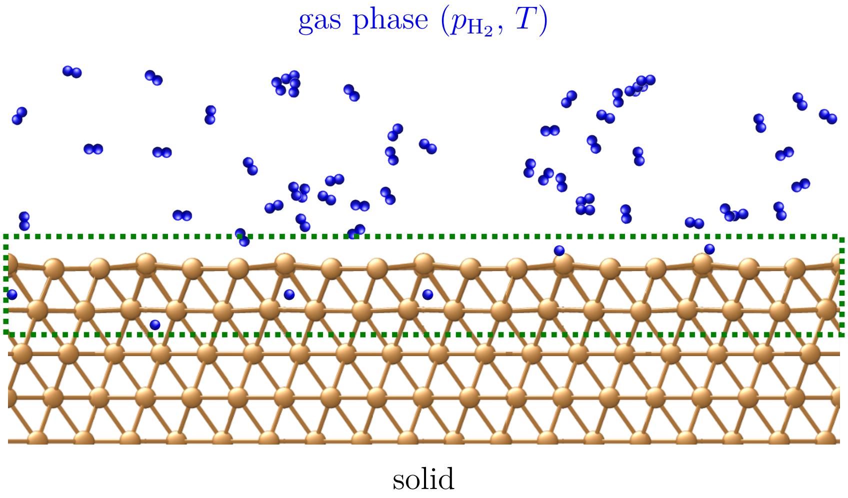

Figure 4: Sketch of an interface of a solid and gaseous phase. The area bordered by the dotted, green rectangle represents the finite part of the system that is affected by the presence of the surface. Sketch after Rogal et al. [56, Figure 1].

For an isothermal-isobaric ensemble the most stable configuration minimizes the Gibbs free energy, G. For the studied system G can be separated into contributions from the (bulk) solid phase, G_{solid}, and the homogeneous gaseous phase, G_{gas}. Further contributions of the surface, G_{surf}, have to be considered, where, due to the interaction with the gas phase, deviations from the bulk solid have to be expected. Thus, G can be written as:

$$G = G_{\text{solid}} + G_{\text{surf}} + G_{\text{gas}} \tag{2.40}$$

For a homogeneous surface G_{surf} scales linearly with the area, A, of a periodic two-dimensional unit cell. This allows the introduction of the surface free energy per

---

[15] This introduction to *ab initio* thermodynamics mainly follows the paper of Rogal et al. [56].

[16] In chapter 6.9 we will apply this theory to a more complex system of a mixed monolayers of TFBQ and TFBD adsorbed upon Cu(111) and Ag(111).

[17] An interesting publication of ab initio thermodynamics with multiple surrounding gas phases was published by Herrmann et al. [57].

area:

$$\gamma = \frac{1}{A}\left(G - G_{\text{solid}} - G_{\text{gas}}\right) \tag{2.41}$$

With γ only the Gibbs free energy of the interface region is described – see area bordered by the dotted, green rectangle in figure 4. Contributions of the solid and gaseous phase (contained in G_{solid} and G_{gas}) that are not affected by the interface also appear in G and, thus, cancel each other out. Hence just those atoms have to be accounted, which are located in the interface region.

If this region contains N_{solid} repeating units forming the solid phase and N_{gas} dissociated gas molecules per surface area incorporated to the interface, equation 2.41 can be rewritten as:

$$\gamma = \frac{1}{A}\left(G - N_{\text{solid}} \cdot g_{\text{solid}} - N_{\text{gas}} \cdot \mu_{\text{gas}}\right) \tag{2.42}$$

with the Gibbs free energy per repeat unit in the bulk of the solid, g_{solid}, and the chemical potential of the gas phase, μ_{gas}.

Besides the total energies of the corresponding systems G, g_{solid} and μ_{gas} contain terms from vibrational free energy and configurational entropy. Writing those contributions in separated terms equation 2.42 can be rewritten as:

$$\gamma = \frac{1}{A}\left(E - N_{\text{solid}} \cdot \epsilon_{\text{solid}} - N_{\text{gas}} \cdot \mu_{\text{gas}} - T \cdot S_{\text{conf}} + F_{\text{vib}}\right) \tag{2.43}$$

Thereby the total energies appear that are calculable via DFT – see symbols E, ϵ_{solid} and ϵ_{gas}. Depending on the investigated systems F_{vib} and S_{conf} can be neglected or have to be taken into account – compare Reuter [58], Kresse [59] or Herrmann [57].

The chemical potential of the gas phase can be separated in two terms: The ground state energy of a gas molecule, ϵ_{gas}, and contributions that depend on gas pressure and temperature, $\Delta\mu_{\text{gas}}(p, T)$:

$$\mu_{\text{gas}}(p, T) = \epsilon_{gas} + \Delta\mu_{\text{gas}}(p, T) \tag{2.44}$$

For the calculation of $\Delta\mu_{\text{gas}}(p, T)$ different approaches exist. In the following section we discuss the chemical potential for a real gas based on tabulated data and the chemical potential for an ideal gas based on a theoretically derived expression and perform a comparison of the two approaches for the case of a hydrogen gas phase.

2.3.1 Chemical Potential of a Real Gas

For a real gas customarily the chemical potential is calculated based on tabulated data. As standard database often NIST-JANAF [60] is used – compare Reuter et al. [61] or Bollinger et al. [62]. $\Delta\mu_{\text{gas}}(p,T)$ then is expressed relative to a standard pressure, p_0:

$$\Delta\mu_{\text{gas}}(p,T) = \Delta h_{\text{gas}}(p_0,T) - T \cdot s_{\text{gas}}(p_0,T) + k_B T \ln\left(\frac{p}{p_0}\right) \tag{2.45}$$

$\Delta h_{\text{gas}}(p_0,T)$	enthalpy contributions at standard pressure, p_0
$s_{\text{gas}}(p_0,T)$	entropy contributions at standard pressure, p_0

Because the calculated chemical potential here depends on data from experiments, with this approach better agreement with experimental results can be expected. Using tabulated data, however, the *ab initio* character of the calculations may get questionable.

2.3.2 Chemical Potential of an Ideal Gas

If ideal gas behaviour can be expected, also theoretically derived expressions can be used – compare Herrmann [57]. With an ideal gas, just translational degrees of freedom must be accounted. Then the chemical potential is related to gas pressure p and temperature T via the equation – compare Loffreda et al. [63]:

$$\Delta\mu_{\text{gas}}(p,T) = k_B\, T\, \ln\left(\frac{p\lambda_{\text{gas}}(T)^3}{k_B\, T}\right) \tag{2.46}$$

with the thermal De'Broglie wavelength, λ_{gas}, of the gas molecules, which, according to statistical physics – compare Nolting et al. [64] –, is given by

$$\lambda_{gas}(T) = \frac{h}{\sqrt{2\pi m_{\text{gas}} k_B T}}, \tag{2.47}$$

with the mass of the gas molecules, m_{gas}.
For comparison with the chemical potential of a real gas we rewrite equation 2.46 for the chemical potential of an ideal gas to:

$$\Delta\mu_{\text{gas}}(p,T) = k_B\, T\, \ln\left(\frac{p_0\lambda_{\text{gas}}(T)^3}{k_B\, T}\right) + k_B T \ln\left(\frac{p}{p_0}\right) \tag{2.48}$$

2.3.3 Comparison of the Approaches for the Case of Hydrogen

Comparing the expressions for the chemical potential of a real and an ideal gas – see equations 2.45 and 2.48 –, we find that the two approaches only differ in they temperature dependencies, which can be written as:

$$\Delta\mu_{\mathrm{real,H_2}}(p_0, T) = \Delta h_{\mathrm{H_2}}(p_0, T) - T \cdot s_{\mathrm{H_2}}(p_0, T) \tag{2.49}$$

$$\Delta\mu_{\mathrm{ideal,H_2}}(p_0, T) = k_B\,T\,\ln\left(\frac{p_0 \lambda_{\mathrm{H_2}}(T)^3}{k_B\,T}\right) \tag{2.50}$$

If figure 5 for the case of a hydrogen gas the temperature dependencies are plotted via the two approaches. Reference pressure was set to $p_0 = 10^5$ Pa. The deviations of $\Delta\mu_{\mathrm{gas}}(p_0, T)$ increase with temperature: At 300 K the deviation amounts to 1 meV, whereas at 1000 K already a deviation of 82 meV is observed.

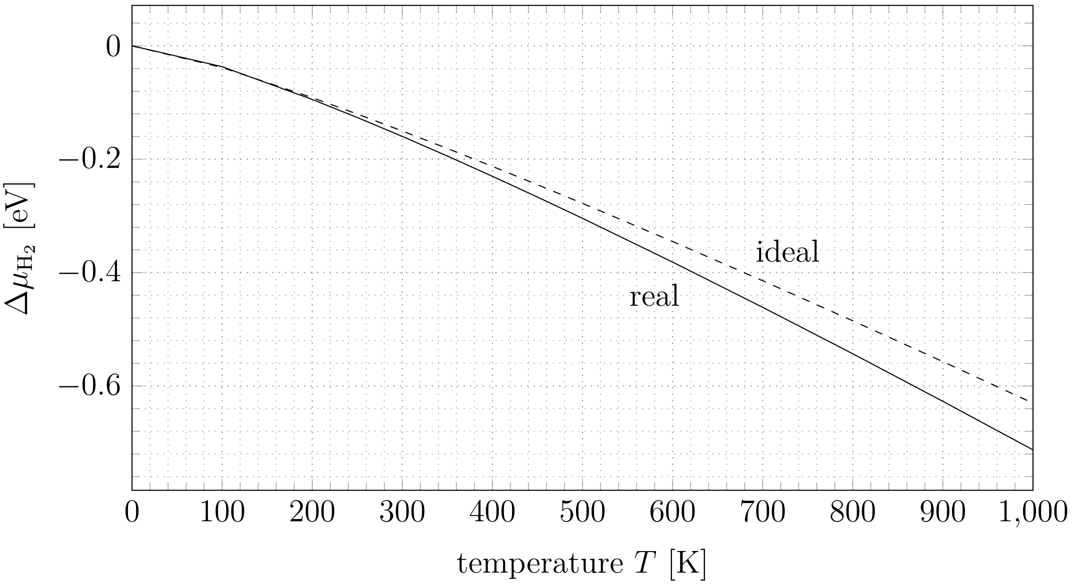

Figure 5: Comparisons of the contributions to the chemical potential, $\Delta\mu_{\mathrm{gas}}(p_0, T)$, for a real gas (solid line) based on tabulated data and for an ideal gas (dashed line) based on a theoretically derived expression.

3 Computational Details[18]

In this section we first will give an overview of the computational settings that served as basis for the DFT-calculations performed within this thesis. In the subsequent sections then certain convergence tests are shown that led to the chosen settings – the results of those tests are summarized in table 2.
The DFT-calculations were performed using the FHI-*aims* code [38] with the Perdew-Burke-Ernzerhof (PBE) exchange-correlation functional [40], augmented by the-vdW$^{\text{surf}}$ method to account for the missing long range van-der-Waals interactions [46,47]. vdW-interaction between metal atoms were suppressed. The discrete eigenvalues of the Kohn-Sham-orbitals were broadened by a Gaussian function with a ”variance”, $\sigma = \frac{0.1}{\sqrt{2}}$ eV. The lattice constants, a, for Cu ($a_{\text{Cu}} = 3.632$ Å) and Ag ($a_{\text{Ag}} = 4.151$ Å) were determined by maximizing the cohesive energy of the bulk crystal from a series of DFT calculations with variations in a. The interface was modelled via the repeated slab approach with a four layer slab of Cu(111) or Ag(111) separated by at least 30 Å of vacuum and a self-consistent dipole correction to account for the asymmetry of the slab [65]. The repeated slab calculations with a single molecule in the the two dimensional unit cell were performed with a 12×12×1 Monkhorst-Pack k-point grid [66]. For larger cells the k-point grid was scaled appropriately. The “tight” defaults, as shipped with FHI-*aims*, were used throughout the whole calculations, except for the onset and width parameters of the confining potential for the basis functions, which were manually set to 4.6 Å and 2.6 Å, respectively, to increase the accuracy of the results. The convergence limits of the charge density, the eigenvalues and the total energy in the SCF-cycles were set to $10^{-4}\ \frac{\text{e}}{\text{Å}^3}$, 10^{-3} eV and 10^{-5} eV, respectively.

Table 2: Basic computational settings obtained from convergence tests.

Parameter	Value	Quantity	Residuum [meV]		
			Cu	Ag	Au
set of basis functions	tier1	E_c	15	11	6
cutting parameters	4.6 2.6 1	Φ	6	8	10
number of layers	4	Φ	11	82	40
number of k-points[19]	32	Φ	2	1	5

---

[18] This section contains contents of Edlbauer et al. [1, Section 2, Computational Details].

[19] This are the values along the x and y direction of a $1 \times 1\sqrt{3}$ unit cell with six layers.

3.1 Lattice Constant Optimization

If one would choose experimental values for the lattice constant in DFT calculations, in geometry optimization processes of a repeated-slab geometry it would come to spurious relaxations of the surface. To avoid this, the lattice constant has to be chosen such that the cohesive energy calculated within DFT, E_{c}, is maximized. For a primitive unit cell generally this quantity is calculated by the formula:

$$E_{\mathrm{c}} = -\left(\frac{E_{\mathrm{prim.}}}{N_{\mathrm{prim.}}} - E_{\mathrm{isol.}}\right) \tag{3.1}$$

$E_{\mathrm{prim.}}$ ... total energy of the atoms in a crystal's primitive unit cell
$N_{\mathrm{prim.}}$ ... number of atoms in a primitive unit cell of an ideal crystal lattice
$E_{\mathrm{isol.}}$ .... total energy of an isolated atom.

Sets of DFT-calculations were performed where the lattice constants of the coinage metals were varied around reference values from Straumanis et al. [67]. With the resulting ground state energies the cohesive energy was calculated using equation 3.1 – the results are shown in figure 6. Besides the settings mentioned before, for the corresponding DFT calculations a 20 × 20 × 20 k-grid was employed. Due to

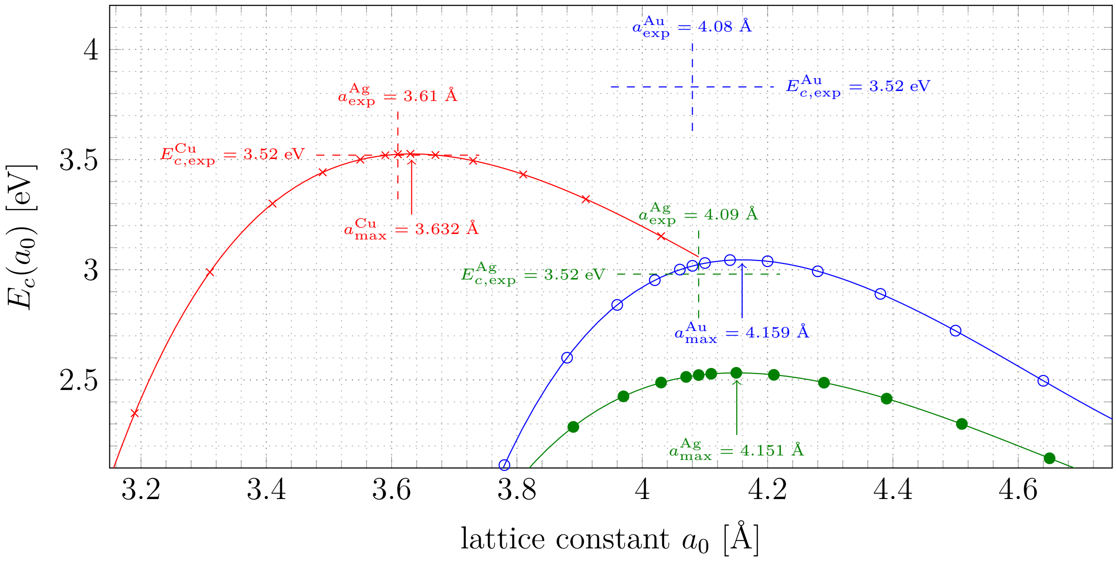

Figure 6: Cohesive energies E_c of Cu (red crosses), Ag (green dots) and Au (blue circles) atoms in the bulk as function of the lattice constant a_0. The optimum values regarding cohesive energy (up pointing arrows) were obtained by the local maximums of polynomials of fifth order (lines) fitted to the data points. Reference values from experiments are indicated as dashed cross lines – see Straumanis et al. [67] and Schimka et al. [68]

the simple basis of the primitive unit cell of the fcc Bravais lattice for the coinage metals $N_{\text{prim.}}$ was set to one. The $E_c(a_0)$ data points were approximated by a least squares fit of a fifth order polynomial. The optimal coinage metal lattice constants were obtained from the positions of the local E_c maxima of the fitted polynomials next to the literature values from experiments.
Comparing the literature values of a_0 – drawn as horizontal, dashed lines – to the positions of the $E_c(a_0)$-maxima – drawn as up pointing arrows –, one finds good agreement with the experimental values for copper ($\Delta a^{Cu} \approx 0.02$ Å), whereas the deviations for Ag ($\Delta a^{Ag} \approx 0.06$ Å) and Au ($\Delta a^{Au} \approx 0.08$ Å) are larger. For the cohesive energies for Cu one finds good agreement with the reference value – for Ag and Au on the other hand strong deviances are observed.

3.2 Basis Functions of the Coinage Metal Atoms

For the numerical accuracy of a DFT calculation the properties of the used basis functions are crucial. By Blum et al. [38] for different purposes compilations of atom-centered basis functions and corresponding settings were listed. Depending on the desired accuracy in ground state energy those were categorized as ”light”, ”tight” and ”really_tight” and are shipped as *species defaults* within FHI-*aims*. Here we focus on ”tight” basis functions sets, which should provide an accuracy in total energy of a few meV. For Cu, Ag and Au different ”tight” settings are available with additional tiers to increase accuracy (and also computation costs). Those tiers contain radial functions and their angular momenta labelled as for atomic orbitals. In FHI-*aims* the speed of the calculations is strongly increased by the use of a confining potential that ”cuts off” the basis functions at a certain distance. In the following two sub-section we investigate the convergence of the cohesive energy E_c first by increasing the number of basis functions and then by variations of the confining potential parameters.

3.2.1 Size of the Basis Set

With the ”tight” basis function settings for the coinage metals the different ”tiers” of basis functions were added successively to DFT-calculations of a primitive unit cell, which were performed parallel on sixteen CPUs. The employed computational settings were chosen according to the previous chapters. Additional a $15 \times 15 \times 15$ k-grid was employed. From the results of those simulations via equation 3.1 the cohesive energies E_c for a primitive fcc unit cell were calculated. The differences of the cohesive energy for a specific basis function set compared to the most accurate values (with the highest ”tier” available) are plotted in figure 7 with the corresponding

(a) Cu - copper.

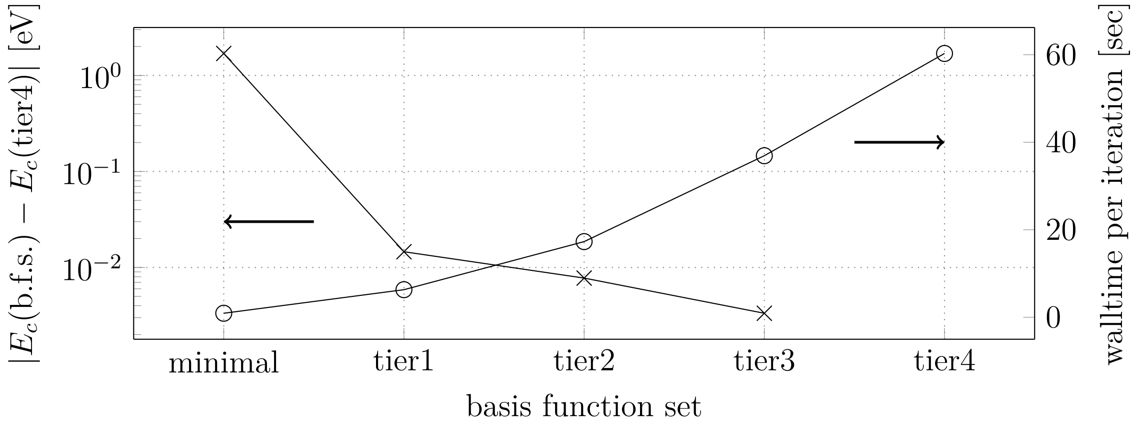

(b) Ag - silver.

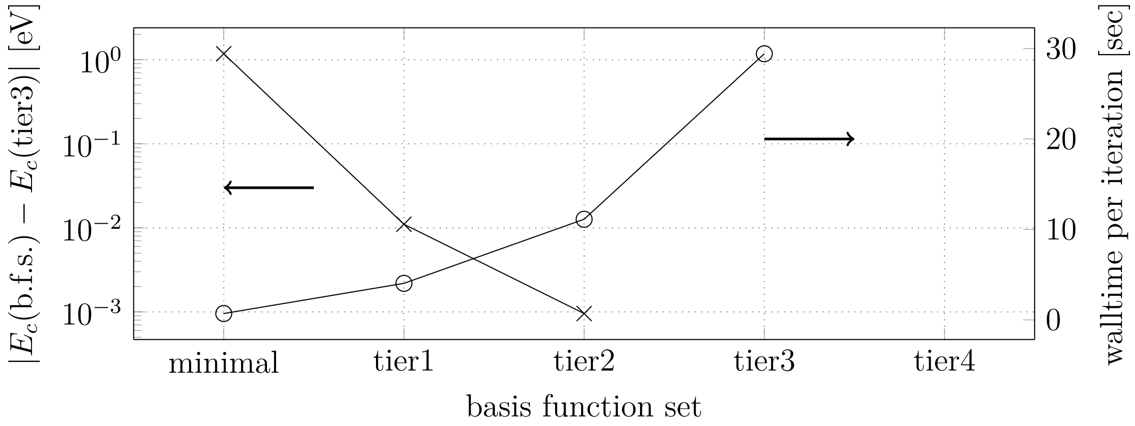

(c) Au - gold.

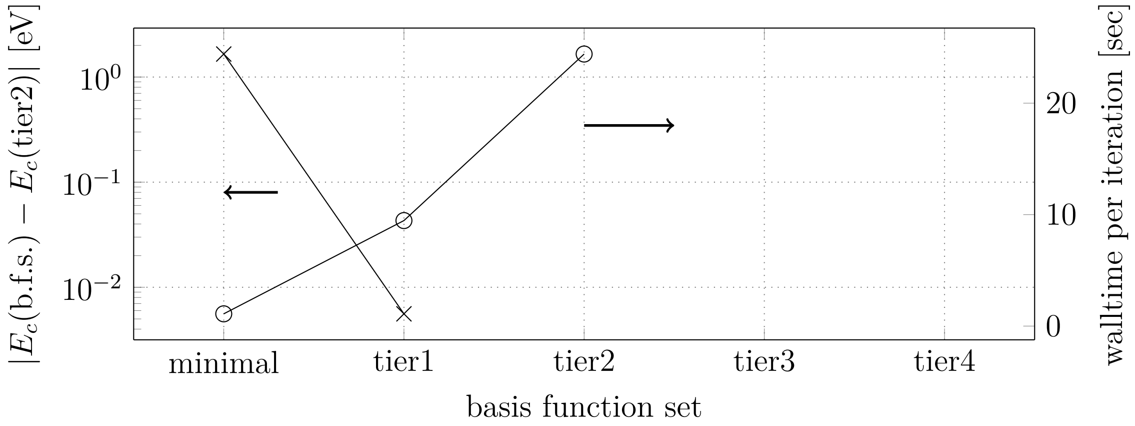

Figure 7: Convergence of the cohesive energy E_c (crosses) for coinage metal crystals calculated with successively enhanced set of basis functions (b.f.s.). Moreover the mean walltime per SCF iteration is plotted (circles). The arrows indicate the axis that belongs to the data set.

mean walltime per SCF iteration.[20]
For copper one finds that the calculation time increases more than a factor of three, if one adds the basis function set ”tier2”. For silver and gold the increase in the calculation times are even larger. Moreover with ”tier1” the cohesive energy difference to the most accurate value for all coinage metals is already smaller than 0.02 eV. To save computing time that especially is crucial for calculations dealing with heavy elements (as gold) or big geometries with hundreds of atoms, hence it is useful to choose just the sets ”minimal” and ”tier1” for the coinage metal basis functions of our DFT calculations.

3.2.2 Parameters of the Confining Potential

The confining potential ensures that the radial functions of the basis set go to zero at at a certain radius, which enables high numerical efficiency. On the other hand with a to small radius of the confining potential numerical accuracy gets decreased. To find appropriate settings for the parameters of the confining potential function convergence tests were performed for the coinage metals. For the test we calculated the work function of a $1 \times 1 \times 6$ repeated slab geometry with a (111)-surface with an over-converged $63 \times 63 \times 1$ k-grid with an offset of $\{0.5, 0.5, 0\}$. The computational settings for the DFT calculations were chosen as described in the previous chapters. By default in FHI-*aims* for the confining potential of the basis functions the following function is used – see Blum et al. [38, equation 9]:

$$v_c(r) = \exp\left(\frac{w}{r - r_{\text{onset}}}\right) \cdot \frac{1}{(r - w - r_{\text{onset}})^2} \tag{3.2}$$

For the different test cases the onset r_{onset} and the width w were increased by the quantity δ from the default setting in a ”tight” basis functions settings with the sets ”minimal” and ”tier1”:

$$r_{\text{onset}} = 4\ \text{Å} + \delta \qquad\qquad w = 2\ \text{Å} + \delta \tag{3.3}$$

The corresponding results are shown in figure 8. With $\delta = 0.6$ Å the residuum is smaller than 0.01 eV for all of the coinage metals. The results further show that also the parameters of the confining potential strongly affect numerical efficiency: Increasing the variation δ by approximately 0.6 Å increases the mean walltime per iteration by about 50 %, 33 % and 20 % for Cu, Ag and Au.

---

[20] Because the number zero cannot be displayed in a logarithmic plot, the number of data points regarding the cohesive energy is by one less than for the mean walltime per iteration.

(a) Cu - copper.

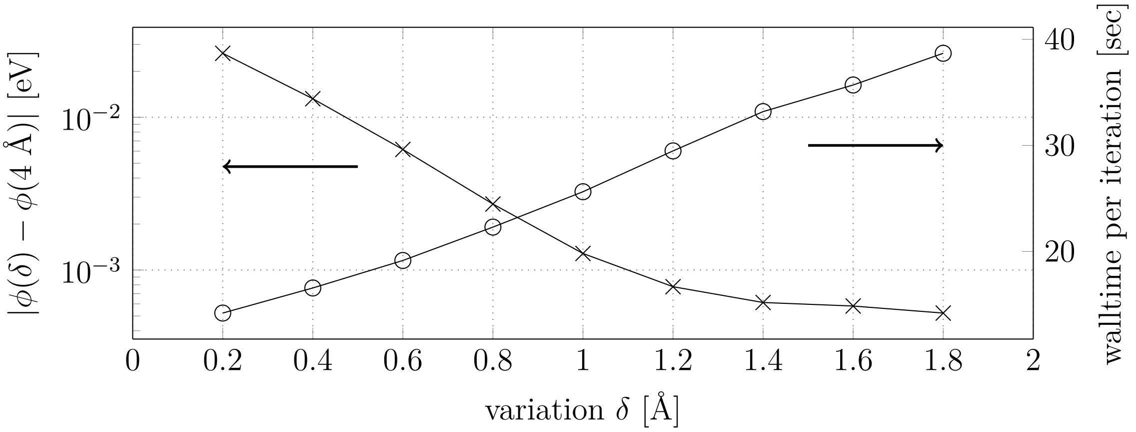

(b) Ag - silver.

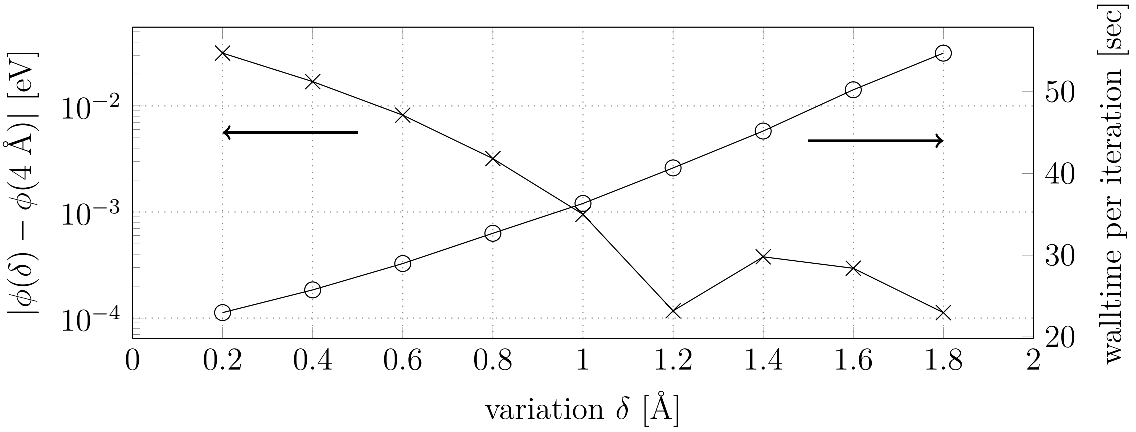

(c) Au - gold.

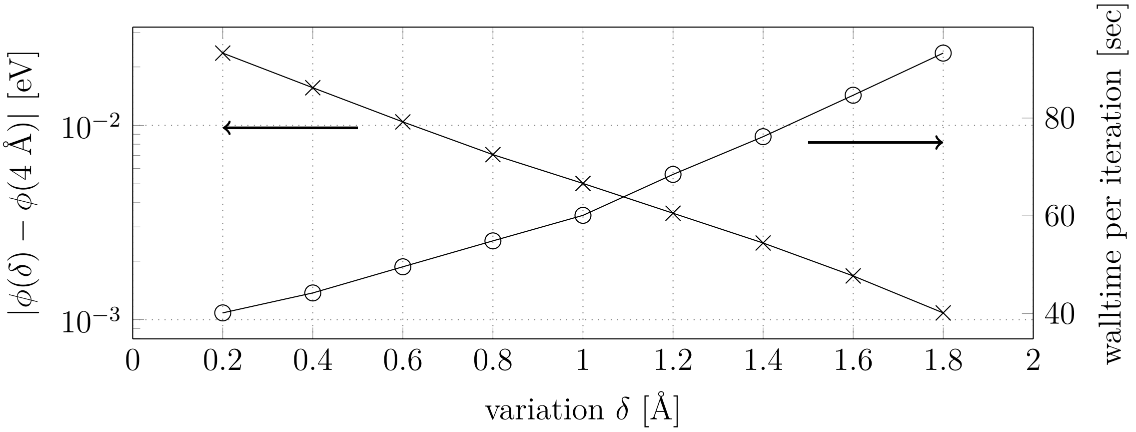

Figure 8: Convergence of the work function regarding the (111)-surface of coinage metal slabs with six layers (crosses) with successively increased onset r_{onset} and width w of the confinement potential. The simultaneous variation of those parameters is denoted by δ. Additionally, the mean walltime per SCF iteration is plotted (circles).

3.3 Repeated Slab Approach

If adsorbed molecules form an ordered layer on the surface of a certain substrate, the interface shows periodicity in two-dimensions of space. To simulate such geometries by DFT customarily the repeated slab approach is used, where just the uppermost layers the of the bulk material are modelled. A sketch of such a repeated slab geometry is shown in figure 9. For simulation of the bulk material the lower layers of the slab are fixed in position, whereas the upper layers are allowed to move in the geometry optimization process. In addition to the obvious periodicity along the interface in repeated slab geometries also perpendicular to the surface periodicity is claimed. This is accomplished by introduction of a vacuum gap of at least 20 Å. To account for different vacuum-levels (VL) above and below the slab that occur if the upper and lower side of the slab are not mirror-symmetric, an artificial dipole correction – compare Freysoldt et al. [65] – is introduced at a certain height above the simulated surface.

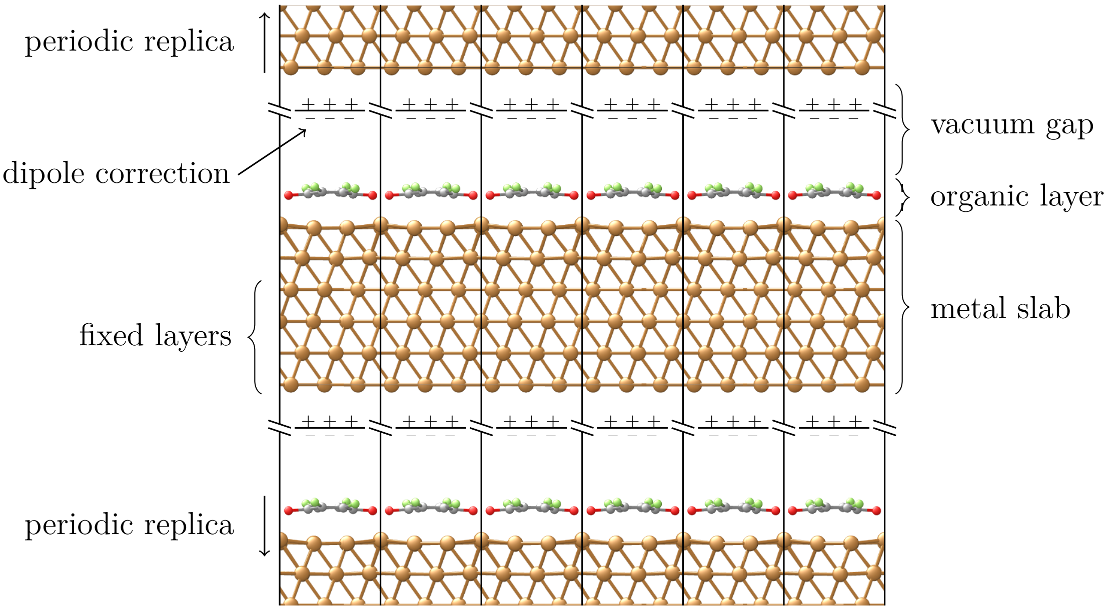

Figure 9: Illustration of the repeated slab approach.

3.3.1 Number of Layers

The impact of the thickness of the slab on the work function was investigated by a set of DFT calculations, where the number of layers was successively increased. The convergence of the work function with increasing number of layers is shown in figure 10. For the DFT calculations a 64 × 64 × 1 Monkhorst-Pack [66] k-grid

(a) Cu - copper.

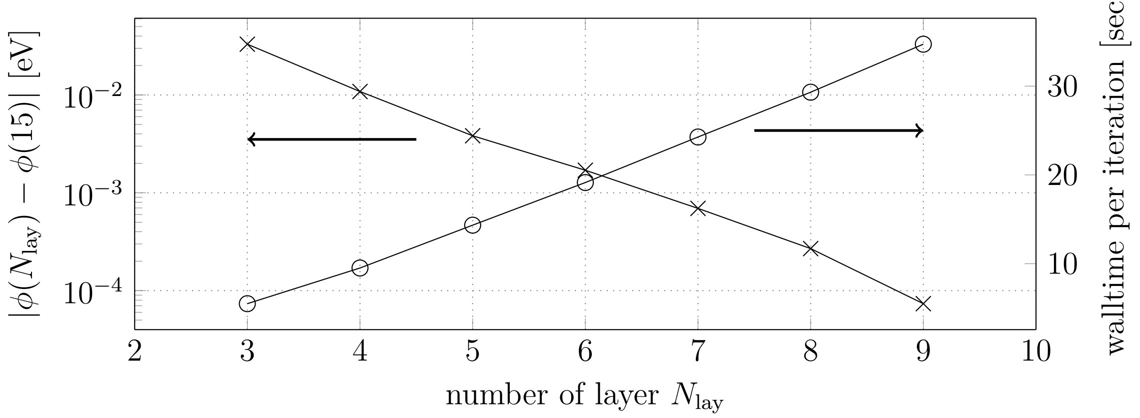

(b) Ag - silver.

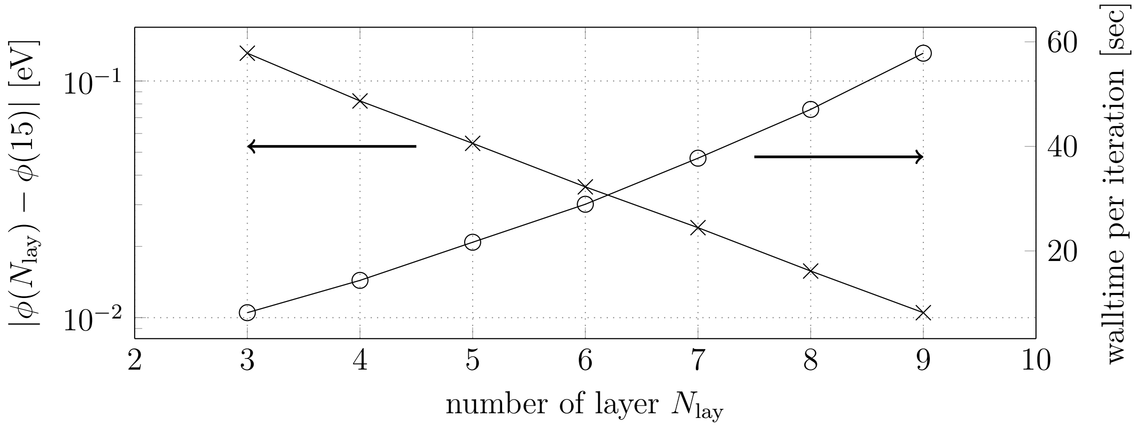

(c) Au - gold.

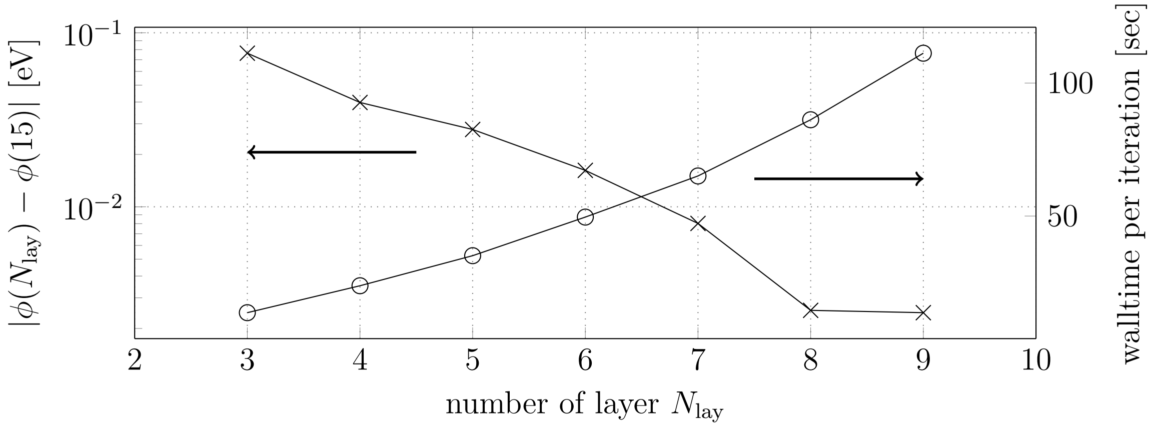

Figure 10: Convergence of the (111)-surface work function (crosses) for the coinage metals with successively increased number of layers. The data points show the work function difference to a slab with $N_{\rm lay} = 15$. Further the mean walltime per SCF iteration is plotted (circles).

was employed for a hexagonal $(1 \times 1\sqrt{3})$ Cu(111) unit cell with variable number of layers. Other computational settings were chosen according to table 2.

From the results of the convergence test it is apparent that for copper with four layers the work function is converged to ≈ 0.01 eV. However, for silver and gold the residuum of the work function is one order of magnitude larger: with six layers the residuum is still ≈ 0.04 eV. Further it is apparent that the mean walltime per iteration significantly increases. For the calculation of charge rearrangements at adsorption of organic molecules[21] the number of layers was increased to six, so that on the lower side of the slab is not affected by charge rearrangements at the upper side.

3.3.2 k-Grid Density

For the k-point grid in this work the scheme of Monkhorst and Pack [66] was employed. In this scheme an offset to the Γ-point is introduced to each direction of reciprocal space $\alpha \in \{x,\ y,\ z\}$ of the magnitude

$$k_{\mathrm{offset},\alpha} = \frac{1}{2} - \frac{1}{2 \cdot n_\alpha}, \tag{3.4}$$

where n_α is the number of reciprocal lattice points along the direction α.[22] The offset causes that the sampling points in the Brillouin zone do not overlap with high symmetry points. For even numbers of k-points n_α the Γ-point is avoided, what enhances the convergence of the ground state energy significantly. In the following therefore only even k-grid numbers, n_α were used.

For the ground state energy and the work function convergence tests were conducted, where n_α was successively increased. The used geometry was a hexagonal 1×1 Cu(111) unit cell of a repeated slab with six layers. Therefore n_x and n_y were varied simultaneously, whereas n_z was set to one. In figure 11 the results of the convergence test are shown.

There one finds that with $n_\alpha = 32$ the difference to the most accurate value ($n_\alpha = 128$) is less than 0.01 eV and that the mean walltime per iteration with respect to $n_\alpha = 2$ is increased by less than 6 %. To accomplish the same accuracy for bigger two dimensional unit cells the k-point grid density had to be scaled appropriately: a $(3 \times 3\sqrt{3})$ Cu(111) unit cell for instance would require a k-grid of $n_\alpha = 10.\dot{6}$. Rounded up to the next even number this gives $n_\alpha = 12$.

---

[21] For details see chapter 5.5

[22] Along the z-direction the offset is zero because $n_\alpha = 1$ in repeated slab simulations.

(a) Cu - copper.

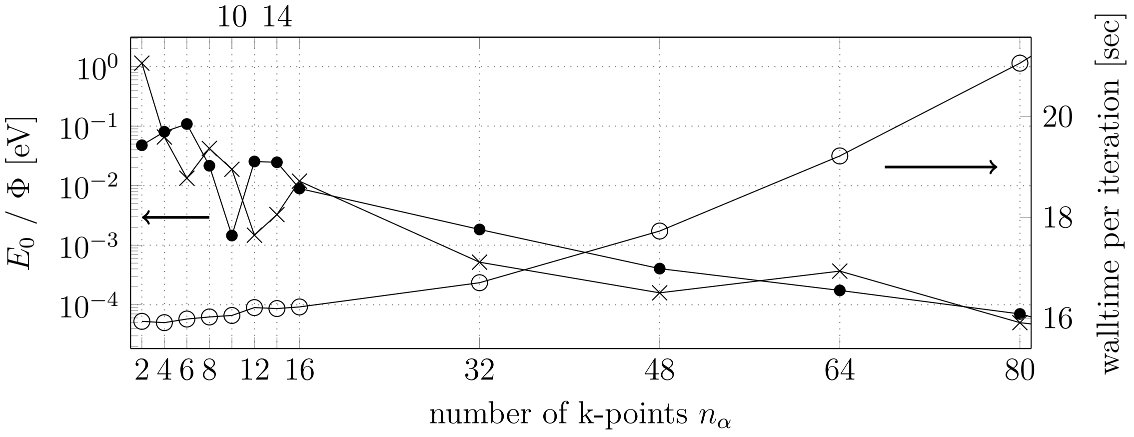

(b) Ag - silver.

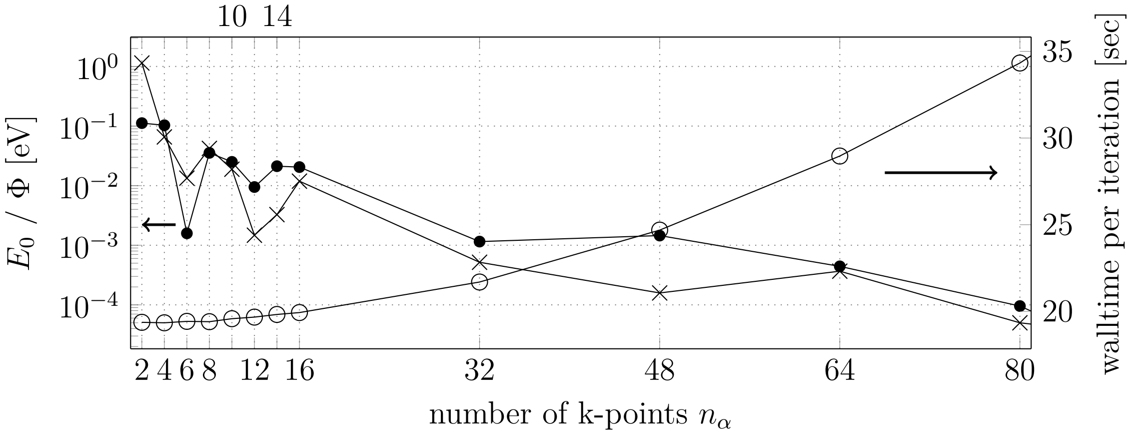

(c) Au - gold.

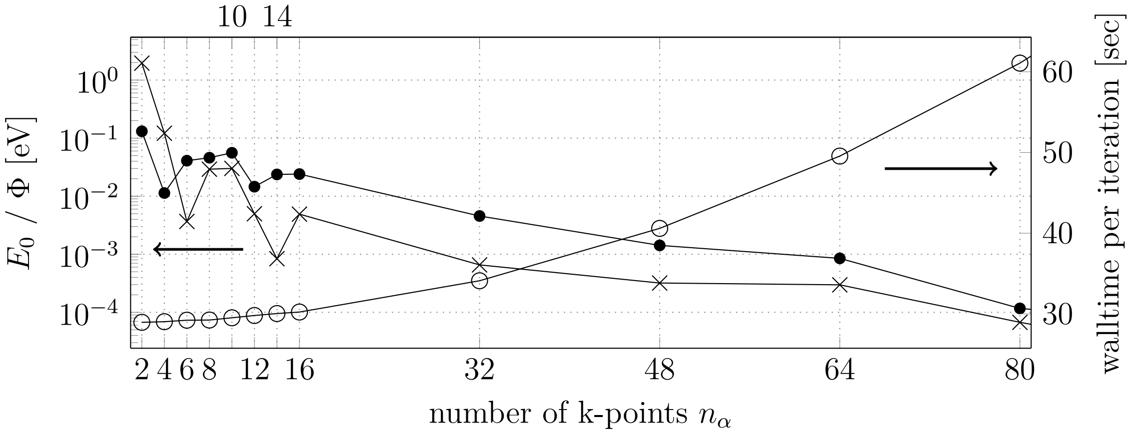

Figure 11: Convergence of the ground state energy E_0 (crosses) and the work function Φ (dots) for coinage metal slabs with six layers calculated with a successively increased number of k-points n_α. Plotted are the absolute differences to respective reference values with $k = 128$. Further the mean walltime per SCF iteration is plotted (circles).

4 Quinones and Hydroquinones

In this section we discuss the properties of organic molecules that were considered as adsorbates on the coinage metal (111)-surfaces. The molecules of choice had to fulfil the following properties:

- Small Size: For the numerical efficiency of interface simulations via DFT the number of involved atoms is crucial. For large molecules also a large number of atoms simulating the adsorbent is needed. Therefore, smaller organic molecules are favourable for the investigation.
- Simple Structure: Simulating the introduction of chemical defects via hydrogenation necessitates a preferably unique conformation of the reduced organic species. Too many possible arrangements can increase the complexity of the system drastically.
- High Electron Affinity (EA): Organic molecules of high EA undergoing charge-transfer reactions on metal electrodes can strongly increase the work-function and, thus, decrease hole injection barriers. An investigation of molecules (with low EA) that hardly show an effect would be less useful for applications.

One class of organic molecules with examples meeting those requirements are acenequinones. Based on Streitwieser et al. [23, chapter 30.8], here we will first discuss general properties of this class of molecules. We then quote EA and ionization potential (IP) values calculated via DFT molecule simulations for various examples of this and other classes that were considered for the investigation. Also related species formed by reaction with hydrogen are discussed.

4.1 General Properties

Generally quinones are compounds having a fully conjugated cyclic dione structure [69]. Examples of acenequinones are 1,4-benzoquinone (BQ) and 6,13-pentacenequinone (PQ) – see chemical structures in figure 12. Many quinones are naturally appearing – for instance fumigatin, alizarin or juglone. They are derived by oxidation of aromatic hydroxyl- or amino-compounds.

The hydrogenated counterparts – so called hydroquinones or diols – to those acenequinones are 1,4-benzenediol (BD) and 6,13-pentacenediol (PD). In general, quinones and hydroquinones form an electrochemically reversible redox-system. The more positive the redox-potential of a certain quinone is, the easier hydro-quinones are formed. An increase of the reduction potential can be obtained, when the electron-donating hydroxyl-groups are exchanged by an electron-accepting substituent such

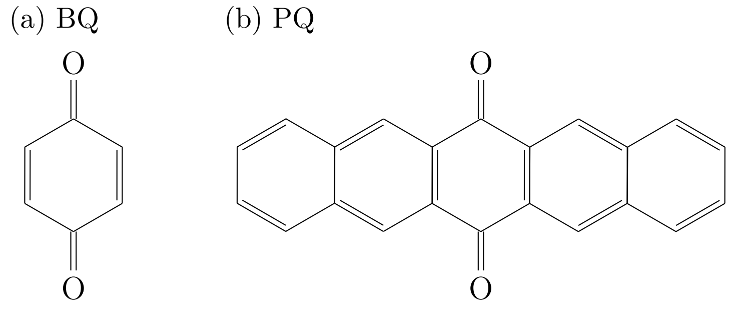

Figure 12: Chemical structures of two acenequinones.

as a halogen. Substituents as fluorine, chlorine or bromine, hence, cause a strong *EA*-increase. For the electrochemical reaction of tetrafluoro-1,4-benzoquinone (TFBQ) – a molecule that has many applications in chemical synthesis [70] – with hydrogen to TFBD the reaction is displayed in figure 13.

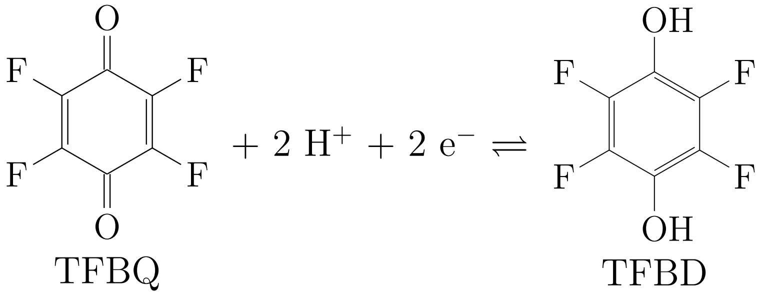

Figure 13: Electrochemical reaction of TFBQ with hydrogen to TFBD.

Mixtures of electron-accepting quinones and electron-donating hydroquinones form solid charge-transfer-complexes. An equimolar mixture of BQ and HQ, for instance, forms the darkgreen crystalline molecule complex chinhydron. In such compounds, the LUMO of the acceptor overlaps with the HOMO of the donor. From this results an electron transfer from the donor to the acceptor. The extent of this charge transfer is usually just a small fraction of an electron (≈ 0.05 e) – see Streitwieser et al. [23, page 1056]. The resulting forces holding the compound to together usually add up to a few kJ mol^{-1}. Charge-transfer-complexes show a characteristic light absorption band – the so-called charge-transfer-band –, which causes intensive colours of the compound, when the transition lies in the visible range.

4.2 Electron Affinity and Ionization Potential

From the DFT calculations regarding the neutral and negatively and positively charged molecule the vertical electron affinity EA and ionization potential IP were calculated. Here ”vertical” indicates that for the geometry of the charged system no additional structure optimization is performed. They were obtained by the equations:

$$EA = E(0\,\mathrm{e}) - E(-1\,\mathrm{e}) \tag{4.1}$$

$$IP = E(+1\,\mathrm{e}) - E(0\,\mathrm{e}) \tag{4.2}$$

$E(0\,\mathrm{e})$	ground state energy of the neutral molecule
$E(-1\,\mathrm{e})$	ground state energy of the negatively charged molecule
$E(+1\,\mathrm{e})$	ground state energy of the positively charged molecule

The resulting EA and IP values for the TFBQ, TFBD and other investigated molecules are listed in table 3. For quinones of high EA a strong work function increase upon adsorption on coinage metal surfaces can expected, due to charge transfer. Therefore, quinones of high EA are preferred for the present investigation.

Table 3: Electron affinity EA and ionization potential IP calculated via equations 4.1 and 4.2 and DFT for isolated TFBQ, TFBD and other possible molecules for the investigations in this thesis. For some species also reference values from experiments are shown.

Molecule	Abbr.	EA [eV]		IP [eV]	
		DFT	Ref.	DFT	Ref.
tetracyanoethylen	TCNE	3.29	3.17 [71]	11.10	11.67 [72]
tetrafluoro-1,4-benzoquinone	TFBQ	2.44	2.45 [73]	9.83	10.96 [74]
1,4-benzoquinone	BQ	1.91	1.85 [75]	9.30	9.99 [74]
6,13-pentacenequinone	PQ	1.63		7.60	
tetrafluoro-1,4-benzenediol	TFBD	0.10		8.44	
1,4-benzenediol	BD	0.81		7.76	8.44 [76]

The highest EA values are found for TCNE and TFBQ. TCNE has the big disadvantage that it by hydrogenation it dissociates into the toxic hydrocyanic acid. TFBQ fulfilled our requirements best.

5 Homogeneous Monolayers

To understand the adsorption properties of mixed monolayers of TFBQ and TFBD, it is instructive to begin with a study of the limiting cases, where the (111)-surfaces of the coinage metals copper and silver are fully covered by either only the acceptor or the donor molecule.

Before showing the results of the investigations, we discuss how the geometries of homogeneous monolayers were obtained. For TFBQ and TFBD on Cu(111) and Ag(111) we then study the morphology of the adsorbate. Furthermore, we perform a quantitative comparison of the work function modification, $\Delta\Phi$, and its contributions from molecular dipoles, ΔE_{mol}, and bond dipoles, ΔE_{bond}, for the different adsorption cases. For the discussion of the bond dipoles we investigate the density of states projected on molecular orbitals and charge rearrangements upon adsorption.

5.1 Geometry Optimization

Previous to TFBQ other molecules were investigated, namely para-1,4-benzoquinone (BQ), 6,13-pentacenequinone (PQ), 5,7,12,14-pentacenetetrone (PT) and tetracyanoethylene (TCNE). For the sake of completeness, in this chapter geometries and values of the work function modification, $\Delta\Phi$, regarding the later discarded molecules BQ, PQ and TCNE are also mentioned. Comparing the work function modifications of various molecules upon adsorption on Cu surfaces we found that TFBQ and TCNE showed the strongest work function increases – see table 4. For BQ, PQ and PT we found that upon adsorption on Cu(111) $\Delta\Phi$ increases hardly compared to the effects of the corresponding hydrogenated species. Thus, for our investigation those molecules were discarded. TFBQ and TCNE showed strong work function increases upon adsorption. Due to ambiguities of the adsorption geometry regarding hydrogenated TCNE, TFBQ was preferred for the investigation. Therefore, in

Table 4: Work function modifications, $\Delta\Phi$ for various molecules adsorbed upon Cu surfaces.

Molecule	Abbr.	Surf.	Geometry	$\Delta\Phi$ [eV]
para-1,4-benzoquinone	BQ	(111)	$(3 \times 3\sqrt{3})$	-0.22
6,13-pentacenequinone	PQ	(111)	$(2\sqrt{3} \times 6)R30.0°$ [22]	-0.71
tetrafluoro-1,4,benzoquinone	TFBQ	(111)	$(3 \times 3\sqrt{3})$	$+0.51$
tetracyanoethylene	TCNE	(100)	(2×2)	$+0.38$

subsequent chapters then the focus is put on TFBQ and its corresponding chemical defect, TFBD, introduced via hydrogenation.

For the BQ molecule that shows structural similarities to TFBQ an extensive investigation was done to find the best two dimensional unit cell and alignment of the molecule. In those investigations after geometry relaxation with "light" settings to a force of 0.03 $\frac{\text{eV}}{\text{Å}}$ the adsorption energy per area ϵ_{ads} was calculated for many unit cells of different size and shape. Some of those geometries were motivated by findings from experiments where monolayers of para-1,4-benzoquinone (BQ) were adsorbed on (111)-surfaces of other face centered cubic crystals. Finally the geometry with largest ϵ_{ads} was chosen. This quantity was calculated via the equation:

$$\epsilon_{\text{ads}} = \frac{E_{\text{ads}}}{A} = \frac{1}{A} \cdot (E_{\text{full}} - E_{\text{mol}} - E_{\text{slab}}) \tag{5.1}$$

E_{full}	total energy of the full system containing the molecule and the slab in the unit cell.
E_{mol}	total energy of the molecule in the unit cell without a slab below, i.e. free-standing monolayer.
E_{slab}	total energy of the slab without any molecule above.
A	area of the unit cell

Those calculations showed that a flat lying orientation of the BQ molecule on the copper slab and a hexagonal two-dimensional Bravais lattice are preferred. The largest adsorption energy was observed for a geometry that was motivated by an experimental investigation of the alignment of BQ adsorbed on Rh(111) by Inukai et al. [77].

Due to the structural similarity of TFBQ to BQ for former just three geometries were investigated that are shown on the next page in figure 14. Geometry (a) is similar to that proposed by Inukai et al. [77]. Geometry (b) was proposed by Kim et al. [78] for the adsorption geometry of BQ on Pt(111). Further a geometry with smaller packing density – namely geometry (c) was investigated. The corresponding adsorption energies are listed in table 5.

For the choice of the unit cell finally two criterions were relevant: First the packing of the molecules should be as close as possible to maximize the area-specific adsorption energy, ϵ_{ads}. Further the molecules should not be packed to dense, to avoid spurious distortions of the molecules. To accomplish this the spacing of the atoms of neighboring molecules were compared to the corresponding vdW radii. Albeit geometry (a) showed the largest adsorption energy, it was not reasonable for TFBQ on Cu(111), because there the distance of the neighboring fluorine atoms of 2.6 Å would be smaller than the sum of the corresponding van der Waals radii

(a) hexagonal; $a = 6.79$ Å; $\alpha \approx 18.1\,^\circ$

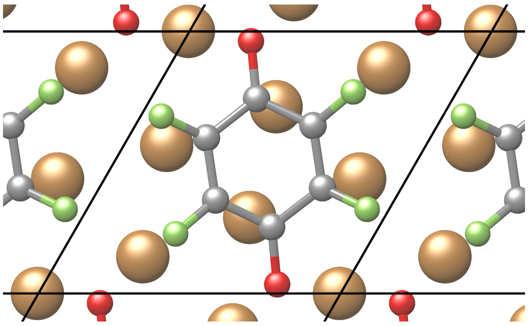

(b) hexagonal; $a = 7.70$ Å; $\alpha = 0\,^\circ$

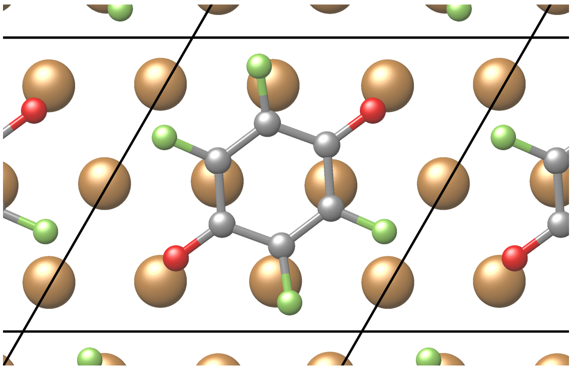

(c) hexagonal; $a = 8.87$ Å; $\alpha = 30\,^\circ$

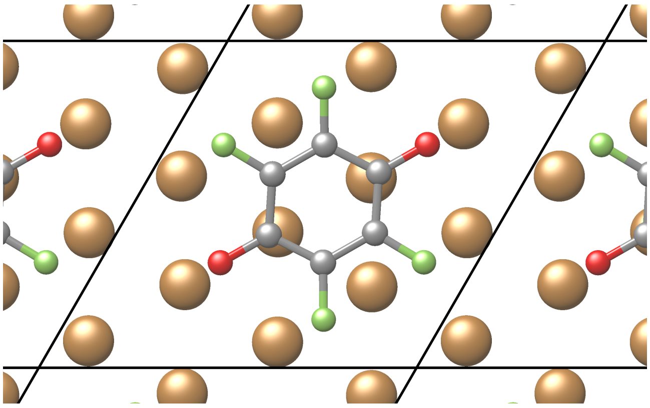

Figure 14: Top views on investigated geometries for TFBQ adsorbed on Cu(111). For each geometry the two-dimensional Bravais lattice the length of the lattice vectors a and the tilting angle α of the $[\bar{1}01]$ direction of copper lattice to the x-direction are given.

Table 5: Adsorption energies per area and unit cell, ϵ_{ads} and E_{ads}, and work function modifications, $\Delta\Phi$, for different geometries of TFBQ adsorbed upon Cu(111).

Label	Geometry	ϵ_{ads} $[\frac{\text{eV}}{\text{Å}^2}]$	E_{ads} $[\frac{\text{eV}}{\text{cell}}]$	$\Delta\Phi$ [eV]
(a)	$(\sqrt{7} \times \sqrt{7})R18.1°$	-0.07	-2.77	$+0.26$
(b)	$(3 \times 3\sqrt{3})R0.0°$	-0.05	-2.60	$+0.53$
(c)	$(4 \times 4\sqrt{3})R0.0°$	-0.04	-2.58	$+0.51$

of $2 \cdot 1.35$ Å – smallest estimation that appears in the publication of Batsanov et al. [79]. Outweighing adsorption energy against packing density, thus, we decided that for TFBQ adsorption upon Cu(111) from the investigated set geometry (b) is the best choice.[23]

For Ag(111) a similar course of the adsorption energy with packing density was expected. Due to the larger lattice constant of bulk silver for geometry (a) the lattice vector, $a = 7.77$ Å, and, hence, the spacing of the molecules is even slightly larger than for geometry (b) with a copper slab. Therefore, for Ag(111) geometry (a) was chosen – see figure 15.

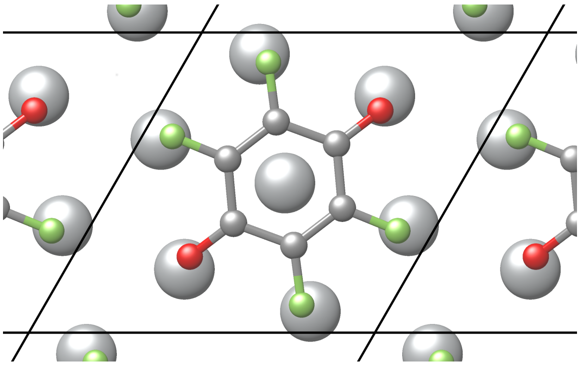

Figure 15: Top view on geometry (a) for TFBQ adsorbed on Ag(111). Comparing the alignment of the molecule to the upper metal layer for this geometry and the original proposed by Inukai et al. [77], one finds that here the molecule is rotated by −30° to obtain a larger distance between the oxygen atoms and, thus, a gain in adsorption energy.

---

[23] The distance of fluorine atoms of neighboring TFBQ molecules is about 3.1 Å.

5.2 Structural Properties[24]

The side views on homogeneous monolayers of TFBQ and TFBD adsorbed upon Cu(111) and Ag(111) are displayed in figure 16. The corresponding adsorption heights are listed in table 6.

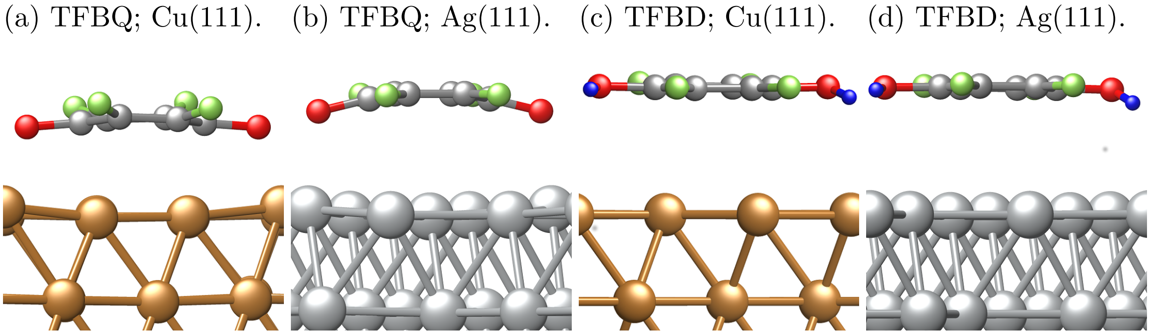
(a) TFBQ; Cu(111). (b) TFBQ; Ag(111). (c) TFBD; Cu(111). (d) TFBD; Ag(111).

Figure 16: Side views on adsorption geometries of homogeneous monolayers after geometry optimization: (a) TFBQ on Cu(111), (b) TFBQ on Ag(111), (c) TFBD on Cu(111) and (d) TFBD on Ag(111).

Table 6: Mean adsorption distances, d_X, of the atomic species, X, to the relaxed, uppermost metal layers and adsorption energies, E_{ads}, for homogeneous monolayers of TFBQ and TFBD on Cu(111) and Ag(111) at full coverage. The adsorption energy per molecule $E_{\mathrm{ads}} = \epsilon_{\mathrm{ads}} \cdot A$ was calculated via equation 5.1.

Substr.	Mol.	d_{H} [Å]	d_{C} [Å]	d_{O} [Å]	d_{F} [Å]	E_{ads} [eV]
Cu(111)	TFBQ	-	2.30	2.10	2.60	-2.6
Ag(111)	TFBQ	-	2.83	2.46	2.85	-1.5
Cu(111)	TFBD	2.89	3.03	3.06	3.07	-0.9
Ag(111)	TFBD	2.86	3.09	3.05	3.12	-0.9

On Cu (Ag) the adsorption distance of TFBQ is about 0.7 Å (0.4 Å) smaller than for TFBD. This is in congruency with the results of Duhm et al. [17], who investigated PTCDA adsorbed upon (111)-surfaces and found that d_{ads} decreases with increasing reactivity of the metal substrate. Further, the planar structure of TFBQ is significantly distorted upon adsorption for both Cu(111) and Ag(111). On Cu(111) the carbon backbone of TFBQ is located between the oxygen and fluorine atoms, whereas on Ag(111) it is lifted to the height of the fluorine atoms. Exchanging

---

[24] This section contains contents of Edlbauer et al. [1, Paragraph "Properties of Homogeneous Monolayers."]

Cu(111) with Ag(111) the adsorption distance regarding the oxygen and fluorine atoms of TFBQ increases by about 0.2 Å. Contrary, TFBD remains planar and adsorbs at a distance of approximately 3 Å for both coinage metal surfaces – except for the hydrogen atoms located 0.2 Å below.

5.3 Molecular and Bond Dipoles[25]

The work function, Φ, of a metal electrode is one important factor determining the magnitude of charge-injection barriers. Φ is modified via adsorption of organic molecules by the formation of dipoles shifting the VL above the slab:

$$\Delta\Phi = \Delta E_{\mathrm{mol}} + \Delta E_{\mathrm{bond}} \tag{5.2}$$

ΔE_{mol}	energy shift due to molecular dipoles of the adsorbate perpendicular to the surface (molecular distortions are crucial). It is calculated from the vacuum-level shift introduced by the hypothetically, free standing monolayer.
ΔE_{bond}	modification of Φ due to charge rearrangements upon adsorption, called bond dipole. Here this value is calculated simply by subtraction of ΔE_{mol} from ΔΦ.

The values for ΔΦ and its contributions from charge rearrangements and molecular dipoles are given in table 7. TFBQ strongly increases Φ upon adsorption due to its high *EA* causing Fermi-level-pinning. Furthermore on Ag(111) ΔE_{mol} gives a significant contribution to ΔΦ, whereas on Cu(111) a molecular dipole is hardly present. Despite the strong distortion of TFBQ upon adsorption, on Cu(111) ΔE_{mol} is very

Table 7: Quantitative comparison of the contributions to ΔΦ from charge rearrangements, ΔE_{mol}, and molecular dipoles, ΔE_{bond}, for TFBQ and TFBD adsorption upon Cu(111) and Ag(111) corresponding to equation 5.2.

Substrate	Molecule	ΔΦ [eV]	ΔE_{bond} [eV]	ΔE_{mol} [eV]
Cu(111)	TFBQ	+0.5	+0.5	+0.0
Ag(111)	TFBQ	+0.6	+1.1	−0.5
Cu(111)	TFBD	−0.4	−0.7	+0.3
Ag(111)	TFBD	−0.3	−0.6	+0.3

---

[25] This section contains contents of Edlbauer et al. [1, Paragraph "Properties of Homogeneous Monolayers"].

small, because there the contributions to the formation of the molecular dipole from the partial charges of the fluorine and oxygen atoms, located above and below the carbon atoms, cancel each other out. Therefore, for TFBQ on Cu(111) no formation of a molecular dipole contributing to $\Delta\Phi$ occurs. On Ag(111) the carbon backbone is located at about the same height as the fluorine atoms. With the negative partial charges at the oxygen atoms of TFBQ, ΔE_{mol} results to a considerable contribution of -0.5 eV. Interestingly, the magnitude of ΔE_{bond} on Ag(111) is twice as big than on Cu(111). This likely is also caused by the different positions of the carbon backbone for TFBQ adsorption on Cu(111) and Ag(111). Hofmann et al. [41] showed that molecular dipoles that are located in the region of Fermi-level-pinning-induced charge rearrangements are compensated by variations in the charge-transfer dipoles arising from the metal-molecule interaction. The increased height of the carbon backbone increases the molecular dipole built up with the oxygen atoms that lies in the spatial region of charge-rearrangements caused by Fermi-level-pinning. Accordingly, the compensation of that molecular dipole is reflected in the large value of ΔE_{bond} on Ag(111).

For TFBD, on the other hand, we find quite similar contributions to the molecular dipole of $\Delta E_{\mathrm{mol}} = +0.3$ eV for the different coinage metal surfaces that are caused by the molecular dipole of the rotated OH-group. Also the negative values ΔE_{bond} just deviate weakly (by about 0.1 eV) for TFBD on Cu(111) and Ag(111).

In the following sections we discuss the electronic properties leading to the ΔE_{bond} values.

5.4 Molecular Orbital Projected Density of States

To get a more detailed view on the electronic properties of homogeneous monolayers of TFBQ and TFBD upon adsorption on Cu(111) the density of states (DOS) was calculated and projected on the molecular orbitals – compare Romaner et al. [16], Hoffmann [80] and Hughbanks et al. [81]. This allows an identification of the peaks in the DOS of the adsorbate and gives insight on the effects causing charge rearrangements. By integration of the MODOS of a certain molecular orbital from $-\infty$ to E_F additionally the occupation of the molecular orbitals was calculated.

The MODOS and occupation of the molecular orbitals for TFBQ adsorption upon Cu(111) is shown in figure 17a and figure 17b. The TFBQ-MODOS illustrates that upon adsorption on Cu(111) the molecular orbitals hybridize strongly causing a distribution of the peaks ranging over a few eV – see for instance the HOMO-peak in figure 17a. The broadening stems from the strong interaction of TFBQ with copper where distinct electronic states of the molecule couple to continuously

(a) Density of states projected on molecular orbitals (MODOS).

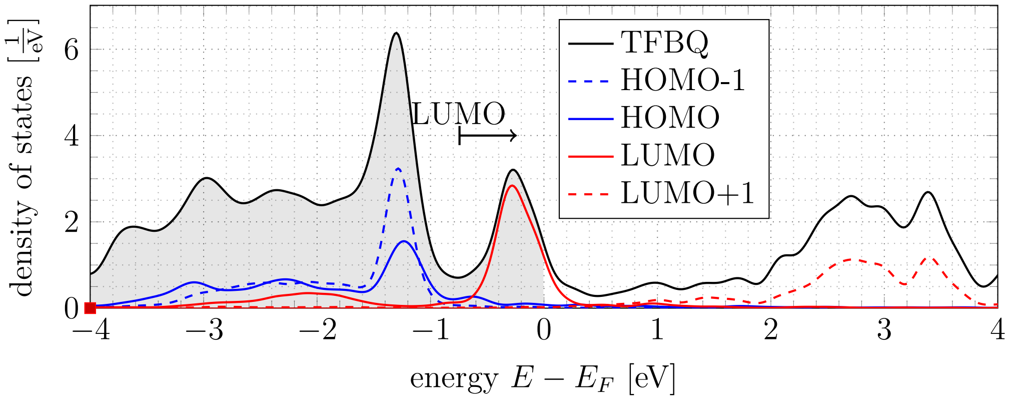

(b) Occpation of the molecular orbitals.

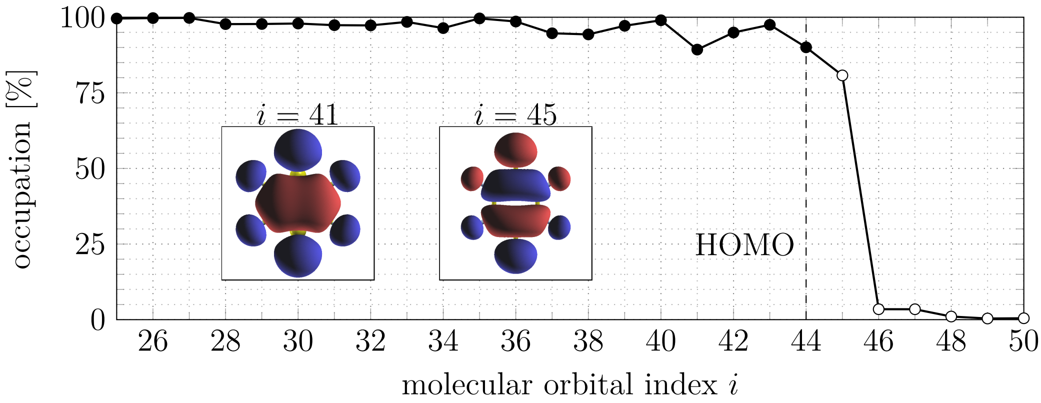

(c) MODOS of weakly depopulated molecular orbitals ($i \in 37, 38, 41$). For comparison further a fully occupied orbital ($i = 27$) is plotted.

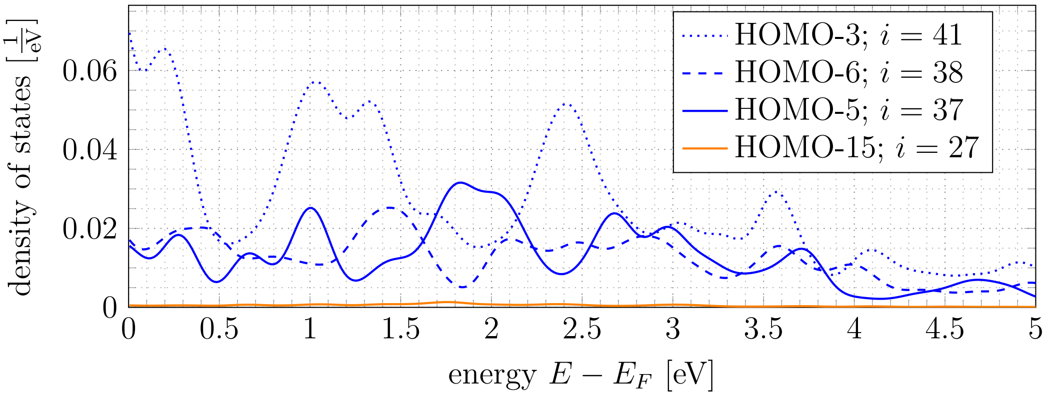

Figure 17: (a) MODOS for TFBQ adsorbed upon Cu(111) with (b) corresponding occupation of the molecular orbitals. The inlay graphics show iso-density plots of the orbitals 41 and 45. (c) Strongly hybridized orbitals on a different scale. The bold, horizontal arrow dawn in (a) the MODOS-plot indicates the pinning-induced shift of the LUMO from the charge-rearrangements in the plate-capacitor model (for details see text).

distributed states of the metal. Further one finds that the peak of the LUMO-peak is shifted to ≈ -0.28 eV below E_F and hence is occupied by ≈ 80 %, as shown in figure 17b at the corresponding orbital index ($i = 45$).

Considering the separated systems of a hypothetically, free standing TFBQ-monolayer (FSM) and a metal slab, for Fermi-level-pinned systems one finds that the LUMO has an energy lower than E_F relative to VL. Upon adsorption, thus, the LUMO gets filled and a dipole is formed, which shifts the LUMO to higher energies, until it gets in resonance with E_F (see corresponding density of states in figure 17a). This effect that is also known as Fermi level pinning leads to a metal-to-molecule electron transfer. But the observed charge transfer (compare section 5.5) is much lower than one would expect from the filling of the LUMO: From the occupation of the LUMO by simple electrostatic considerations – of a point charge with 2.3 Å distance to the surface – one would expect a strong dipole formation of ≈ 3.7 eÅ and a corresponding high work function increase of ≈ 3.7 eV that actually is not observed in the results of the DFT calculations. As in the findings of Romaner et al. [16] this deviation from the first expectation results from many deep lying (HOMO) orbitals that get slightly depopulated. For TFBQ on Cu(111) for instance the orbitals with the indices 37, 38, 41 and 44 show an occupation smaller than 95 %. Due to the scaling of the ordinate this depopulation is not visible in figure 17a. In figure 17c the MODOS of those depopulated HOMO orbitals is shown on a smaller scale: We find that those orbitals are distributed over energies far beyond E_F and that they spread over a broad range of energy leading to a non-negligible depopulation despite the small magnitude of the corresponding MODOS. For comparison in figure 17c also a completely filled orbital (HOMO-15, $i = 27$) is plotted, which shows approximately no MODOS for energies above E_F.

For a dense packing of the molecules as present for the homogeneous monolayers discussed here, the adsorption induced charge rearrangements resemble the electrostatic model of a plate capacitor – compare section 2.2.2. In such a system the shift of the LUMO in the Schottky-Mott-limit is approximately given by the magnitude of the bond dipole if the LUMO is modelled as a Delta-Distribution. To show this we calculated the LUMO energy relative to the lower vacuum level for the hypothetically, free-standing monolayer – that is the LUMO-energy in the aforementioned Schottky-Mott-limit where the system is separated in it's semiconducting and metallic sub-systems. The shift of the LUMO in the Schottky-Mott-limit by the bond dipole that would theoretically apply if the LUMO does not broaden and if all of the charge-rearrangements occur below the pinning-induced region is shown as bold, horizontal arrow in figure 17a. The positions of the LUMO predicted by the plate-capacitor model indeed shows good agreement with the position of the

LUMO-peak in the MODOS. However, due to the broadening of the LUMO and dipoles above the pinning-induced region a small deviation is present.[26]

The MODOS for a homogeneous monolayer adsorbed upon Ag(111) is shown in figure 18a. Contrary to adsorption upon Cu(111) on Ag(111) the broadening of the MODOS-peaks is smaller due to the lower reactivity of the metal. Here the position of the LUMO-peak is close to the Fermi-edge giving an occupation of 45 % – see figure 18b. From the work function difference of the two coinage metal surfaces ($\Phi_{\mathrm{Cu(111)}} - \Phi_{\mathrm{Ag(111)}} = 0.42$ eV) in the Schottky-Mott limit one would expect, that

(a) Density of states projected on molecular orbitals (MODOS).

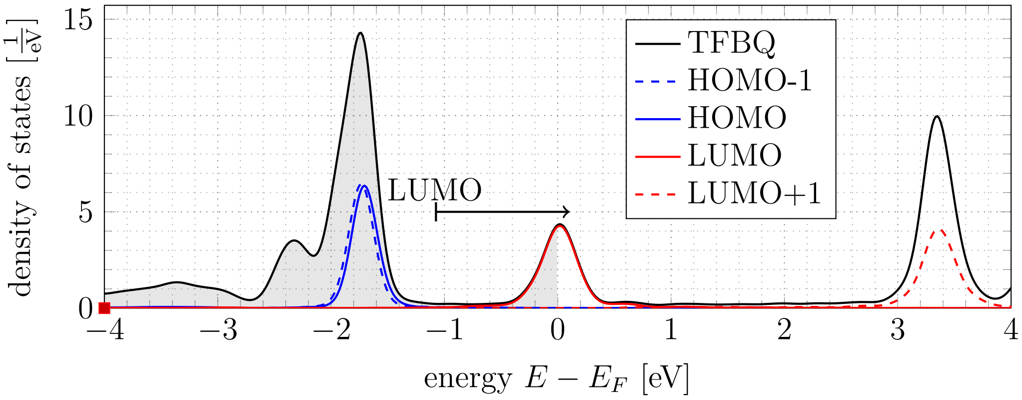

(b) Occupation of the molecular orbitals.

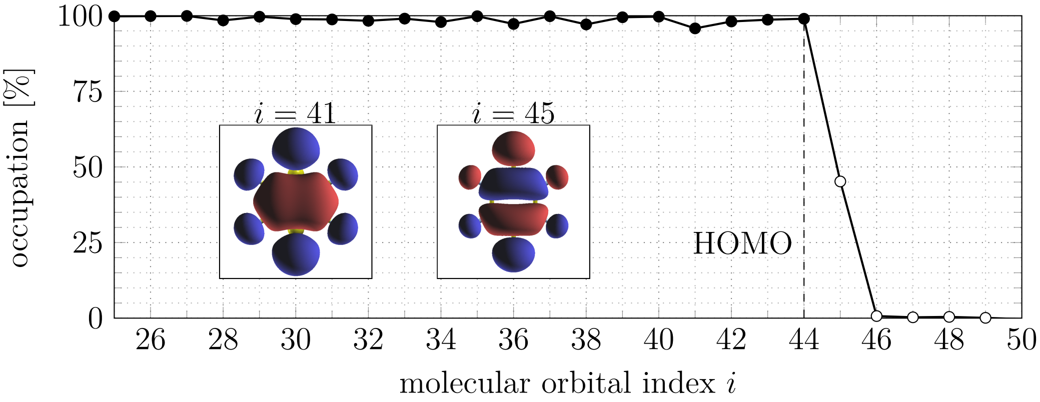

Figure 18: (a) MODOS for TFBQ adsorbed upon Ag(111) with (b) corresponding occupation of the molecular orbitals. The bold, horizontal arrow dawn in (a) the MODOS-plot indicates the pinning-induced shift of the LUMO from the charge-rearrangements in the plate-capacitor model (for details see text). The inlay graphics in (b) the occupation-plot show iso-density plots of the orbitals 41 and 45.

---

[26] Note that for lower coverages and mixed monolayers this picture collapses due to the lateral inhomogeneity of the electron potential distribution – see sections 6.7.2 and 6.7.3.

on Ag(111) the LUMO-peak in the MODOS would lie at an energy lower that on Cu(111), what actually is not observed. Leaving the Schottky-Mott picture and considering the adsorbed TFBQ-molecules, however, one has to expect that the LUMO is also shifted down in energy by the potential caused by Pauli-pushback and HOMO-hybridization. Due to the smaller reactivity of Ag(111) and the higher adsorption distance of TFBQ on Ag(111) the also the potential of Pauli-pushback and HOMO-hybridization and, thus, the shift of the LUMO is much smaller on Ag(111), what may explain the position of the LUMO-peak in the MODOS.

The Fermi-level pinned LUMO-peak predicted by the aforementioned plate-capacitor model and the LUMO energy in the Schottky-Mott-limit are again indicated as a bold arrow.[27]

For the adsorption of TFBD, a different phenomenon is predominant for the work function change: In the density of states of the adsorbed molecule here no peak is present at or close to E_F. In the corresponding MODOS that is shown in figure 19a a band gap of ≈ 3 eV is apparent which separates the HOMO and the LUMO of the TFBD molecule. This indicates that the work function decrease is only caused by the Pauli pushback effect (also known as cushion effect) – for details see chapter 2.2.2. There, the electron density above the copper surface spilling out into vacuum is pushed back due to the presence of the electrons of the adsorbed species. This is reflected in the occupation of the molecular states – see figure 19b: the unoccupied orbitals of the pristine molecule stay empty upon adsorption, whereas the peaks associated with occupied orbitals are completely filled. An indication for weak interaction with the metal is that the energy distribution of the MODOS-peaks here is much more narrow than for the unhydrated species TFBQ, because the hybridization for adsorption of TFBD is much smaller that for TFBQ.[28]

---

[27] Comparing the energies of the LUMO in the hypothetically, free-standing monolayers one finds a deviance that occurs due to the different morphologies of the layers that occur on Cu(111) and Ag(111). This causes that the pinning-induced energy TFBQ-LUMO-peak on Ag(111) is closer to E_F than on Cu(111). From the work functions of the Cu(111)- and Ag(111)-surfaces (about 4.8 eV and 4.4 eV) the reverse situation would be expected.

[28] For TFBD adsorption upon Ag(111) the results regarding the DOS of the adsorbate is very similar – also a band gap of about 3 eV occurs. The corresponding MODOS is not shown here because a gain of new insights is not expected from this information – compare corresponding DOS-plot for mixed monolayers in chapter 6.4.

(a) Density of states projected on molecular orbitals (MODOS).

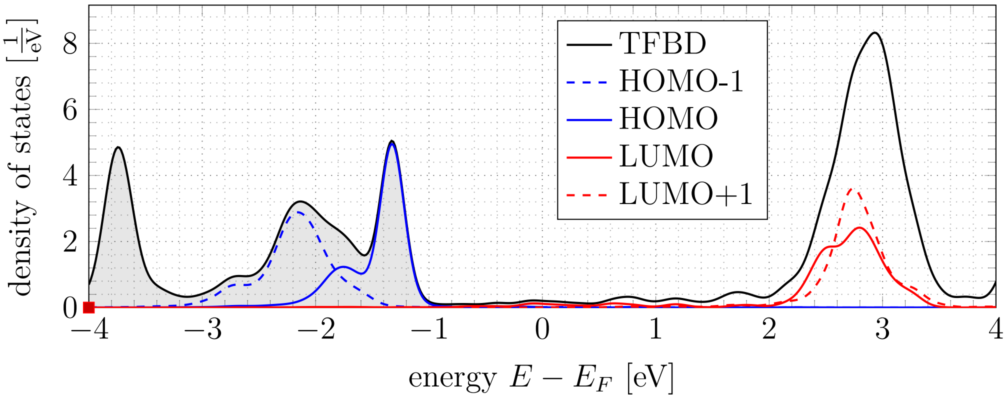

(b) Occupation of the molecular orbitals.

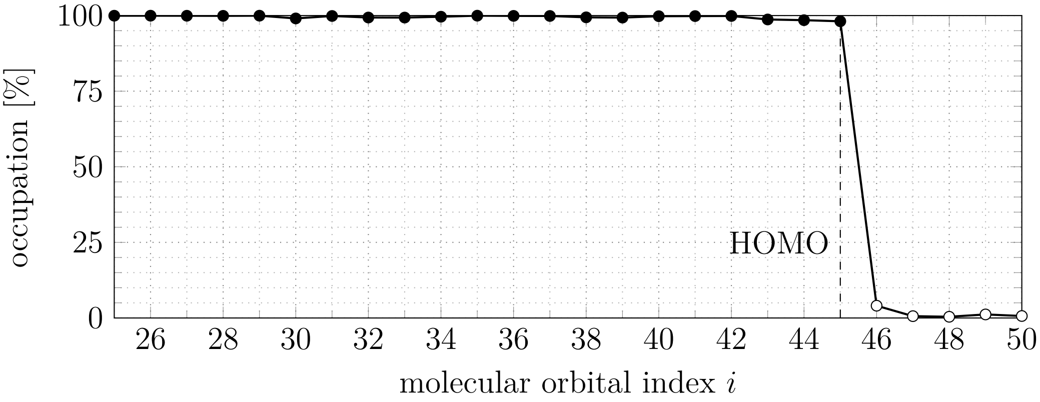

Figure 19: (a) MODOS for TFBD adsorbed upon Cu(111) with (b) corresponding occupation of the molecular orbitals.

5.5 Adsorption-Induced Charge Rearrangements

With the adsorption of organic molecules on surfaces charge rearrangements occur reflecting bond dipole formation. For adsorption of homogeneous monolayers of TFBQ and TFBD upon Cu(111) and Ag(111) surfaces those charge rearrangements are investigated in more detail in the following. The investigation follows the works of Heimel et al. [82] and Hofmann et al. [24] via the charge rearrangements $\Delta\rho(z)$ at a certain height, z, that are obtained by plane-integration over the area A of the unit cell:

$$\Delta\rho(z) = \iint_A \Delta\rho(\vec{r})\, dx\, dy, \tag{5.3}$$

$\Delta\rho(\vec{r})$ describes the charge rearrangement at a certain spatial position, $\vec{r} = (x, y, z)$, that is calculated by:

$$\Delta\rho(\vec{r}) = \rho_{\text{system}}(\vec{r}) - \rho_{\text{slab}}(\vec{r}) - \rho_{\text{monolayer}}(\vec{r}), \tag{5.4}$$

with

$\Delta\rho(\vec{r})$	charge rearrangement at a certain spatial position $\vec{r}$.
$\rho_{\text{system}}(\vec{r})$	electron density of the full system.
$\rho_{\text{slab}}(\vec{r})$	electron density of the metal slab without any molecules upon.
$\rho_{\text{monolayer}}(\vec{r})$ ...	electron density of the monolayer without any metal slab below.

From this quantity by integration from the bottom of the cell to a certain height z the cumulative charge transfer $Q(z)$ can be calculated – compare Stadler et al. [83]:

$$Q(z) = \int_0^z \Delta\rho(\tilde{z})\, d\tilde{z} \tag{5.5}$$

This value describes how much charge is shifted from the region above a plane at a certain height z to the region below that plane due to the adsorbate. From $-Q(z)$ the charging of the molecule due to adsorption can be estimated by the magnitude of the largest peak located between the surface and the molecule.

For the calculation of those quantities the thickness of the metal slabs was set to six layers so that no charge rearrangements appeared at the lower side of the slab and that appropriate simulation of bulk copper was ensured. The settings of the calculations were chosen as described in chapter 3.

The charge rearrangements at adsorption of TFBQ upon Cu(111) and Ag(111) are shown in figure 20. For the two coinage metals the different courses of the charge rearrangements are apparent. For adsorption of TFBQ upon Cu(111) – see figure 20a – $\Delta\rho(z)$ shows four large peaks: Charge is depleted above the copper surface at a height $z \approx 0.9$ Å and in the σ-system of the molecule at $z \approx 2.3$ Å due to Pauli pushback. Mostly charge is transferred to the π-system of the TFBQ-molecule. Therefore two broad positive peaks are apparent at $z \approx 1.7$ Å and $z \approx 2.7$ Å. Due to the charge depletion above the surface and the accumulation on the adsorbate the formation of a positive bond dipole, $\Delta E_{\text{bond}} = 0.5$ eV, takes place. On Ag(111) also charge depletion occurs above the surface – see negative $\Delta\rho(z)$ peak at $z \approx 0.9$ Å in figure 20b.

On Ag(111), however, from the plane-averaged rearrangements we find mainly charge accumulated in the lower lobe of the molecular π-system. On the first sight here a charge depletion peak of the molecules σ-system is not apparent. Comparing $\Delta\rho(\vec{r})$ – see iso-density plots for TFBQ adsorption on Cu(111) and Ag(111) in figure 21a and 21b – we find two qualitative differences: The charge depletion zone at the σ-system of the carbon backbone seems to weaker than on Cu(111) what occurs due to the increased adsorption height mitigating Pauli pushback. Furthermore, on Ag(111) the carbon backbone lies at about the same height as the fluorine atoms. This causes that the charge accumulation in the upper lobes of the π-system is partially compensated by depletion of the σ-system what is reflected in the plane-averaged charge rearrangements.

The larger charge transfer to the molecule and the increased adsorption height results in a bond dipole of $\Delta E_{\text{bond}} = 1.1$ eV. Further it is apparent that considerable charge rearrangements also occur below the uppermost metal layer indicating chemical interaction.

The net charging of TFBQ upon adsorption on Cu(111) and Ag(111) can be determined from the $Q(z)$-plots by the heights of the peaks between the metal surface and the molecule. The corresponding values of $Q^{\text{min}} = -0.18$ e and $Q^{\text{min}} = -0.26$ e are in good agreement with the charges calculated via the Mulliken partitioning scheme – for details see chapter 2.1.5 – of $q = -0.17$ e and $q = -0.26$ e.

For TFBD the charge rearrangements at adsorption upon Cu(111) and Ag(111) are shown in figure 22. Here the course of the charge rearrangements, $\Delta\rho(z)$, are qualitatively similar for adsorption on the different coinage metal substrates: Accumulation occurs directly above the metal surface with a maximum at a height of $z = 0.7$ Å. Depletion occurs at the molecular π-system with minima at $z = 2.6$ Å and $z = 3.5$ Å. The course of $\Delta\rho(z)$ shows nicely that the electron spill out into vacuum from the metal surface is pushed back due to the physisorption of the TFBD molecule. From the $Q(z)$ peak the charging of the molecule can be determined as $Q^{\text{max}} = +0.14$ e and $Q^{\text{max}} = +0.10$ e for adsorption on Cu(111) and Ag(111). The charges calculated via the Mulliken scheme are $q = +0.14$ e and $q = +0.08$ e.

(a) Charge rearrangements, $\Delta\rho(z)$, for TFBQ adsorption on Cu(111).

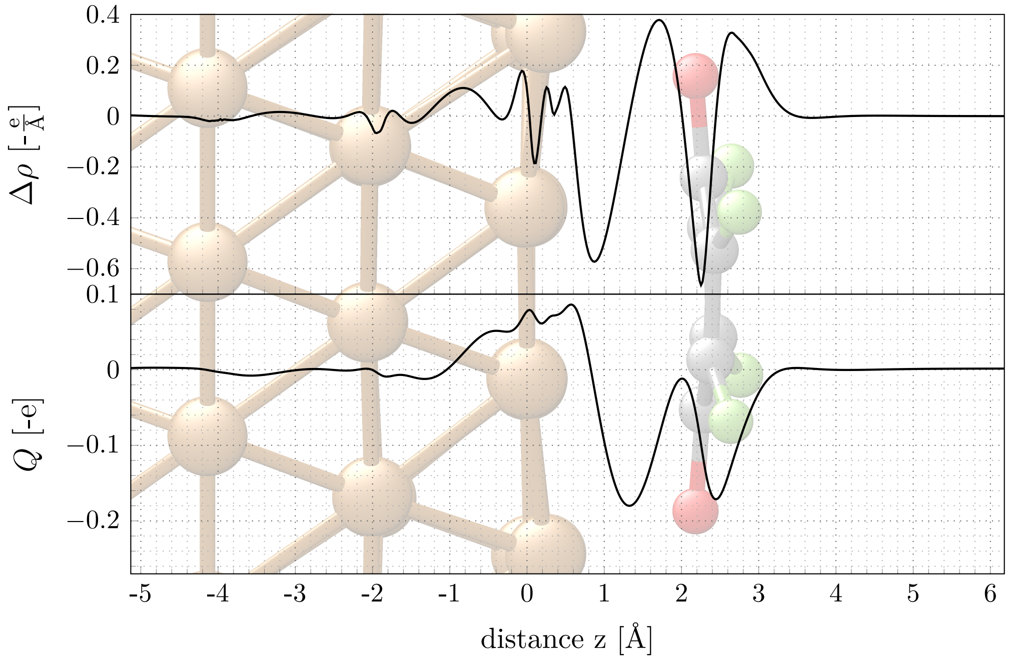

(b) Charge rearrangements, $\Delta\rho(z)$, for TFBQ adsorption on Ag(111).

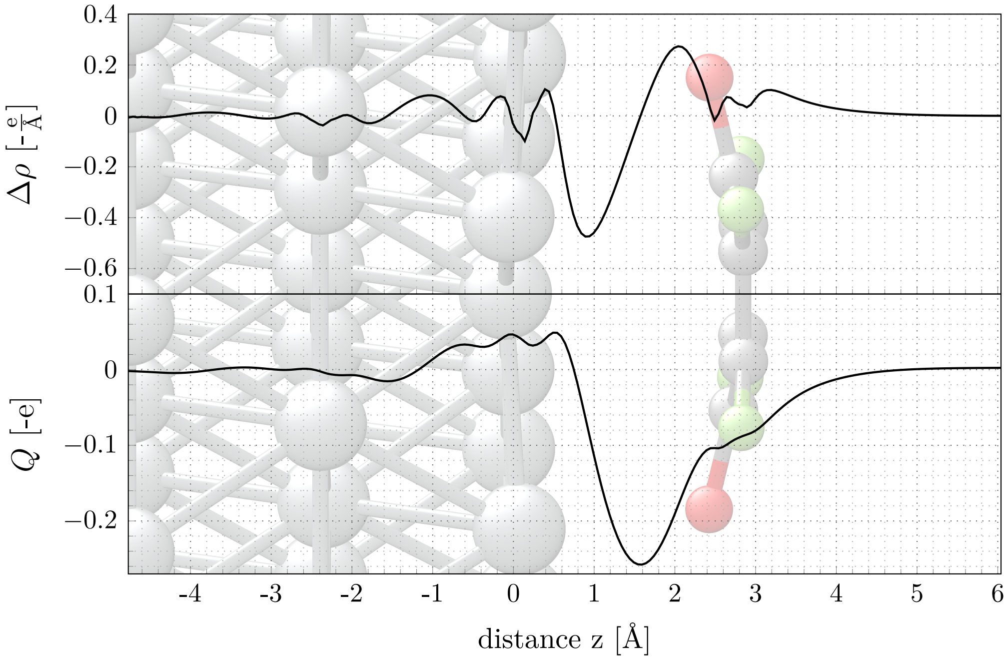

Figure 20: Charge redistribution $\Delta\rho$ and net charge transfer Q for a TFBQ monolayer adsorbed on a (a) Cu(111) and a (b) Ag(111) slab of six layers. The background images serve as guide to the eye.

(a) Charge rearrangements of TFBQ on Cu(111).

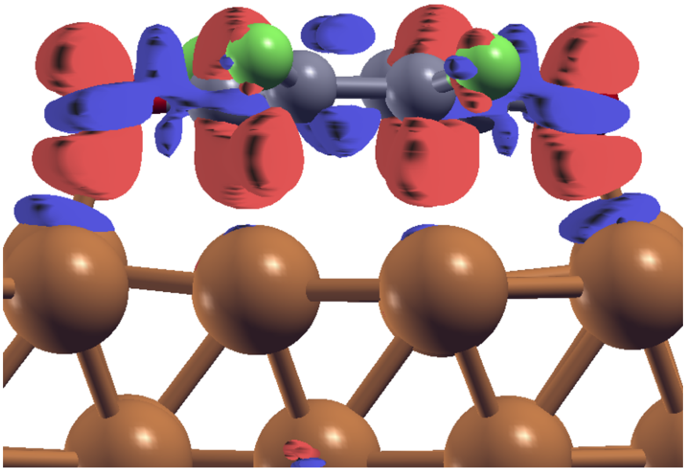

(b) Charge rearrangements of TFBQ on Ag(111).

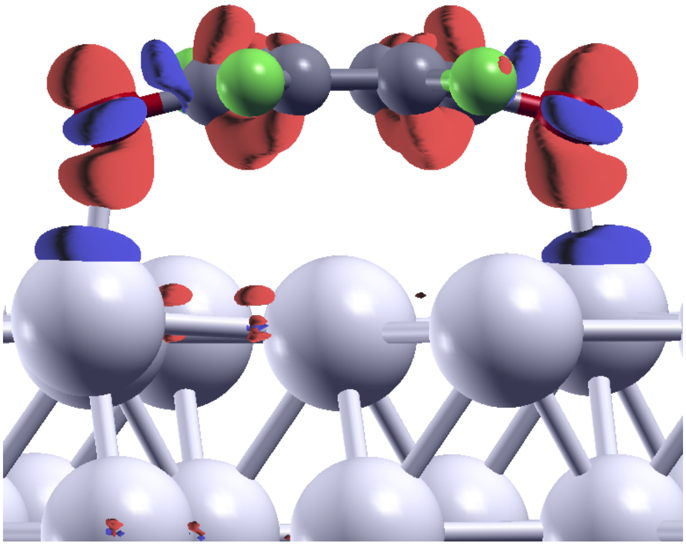

Figure 21: Iso-density plots of the charge rearrangements for adsorption of TFBQ on (a) Cu(111) and (b) Ag(111) with an iso-value of $\Delta\rho(\vec{r}) = 0.025\ \frac{\mathrm{e}}{\text{Å}^3}$. The red and blue surfaces indicate regions of electron accumulation and depletion.

(a) Charge rearrangements, $\Delta\rho(z)$, for TFBD on Cu(111).

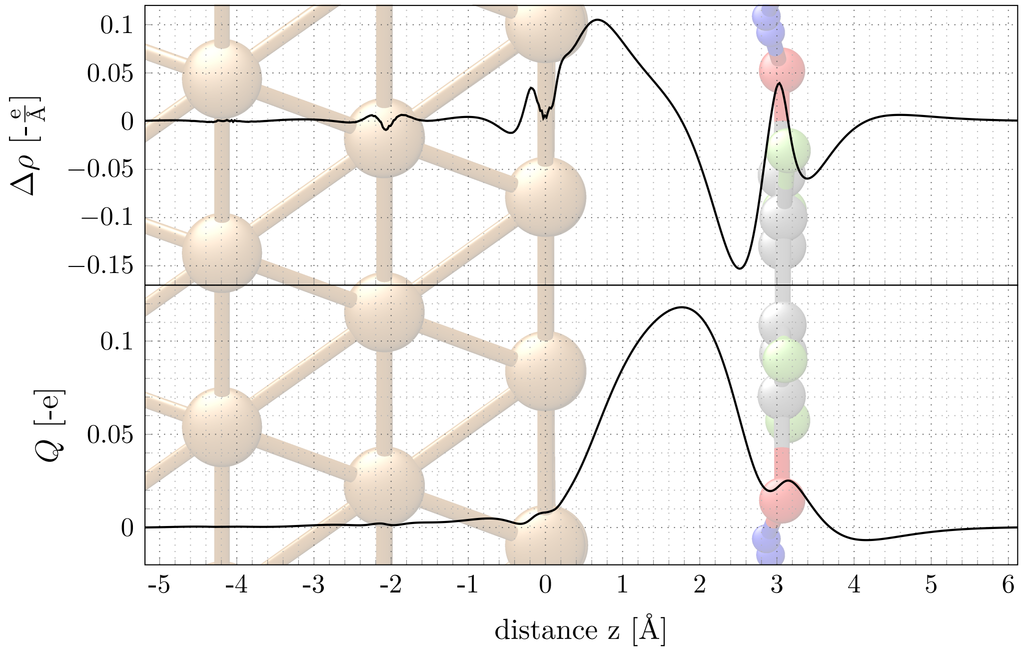

(b) Charge rearrangements, $\Delta\rho(z)$, for TFBD on Ag(111).

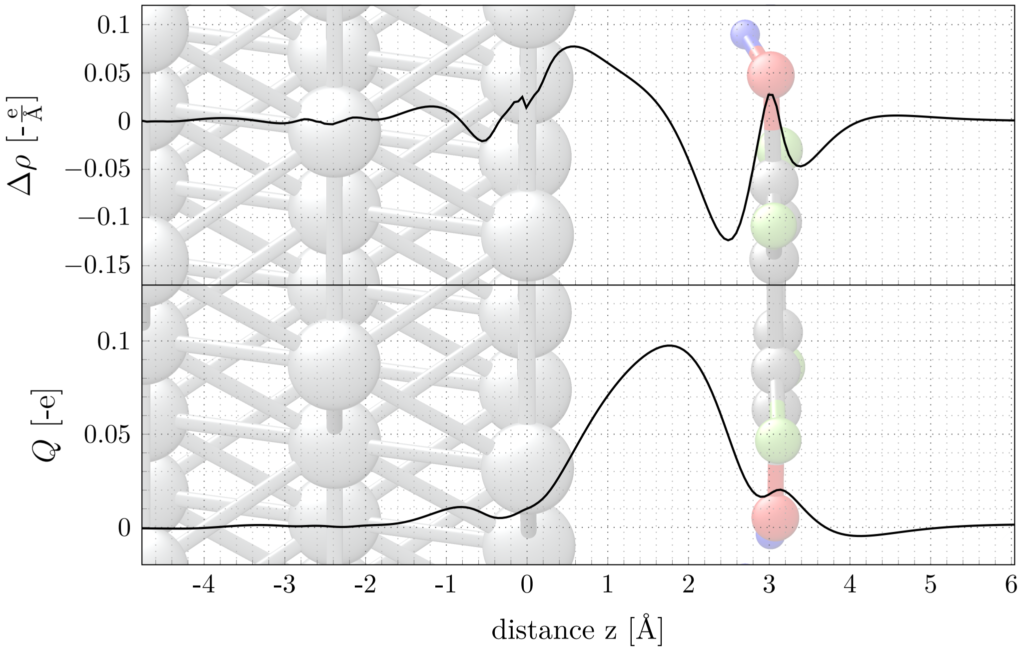

Figure 22: Charge redistribution $\Delta\rho$ and net charge transfer Q for a TFBD monolayer adsorbed on a (a) Cu(111) and a (b) Ag(111) slab of six layers. The background images serve as guide to the eye.

6 Mixed Monolayers

Here we come to the central part of this work: We investigate how gradual introduction of TFBD into a TFBQ-monolayer affects charge-injection barriers. Those barriers can be approximately determined by the energy difference of the Fermi energy, E_F, and the transport level of the overlying organic material – that is the HOMO for holes and the LUMO for electrons – compare section 2.2.1. Here first we focus on the work function modification $\Delta\Phi$, which determines the energy of E_F relative to the VL above the slab, and investigate how it is affected by the TFBD fraction, f, in mixed monolayers. To understand the energy level alignment at the interface we also look at sub-monolayers[29] of TFBQ and TFBD and discuss the courses of $\Delta\Phi(f)$ by considering electronic and structural properties like the density of states, the net molecular charges, the potential distributions, charge rearrangements and adsorption geometries. We then shift our focus on the second quantity affecting charge-injection barriers: The transport level of the overlying organic layers, which can be locally shifted by the electron potential above the surface. Therefore we investigate the distributions of the potential for different TFBD fractions, f, of mixed monolayers. Finally *ab initio* thermodynamics is employed – see introduction in section 2.3 – to describe the dependence of f on the pressure of a hydrogen gas phase surrounding the electrode. The results of this investigation show that the mixing ratio – and, thus, the charge-injection barrier – is tunable via hydrogen pressure control. Previous to this discussion, we introduce the supercell approach, which we used for the description of mixed monolayers.

6.1 Supercell Approach

Gradual induction of TFBD is simulated via supercells where the $(3 \times 3\sqrt{3})$ and $(\sqrt{7} \times \sqrt{7})R18.1^\circ$ unit cells for the single molecules in homogeneous monolayers adsorbed upon Cu(111) and Ag(111) are repeated along the directions of the lattice vectors. If this, for instance, is done twice along each lattice vector, one obtains a (2×2)-supercell with four adsorption sites on which, depending on the desired mixing ratio, the TFBQ and TFBD molecules of a mixed monolayer can be placed. Due to the single bond of the OH-group of the TFBD molecule to its phenyl ring it is freely rotatable around the bonding direction. By rearranging the TFBQ and TFBD molecules on the adsorption sites with gradually increasing TFBD fraction, f, and different alignments of the rotatable OH-groups, we find that for the ground state

---

[29] Here we define sub-monolayers as homogeneous monolayers with reduced coverage that is not achieved by modification of the unit cell size, but by successive introduction of empty adsorption sites into supercell geometries.

energy the alignment of the OH-bonds is crucial. To converge into the global energy minimum in the geometry optimization procedures, hence, it is necessary to rotate the OH-groups in such a way that the hydrogen comes close to an oxygen atom of a neighboring TFBQ molecule. This then leads to the formation of a hydrogen bond. It turned out that four geometries, as sketched in figure 23, serve as basic building blocks for the supercell geometries minimizing the ground state energy, if arranged in proper order.

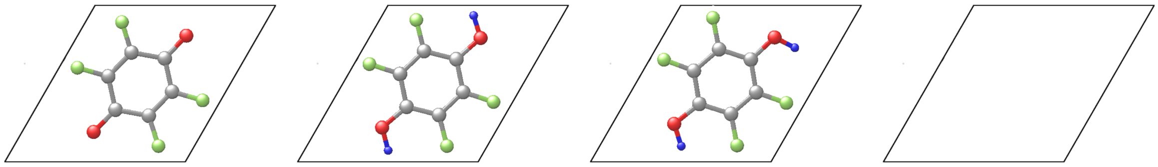
(a) Geometry 1. (b) Geometry 2. (c) Geometry 3. (d) Geometry 4.

Figure 23: Geometries that were arranged on the adsorption sites of supercells containing TFBQ and TFBD. (a) Geometry 1 for TFBQ; (b) Geometry 2 for TFBD with neighboring TFBQ molecules; (b) Geometry 3 for TFBD with neighboring TFBD molecules. (c) Geometry 4 for empty adsorption site.

To identify a certain supercell geometry based on its building blocks we introduced the following nomenclature. Starting from the lower, left adsorption site of a supercell the respective sub-geometries shown in figure 23 are labelled by the numbers 1, 2, 3 and 4. A new row is indicated by a slash symbol "/". The supercell geometry shown in figure 24 then for instance would be labelled as "21/12". By proper alignment of those building blocks a set of supercell geometries were created that served

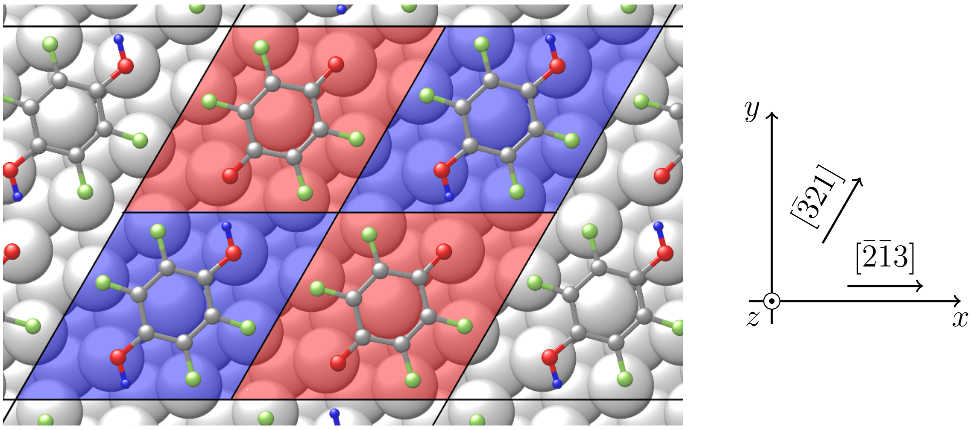

Figure 24: Top view on an exemplary supercell geometry "21/12" on Ag(111) with f = 50 % and checkerboard motif. The adsorptions sites of the TFBQ and TFBD molecules in the supercell geometry are colored red and blue.

as starting points for geometry optimizations. A list of the supercell geometries that were investigated within this work is shown in table 8.

Depending on the neighboring molecules above and below a unit cell for TFBD in the adsorption site two alignments of the OH-bonds minimize the ground state energy: Geometry 2 is preferable when hydrogen bonds are formed to neighboring TFBQ molecules – the OH-group is rotated such that the hydrogen approaches the oxygen atom of the neighboring TFBQ molecule as closely as possible. For neighboring TFBD molecules geometry 3 minimizes the ground state energy – for instance is $E^{\mathrm{Cu(111)}}_{33/33} - E^{\mathrm{Cu(111)}}_{22/22} = -0.63$ eV.

In mixed layers of electron donating and accepting molecules or SAMs cases of superstructure formation and phase separation were reported – see Otero et al. [84] or Stranick et al. [85]. To check whether phase separation is likely to occur for the investigated system, a set of supercell geometries with different arrangements of TFBQ and TFBD molecules at 50 % TFBD fraction were evaluated. We found that checkerboard motifs, as indicated in figure 24, are always more stable than structures where molecules are arranged in rows or clusters. However, the difference in the total energies are just a few meV – for instance $E^{\mathrm{Cu(111)}}_{12/21} - E^{\mathrm{Cu(111)}}_{12/12} = -4.5$ meV and $E^{\mathrm{Cu(111)}}_{12/21} - E^{\mathrm{Cu(111)}}_{11/22} = -1.5$ meV. For a mixed monolayer of TFBQ and TFBD phase separation is, therefore, not expected. Because checkerboard arrangements of the TFBQ and TFBD molecules cannot be realized for odd numbers of unit cell repetitions we focussed on even repeat unit numbers: in particular on 2×2 and 4×2 supercell geometries.

To reduce the number of involved atoms and, thus, computation effort in contrast to chapter 5, due to the large number of atoms in the supercell geometries of mixed monolayers, here just four layers were chosen to simulate the coinage metal slab. Based on the layer convergence tests for Cu(111) – see chapter 3.3 – the reduction of the number of layers from 6 to 4 causes an increased work function inaccuracy of $\delta\Phi \approx 0.02$ eV. For Ag(111) the inaccuracy changes to $\delta\Phi \approx 0.09$ eV. The computational settings that were employed for the final calculations are shown in table 9. The first five settings in this table are suggested to be used in FHI-*aims*, when systems are investigated that contain hundreds of atoms – compare Blum et al. [38].

For each supercell geometry optimizations were performed by the following procedure: First with "light" basis function sets a preliminary optimization was done, before with a "tight" basis function configuration again a geometry optimization was carried out to a force of 0.03 $\frac{\mathrm{eV}}{\mathrm{Å}}$.

Table 8: Supercell geometries for the simulation of mixed monolayers and submonolayers.

Adsorbate	Arrangement			
TFBQ coverage	11/41	14/41	14/44	
	1111/4111	1111/4141	1411/4141	1414/4141
	4414/4141	4444/4141	4444/4441	
TFBD coverage	44/24	42/24	43/23	
	4444/2444	4444/2424	4244/2424	4242/2424
	3242/3424	3232/3434	3332/3334	
mixed	11/21	12/21	13/23	
	1111/2111	1111/2121	1211/2121	1212/2121
	3212/3121	3232/3131	3332/3331	
borderline cases	1	3	4	

Table 9: Settings for the final calculations with supercells.

Setting	Value
density_update_method	density_matrix
collect_eigenvectors	.false.
empty_states	3
use_local_index	.true.
load_balancing	.true.
sc_accuracy_rho / _eev / _etot / _forces	1E-5 / 1E-3 / 1E-4 / - (for 2×2 superc.)
	1E-5 / - / 1E-5 / 1E-3 (for 4×2 superc.)
k_grid	6 6 1
k_offset	0.416667 0.416667 0
Cu basis functions	tight: minimal + tier1
H, C, O and F basis functions	tight: minimal + tier1 + tier2

6.2 Modification of the Electron Spill Out

It was argued by Stadtmueller et al. [86] that in mixed monolayers of electron-accepting and -donating molecules (without hydrogen bonds) the modification of the electron-spill-out plays an important role for the equalization of the adsorption height. To investigate the extent of this effect for the TFBQ / TFBD system, sub-monolayers of TFBQ and TFBD with 75 % coverage on Cu(111) were investigated. By comparison of the plane integrated charge density $\rho(z)$ on the empty adsorption site to the corresponding value without any adsorbate on the Cu(111) surface, the modification of the electron-spill-out on neighboring sites due to adsorption of TFBQ and TFBD was investigated.

The results of this investigation are shown in figure 25: In the left part the charge density integrated over the area of the empty adsorption site, $\rho(z)$, is plotted for sub-monolayers of TFBQ (dashed, red line) and TFBD (dotted, blue line). For comparison further the corresponding $\rho(z)$ values are plotted for a clean Cu(111) surface (solid, black line). The inlay graphic shows the top view on an empty adsorption site of a TFBQ-submonolayer with the spatial region used for the plane integration indicated by the green area. The plot qualitatively shows that the adsorption of TFBQ decreases the charge density in its vicinity on the surface, whereas TFBD causes an increase. To quantify the extent of this effect in the right part of figure 25 for given values of ρ the spatial shift of that iso-value $\Delta z(\rho)$ is plotted. $\Delta z(\rho)$ was calculated the following way: First for the sub-monolayers of TFBQ and TFBD and the clean Cu(111) surface the $\rho(z)$ data values were fitted by an exponential decay:

$$\rho(z) = \rho_0 + A \cdot \exp\Big(-\frac{z}{\zeta}\Big) \tag{6.1}$$

By inversion of that function to

$$z(\rho) = \zeta \cdot \ln\Big(\frac{A}{\rho - \rho_0}\Big) \tag{6.2}$$

then the spatial shift of the charge-density iso-value, ρ, was calculated via:

$$\Delta z(\rho)_{\text{TFBQ/TFBD}} = z(\rho)_{\text{TFBQ/TFBD}} - z(\rho)_{\text{no adsorbate}} \tag{6.3}$$

By reading the $\Delta z(\rho)$ value for charge densities at the mean heights of the adsorbed molecules – indicated via the horizontal lines – the modification of the electron-spill-out at the empty adsorption site can be estimated. For the TFBQ adsorbate we find that at 75 % TFBQ coverage the electron-cloud spilling out into vacuum on the empty adsorption site moves down by about -0.04 Å for $\rho = -0.05\ \frac{\text{e}}{\text{Å}}$, because electron density is transferred to the electron-accepting molecule. TFBD on the other hand pushes charge density into the empty site so that the electron-spill-out there moves up by about 0.08 Å.

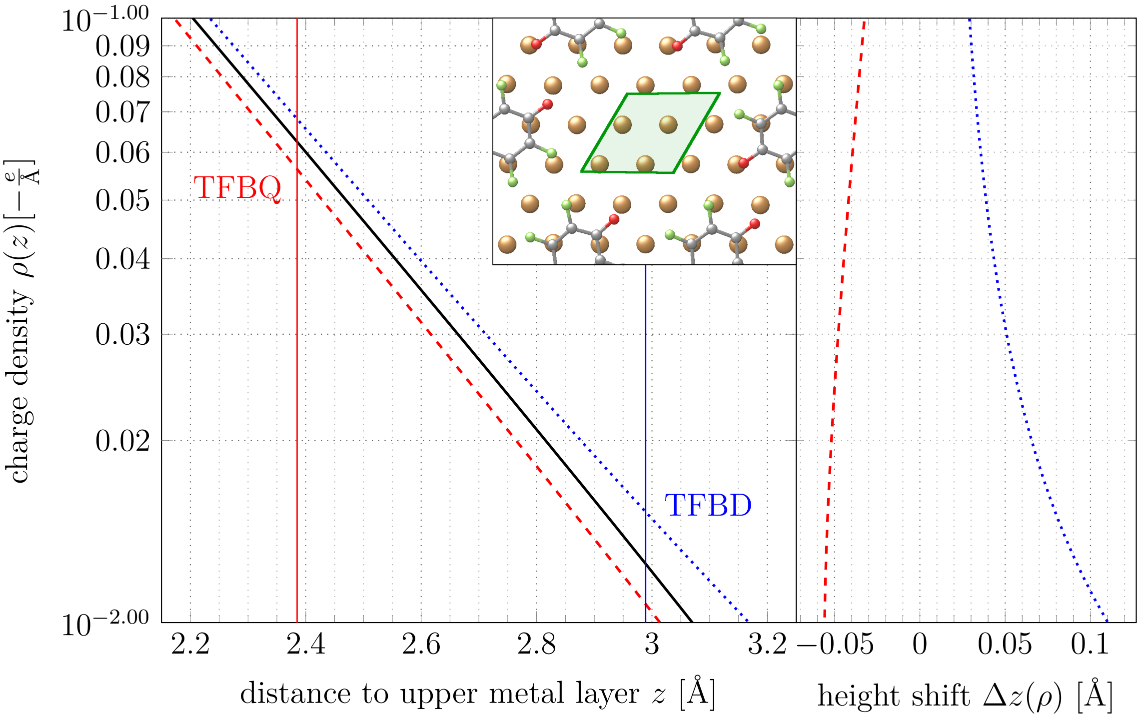

Figure 25: *(left)* Plane integrated charge densities $\rho(z)$ on the empty adsorption site of a 2×2 Cu(111)-supercell with 75 % coverage of TFBQ (dashed red line) and 75 % coverage TFBD (dotted blue line). For comparison also $\rho(z)$ of the Cu(111) surface without any adsorbate is shown (black line). The horizontal lines indicate the mean positions of the molecules in the sub-monolayers of TFBQ (red) and TFBD (blue) – i.e., homogeneous monolayers of lower coverage. The region that was considered for the plane integration is sketched by the green area in the inlay graphic that shows an empty adsorption site in a TFBQ sub-monolayer.
(right) Spatial shift of the electron-spill-out upon the metal surface $\Delta z(\rho)$ at the empty site due to adsorption of TFBQ (dashed red line) and TFBD (dotted blue line) on neighboring sites. The two lines were calculated via equation 6.3.

6.3 Density of States of a Hypothetical, Free-Standing, Mixed Monolayer

Generally compounds of quinones and diols form solid charge-transfer complexes. One example is chinhydron, an equimolar mixture of 1,4-benzoquinone (BQ) and 1,4-benzenediol (BD). There the extent of the charge transfer of an electron-donating diol to an electron-accepting quinone is usually just a small fraction (≈ 0.05) of an electron – compare Streitwieser et al. [23, chapter 30.8.4]. The electrostatic attraction between the charges present on the molecules leads to formation of a solid phase.

To check whether mixed monolayers of TFBQ and TFBD also form such complexes here we study the hypothetical, free-standing monolayer of a selected case. In particular we consider 2×2 supercells simulating mixed monolayers with $f = 25$ % and $f = 75$ %. The projections of the DOS on the molecules in that supercell geometries are shown in figures 26a and 26b. From the corresponding species-projected DOS we find that the HOMO of the TFBD molecules overlaps with the TFBQ-LUMO indicating strong diol to quinone electron transfer. Further it is apparent that the overlap of the orbitals and, thus, the charge transfer is increased, when a hydrogen bond (HB) is present between neighboring TFBQ and TFBD molecules.

When we think of the adsorption of such a free standing monolayer on a surface, besides the charge transfer within the monolayer and the electrostatic attraction of the quinone and diol molecules, due to the interaction with the surface now further effects come into play: Fermi level pinning of the TFBQ-LUMO and Pauli pushback. Due to the presence of the metal acting as electron reservoir the situation observed for the free-standing monolayer will change – see chapter 6.4.

(a) $f = 25$ %

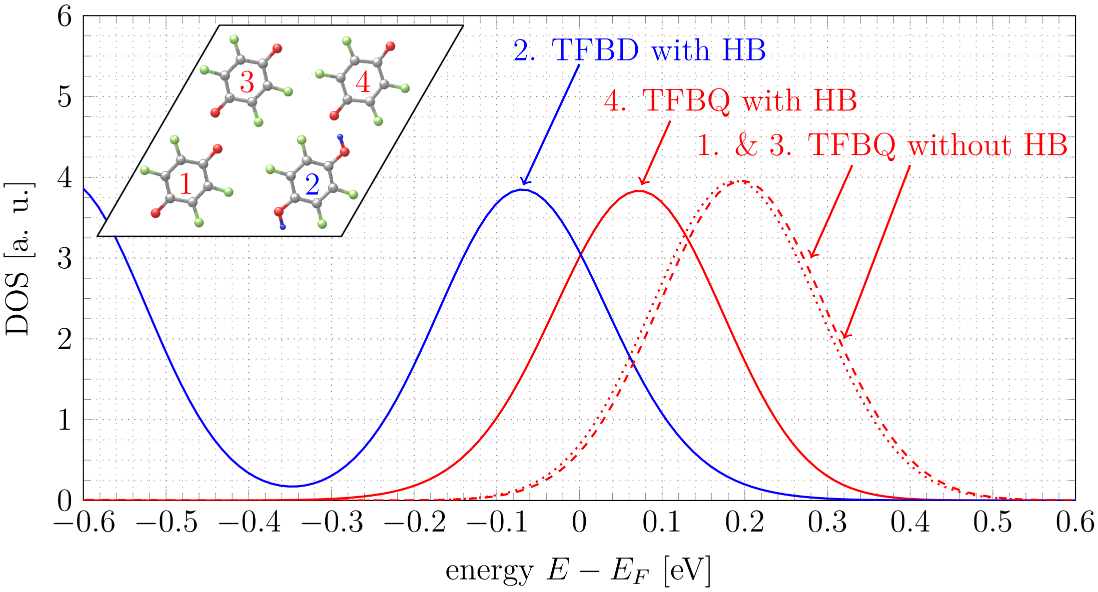

(b) $f = 75$ %

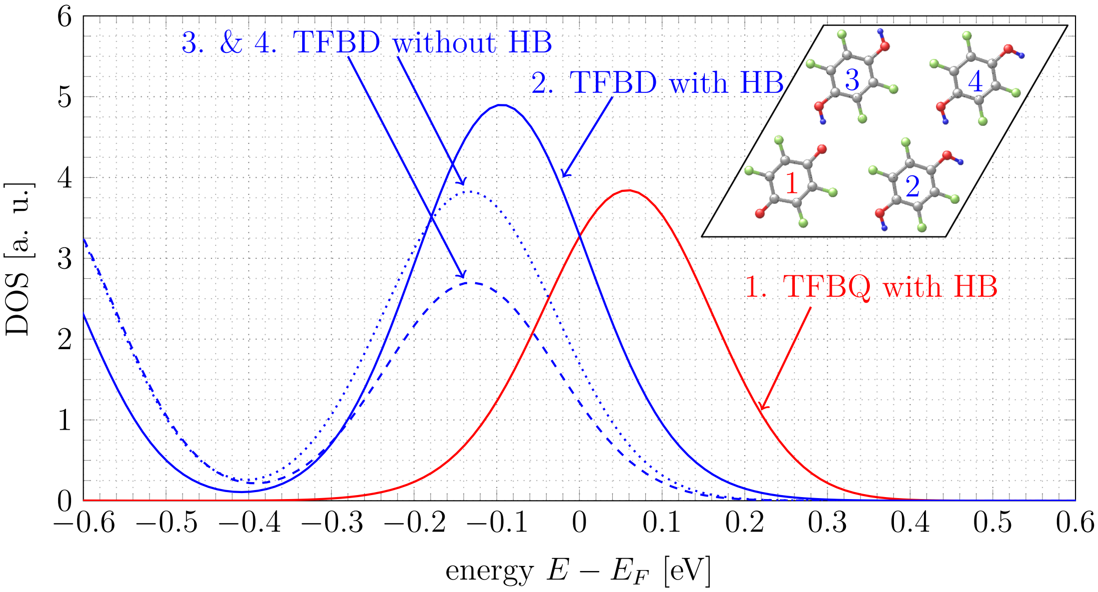

Figure 26: Projection of the DOS on the molecules of a free standing mixed monolayer with (a) $f = 25$ % and (b) $f = 75$ %. The 2×2 supercell geometries with the labelled molecules are sketched in the inlay graphics. The TFBQ-LUMO overlaps with the HOMOs of the TFBD molecules. Therefore charge is transferred from TFBD to TFBQ. An increase of the TFBQ-LUMO to TFBD-HOMO overlap is observed for certain molecules, where a hydrogen bond (HB) is present.

6.4 Density of States of the Full System

Here we analyze the density of states for mixed monolayers adsorbed upon Cu(111) and Ag(111). By projecting the density of states on the molecular species of the mixed monolayer – TFBQ and TFBD – those changes can be analyzed seperately. For different fractions of chemical defects those projections are shown in figure 27. We find that with gradually increasing number of TFBD molecules, f, changes in the density of states occur.

For mixed monolayers adsorbed on Cu(111) from the projection on TFBQ we find that the LUMO shifts by ≈ -0.29 eV with an increase of the defect fraction, f, from 0 % to 75 %. Due to this shift in the DOS an increased occupation of the LUMO and hence a net charging of the TFBQ molecules has to be expected. In the DOS projection of the TFBD molecule the HOMO shifts by $\approx +0.33$ eV to higher energies, with an increase of the TFBQ fraction, $1 - f$, from 0 % to 75 %. Despite the shift the TFBD-HOMO-peak is still ≈ 0.7 eV below from E_F. As a consequence, the TFBD-HOMO remains fully occupied upon adsorption of the mixed monolayer . For the TFBD molecules on the other hand no charge transfer due to changes in the electronic structure can be deduced. For mixed monolayers adsorbed on the metal no overlap of the TFBQ-LUMO with the TFBD-HOMO at E_F is observed. The charge-transfer between TFBQ and TFBD that was observed for the free-standing mixed monolayer – compare section 6.3 – apparently disappears upon adsorption on a coinage metal surface. For the adsorbed mixed monolayer the interaction with the metal dominates the electronic structure.

The energy shifts of the molecular orbitals basically occur according to the potential distribution caused by the neighboring molecules.[30] A closer look reveals that the potential distribution and, thus, the particular peak positions actually result from the interplay of multiple effects: The adsorption-induced, (net) positive charges at the TFBD sites due to the Pauli pushback effect with the corresponding counter charges in the meteal cause an electric field at the TFBQ site shifting the TFBQ-LUMO-peak down in energy with increasing TFBD fraction. On the other hand the negative charges of the TFBQ molecules formed by Fermi-level-pinning lead to an electric field at the TFBD site shifting the TFBD-HOMO-peak up in energy with increasing TFBQ fraction.[31] Further the aforementioned modification of the electron-spill out plays a non-negligible role – compare section 6.2.

---

[30] Contrary, for sub-monolayers of TFBQ and TFBD the peaks of the molecular orbitals in the DOS hardly shift – compare figure 33 in section 6.7.2 – what corroborates the hypothesis.

[31] A detailed discussion of the effects of this subtle interplay of TFBQ and TFBD will be done in sections 6.7.2, 6.7.3 and 6.7.4.

(a) Cu(111)

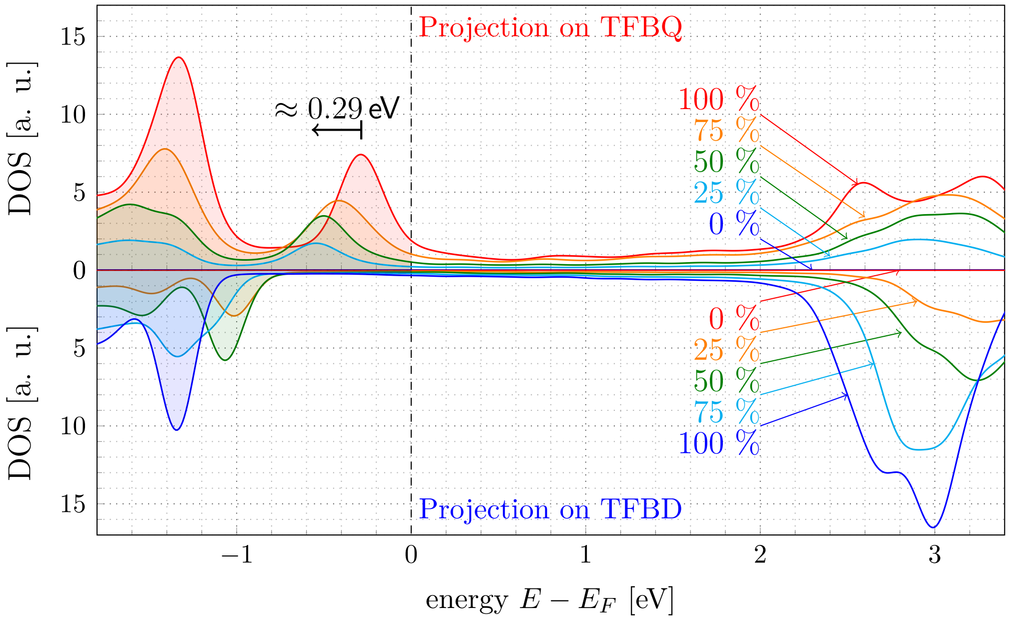

(b) Ag(111)

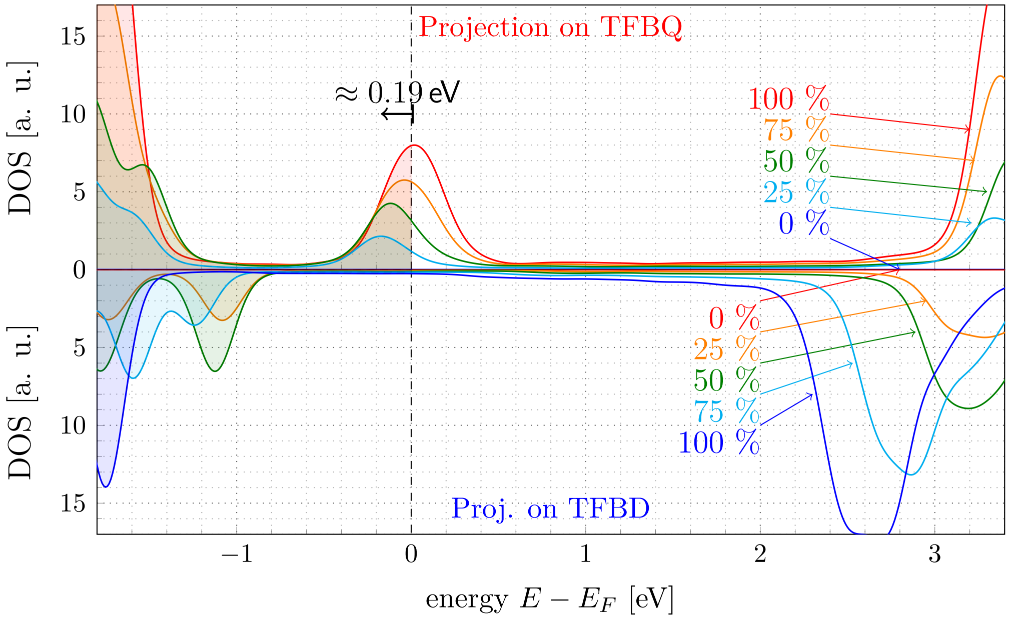

Figure 27: Projection of the density of states on TFBQ (upper plot) and TFBD (lower plot) in mixed monolayers adsorbed upon (a) Cu(111) and (b) Ag(111) with gradually increased number of chemical defects. The defect fraction, f, corresponding to each line is annotated via arrows. The shift of the LUMO-peak to lower energies causes a charging of the TFBQ molecules in mixed monolayers with increased TFBD fraction (see bold, horizontal arrow).

6.5 Adsorption Heights and Molecular Charges

The work function modification, $\Delta\Phi$, is determined by the formation of molecular and bond dipoles that are affected by the distortion of the molecule and adsorption-induced charge rearrangements – compare section 2.2.2. Before showing the results of $\Delta\Phi$, here, we investigate the courses of the adsorption heights and the molecular charges of the TFBQ and TFBD molecules in mixed monolayers with increasing TFBD fraction, f. In particular we study the distance of the mean z-positions of the molecule's atoms to the mean height of the uppermost coinage metal layers for Cu(111) and Ag(111). Moreover, we investigate the charges of the adsorbed molecules via the Mulliken scheme – see chapter 2.1.5. This suggests itself, because the charge rearrangements discussed in chapter 5.5 were in congruency with the calculated Mulliken charges. Further we compare the adsorption heights and the Mulliken charges in mixed monolayers to corresponding sub-monolayer cases. Moreover, we take a closer on the adsorption heights and molecular charges at specific sites of selected mixed monolayer cases.

For Cu(111) and Ag(111) the mean adsorption heights of the atomic species and the TFBQ and TFBD molecules are shown in figure 28a and 28b.

Comparing the adsorption heights for TFBD in mixed monolayers (blue filled diamonds) to the corresponding sub-monolayers (blue open diamonds) for both coinage metals strong deviations are apparent: For the sub-monolayer cases the adsorption height of the TFBD molecules reduces by a very small extent (≈ 0.05 Å) with decreasing coverage due to the modification of the electron spill out in neighboring adsorption sites – for more details see section 6.2. In mixed monolayers the corresponding reduction of the adsorption height of TFBD is increased due to the presence of the TFBQ molecules – here the downshift of the atoms is about 0.2 Å. Naively one might expect that this occurs due to the electrostatic attraction with TFBQ that is present on the neighboring adsorption sites in the hypothetically, free-standing monolayer – compare section 6.3. However, a charging of the TFBQ and TFBD molecules due to their interaction is not reflected in the DOS of mixed monolayer adsorbed on coinage metal surfaces – compare section 6.4. Upon adsorption the molecular species of the mixed monolayer interact mainly with the metal serving as electron "reservoir", rather than with each other.

For the TFBQ molecules in mixed monolayers we find that on Cu(111) the oxygen atoms move towards TFBD by about 0.15 Å with increasing TFBD fraction f from 0 to 100 %. On Ag(111) we observe the same trend, whereas the increase of the oxygen atoms distance to the uppermost metal layer here is much smaller – about about 0.06 Å. On the other hand, the position of the oxygen atoms stays nearly constant

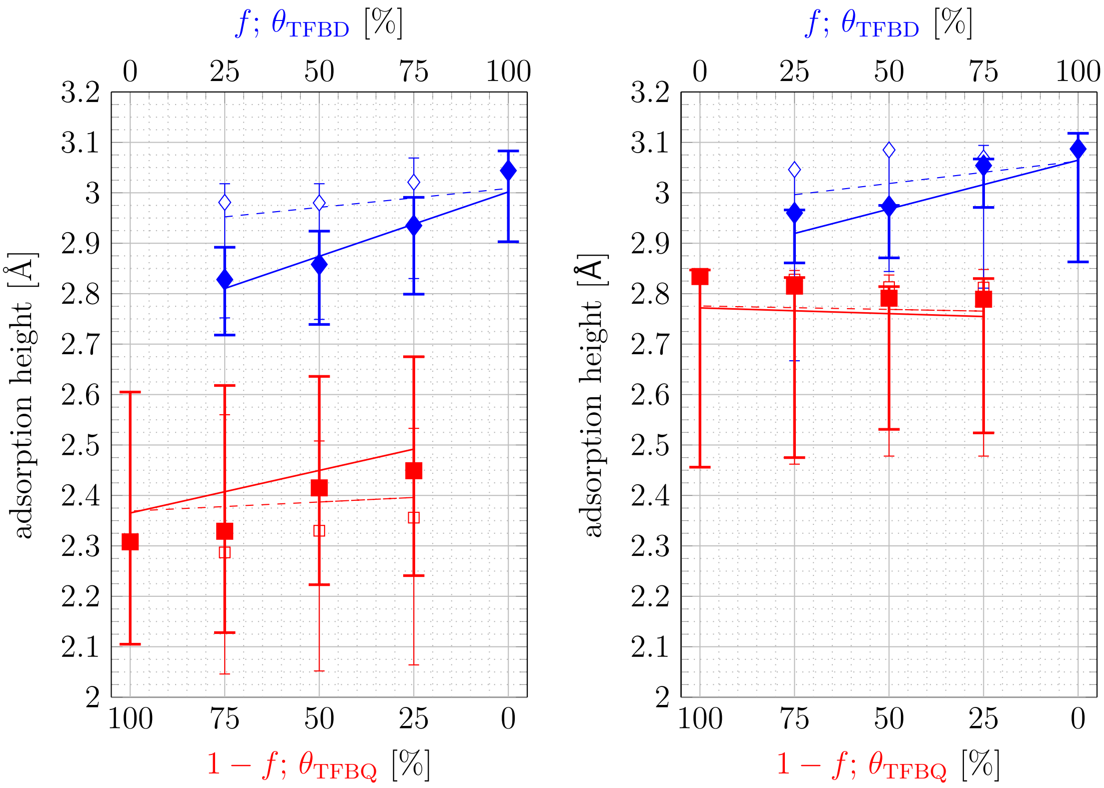

(a) Cu(111).

(b) Ag(111).

Figure 28: Adsorption heights of the atomic species of TFBQ (red squares) and TFBD (blue diamonds) in mixed monolayers on (a) Cu(111) and (b) Ag(111). The data points indicate the mean distance of the carbon backbone to the mean position of the upper metal layer. The upper error bar indicates the mean position of the fluorine atoms. The lower error bar describes the mean position of the oxygen atoms for TFBQ and of the hydrogen atoms for TFBD. The plotted lines indicate linear fits to the mean position of the TFBQ and TFBD molecules. For comparison further the results of the corresponding sub-monolayers are drawn – see smaller, open symbols, with narrower ”error” bars and dashed regression lines.

for the corresponding sub-monolayer cases. For mixed monolayers on Cu(111) and Ag(111) the position of the carbon backbone evolves differently with f. Like the oxygen atoms, on Cu(111) the mean position of the carbon atoms increases by about 0.15 Å. Contrary, on Ag(111) the carbon backbone shifts down by about 0.05 Å. Those trends of the carbon backbones position are also observed for the corresponding sub-monolayer cases, whereas the extent of the shift there is much smaller.[32] The aforementioned difference in the adsorption height dependence is further reflected in the linear regressions of the mean adsorption heights: Comparing to the corresponding sub-monolayer cases for mixed monolayers the slope of the linear fit is increased on Cu(111). On Ag(111) it stays nearly constant.

Such an "equalization of the adsorption heights" was also observed experimentally for different mixed-monolayers of electron-accepting and -donating species by Stadtmüeller et al. [86]. A central effect mentioned there is the modification of the electron spill out due to the adsorption of the molecules that affects neighboring adsorption sites. However, for system investigated here, this is a minor effect – compare section 6.2. Here it only explains the changes of the adsorption heights in sub-monolayers.

The absolute values of the Mulliken charges upon adsorption on Cu(111) and Ag(111) strongly increase for both TFBQ and TFBD upon intermixing – see figures 29a and 29b. The higher the number of neighboring TFBQ (TFBD), the higher is the positive (negative) charging of TFBD (TFBQ). Changing the TFBQ-fraction, $1-f$, from 0 to 75 % the Mulliken charge of the TFBD-molecules doubles – see blue filled diamonds. For the molecular charges of the TFBQ molecules even a triplication is observed with increasing TFBD-fraction, f, from 0 to 75 %.

The change of the adsorption height hardly affects the molecular charges calculated via the Mulliken scheme: By manually changing the adsorption height of homogeneous TFBD monolayers on Cu(111) by 0.2 Å the molecular charge for instance only increases by 0.06 e, as our DFT calculations show.

Investigating the specific adsorption sites in mixed monolayers we find that the adsorption distances and Mulliken charges deviate strongly for TFBQ and TFBD molecules, depending on whether a hydrogen bond is present or not. In table 10 the adsorption distances and Mulliken charges for different adsorption sites with or without hydrogen bonds are quoted exemplary for two selected mixed monolayers on Cu(111). We find that the presence of hydrogen bonds for the investigated system plays an important role.

---

[32] Due to the results of section 6.2 we assume that for sub-monolayers mainly the modification of the electron-spill out above the metal surface is relevant for the course of the carbon backbones position.

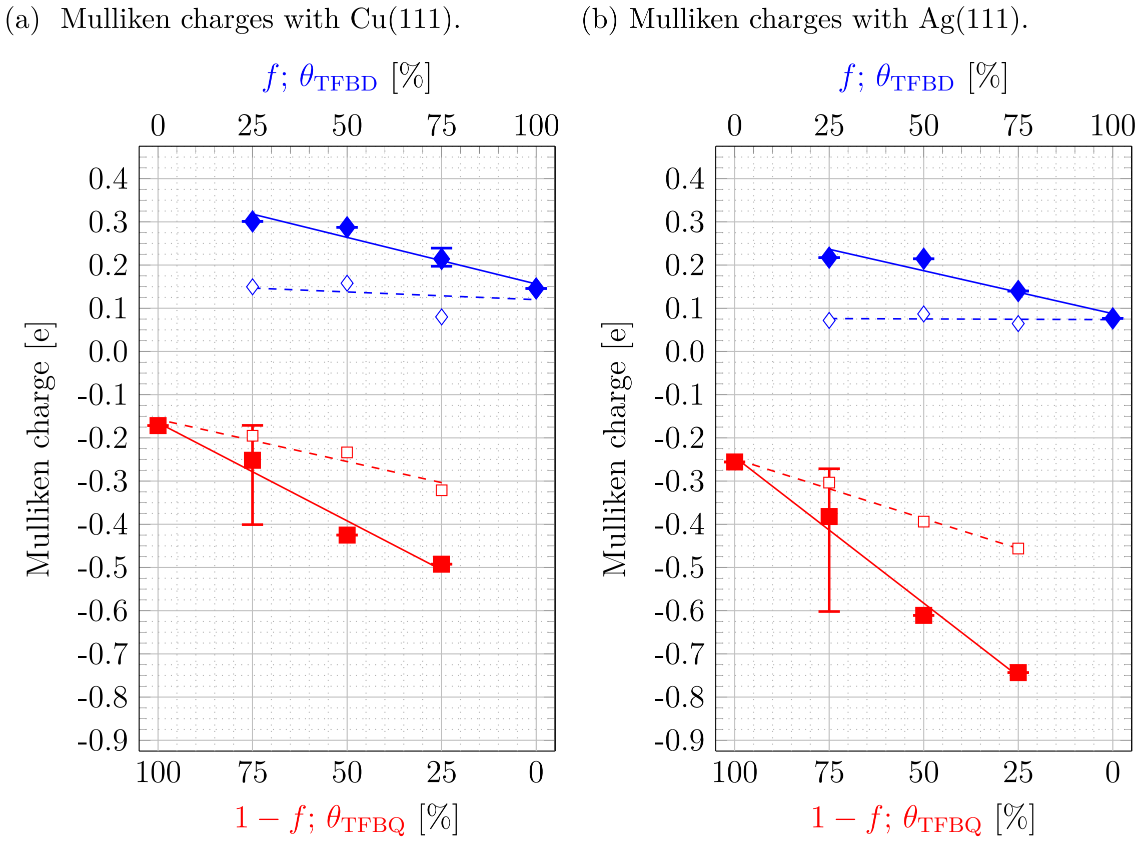

Figure 29: Mean values of the molecular charges of TFBQ (red squares) and TFBD (blue diamonds) in mixed monolayers on (a) Cu(111) and (b) Ag(111) calculated via the Mulliken partitioning scheme. The maximum and minimum values in mixed monolayers are shown via error-bars. To highlight the courses of the respective data sets moreover linear fits are plotted as lines. For comparison further the mean values of sub-monolayers at corresponding coverage are shown – see smaller open symbols.

Table 10: Comparison of adsorption heights, d_{ads}, and Mulliken charges, q, in mixed monolayers adsorbed on Cu(111) with $f \in 25\ \%,\ 75\ \%$ at different adsorption sites with and without hydrogen bond.

Q / D .... adsorption site with TFBQ / TFBD and no hydrogen bond
Q_{HB} / D_{HB} .... adsorption site with TFBQ / TFBD and hydrogen bond

Cu(111)	$f = 25\ \%$		$f = 75\ \%$	
Ads. site	d_{ads} [Å]	q [e]	d_{ads} [Å]	q [e]
Q	2.37	–0.18		
Q_{HB}	2.44	–0.40	2.49	–0.49
D_{HB}	2.83	+0.30	2.89	+0.24
D			2.95	+0.20

Initially we expected charge transfer between the electron-accepting and -donating species of the mixed monolayer as seen in charge-transfer complexes such as chinhydron (compare Streitwieser et al. [23, chapter 30.8.4]). This would have explained the respective increase in molecular charge of the TFBQ and TFBD molecules in the mixed monolayer. It would have further explained the equalization of the adsorption heights as a consequence of electrostatic attraction. If this was true, it would also have been reflected by an overlap of the TFBQ-LUMO and TFBD-HOMO peaks at E_F in the DOS. For the hypothetically, free-standing monolayer this indeed is observed – for details see section 6.3. However, upon adsorption of the layer on a metal surface the overlap of the TFBQ-LUMO- and TFBD-HOMO-peak at E_F disappears – compare section 6.4, due to the aforementioned interaction with the metal.

6.6 Charge Rearrangements within Adsorption Sites

For a selected case of mixed monolayers here we investigate how the adsorption-induced charge-rearrangements change compared to homogeneous monolayers – see section 5.5.

The charge rearrangements upon adsorption, $\Delta\rho(\vec{r})$, within the 2×2 supercell are partitioned into quarters corresponding to the adsorption sites of the molecules. This partitioning, of course, is somehow arbitrary, but provides an acceptable, qualitative picture of the charge rearrangements at the different adsorption sites of the mixed monolayer. The corresponding charge redistributions $\Delta\rho(z)$ and net charge transfers, $Q(z)$, on the different adsorption sites of a supercell with $f = 75\ \%$ are shown in figure 30.

(a) Charge rearrangements at TFBQ site. The horizontal dashed, red line indicates the mean position of the oxygen atoms of TFBQ in the mixed monolayer.

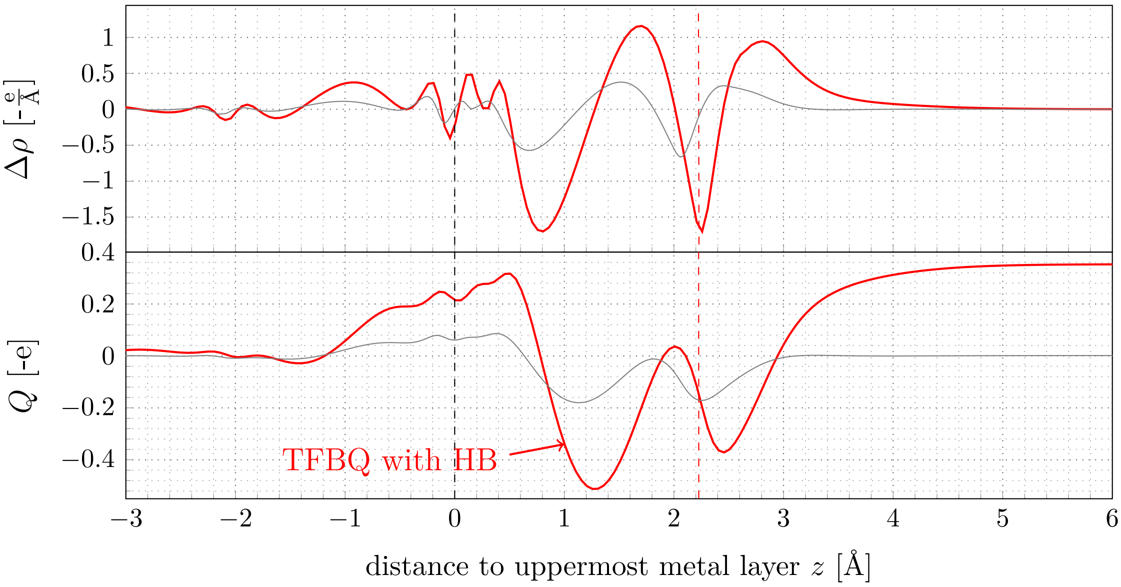

(b) Charge rearrangements at TFBD sites. The horizontal dashed, blue line indicates the mean position of the carbon atoms of TFBD in the mixed monolayer.

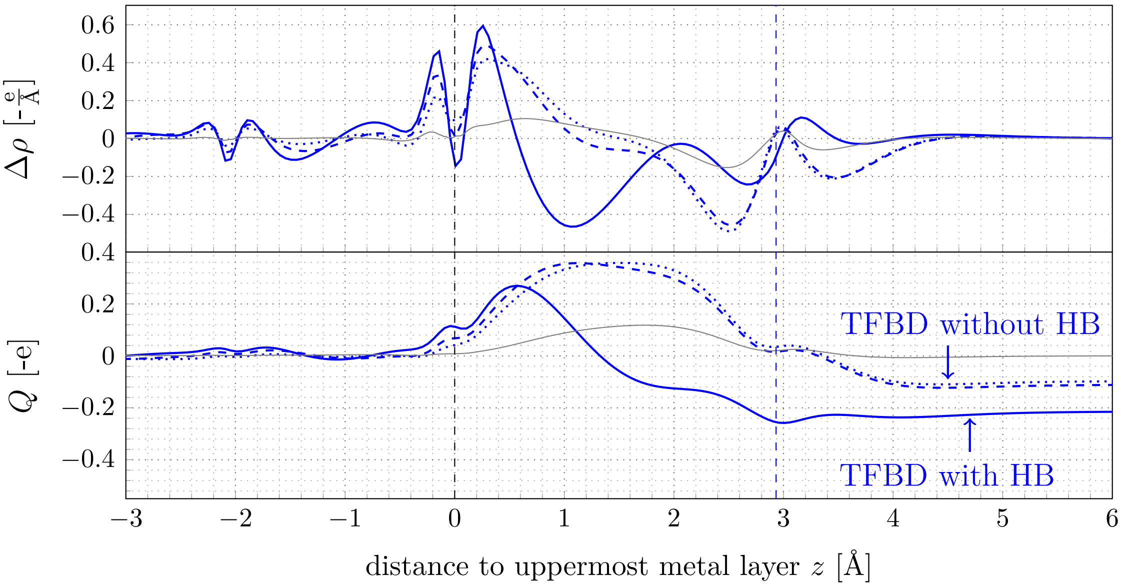

Figure 30: Plane averaged charge redistribution $\Delta\rho$ and net charge transfer Q at the different adsorption sites of a supercell with $f = 75$ % and a Cu(111) slab of four layers. The horizontal black, dashed line indicate the mean positions of the uppermost Cu layer. Two plots are shown that contain the charge rearrangements at the (a) TFBQ and (b) TFBD sites. For comparison also the results of homogeneous layers are drawn as thin, grey lines.

The $\Delta\rho(z)$ dependence of the TFBQ molecule forming a hydrogen bond to neighboring TFBD looks very similar to that of the homogeneous monolayer: Due to the chemical interaction, two "positive peaks" of charge accumulation arise in the π-system of the TFBQ molecule at $z \approx 1.8$ Å and $z \approx 2.8$ Å. As a consequence of the increased adsorption height of the molecule the peaks are located ≈ 0.2 Å higher than the peaks of homogeneous monolayer. The net charge transfer, $Q(z)$, describes how much charge was shifted from above a plane at a certain height z below that plane. Thus, the $Q(z)$-peak between the uppermost metal layer and the molecule delivers the information how much charge was shifted from the molecule to the surface. Contrary the corresponding $-Q(z) = \bar{Q}(z)$ value of that peak describes the adsorption-induced charging at the molecular site. The amplitude of the peak of $\bar{Q}_{\text{max}} \approx -0.48$ e shows very good agreement with the molecular charge calculated with the Mulliken scheme of $q = -0.49$ e. Also charge rearrangements at the sites of the TFBD molecules without hydrogen bonds qualitatively are very similar to that of the homogeneous monolayer: Due to the Pauli pushback effect charge is accumulated directly above the surface – see positive $\Delta\rho$ peak at $z \approx 0.3$ Å. However, by comparison to homogeneous layer, this region of accumulation is narrower and shifted to the surface. Further at the position of TFBD due to the presence of the molecule a depletion region occurs – see the two negative peaks arise in the π-system of the TFBD-molecule at $z \approx 2.8$ Å and $z \approx 3.5$ Å.

For the TFBD molecule with hydrogen bonds to TFBQ, on the other hand, between the regions of accumulation above the surface and the region of depletion at the π-system of the molecule additionally at $z \approx 1.1$ Å a peak of electron depletion arises. From the maximum of $Q(z)$ between the uppermost metal layer and the molecule the charge transfer to TFBD with hydrogen bond can be estimated as $\bar{Q}_{\text{max}} \approx 0.28$ e. This shows good agreement with the corresponding Mulliken charge of $q = 0.24$ e. Estimating the charge transfer to TFBD without hydrogen bond we find $Q_{\text{max}} \approx 0.34$ e. Comparing this to the corresponding Mulliken charge of $q = 0.20$ e we find a larger deviation of 0.14 e.

6.7 Work Function Modification[33]

Here we investigate how the work function modification, $\Delta\Phi$, depends on the TFBD fraction, f, and how this compares to the more traditional approach of changing the coverage, θ, of a single compound. For mixed monolayers of TFBQ and TFBD on Cu(111) and Ag(111) the courses of $\Delta\Phi(f)$ are shown in figure 31a and 31b - see black dots. Further the work function courses of the corresponding sub-systems[34], $\Delta\Phi(\theta_{\mathrm{TFBQ}})$ and $\Delta\Phi(\theta_{\mathrm{TFBD}})$, are shown (red squares and blue diamonds).[35] Prior to the discussion of mixed monolayers here first we'll focus on sub-monolayers of TFBD and TFBQ to gain an understanding of the corresponding sub-systems.

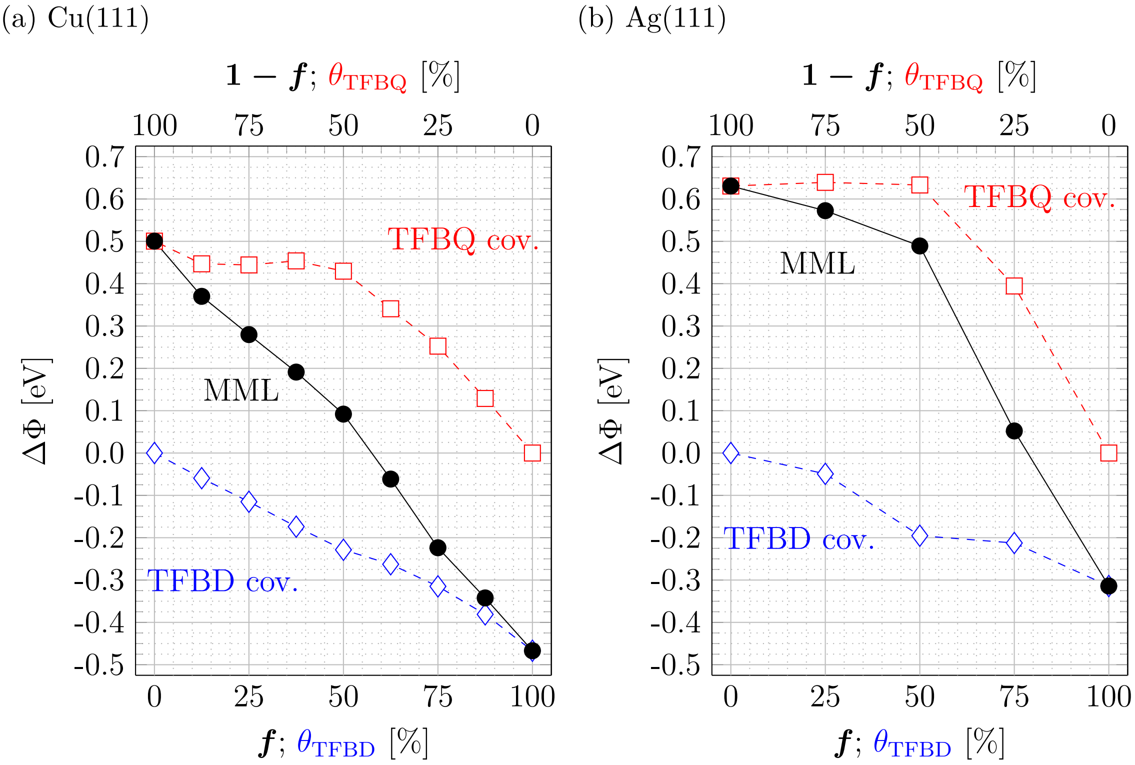

Figure 31: Change of $\Delta\Phi$ with TFBD fraction f in mixed monolayers (MML, black dots) adsorbed on (a) a Cu(111)- and (b) a Ag(111)-surface.For comparison – see text – $\Delta\Phi$ was also plotted for sub-monolayer cases with corresponding coverage $\theta_{\mathrm{TFBQ/TFBD}}$ (open, red squares and open, blue diamonds).

---

[33] This section contains contents of Edlbauer et al. [1, Paragraph "Work-Function Modifications as a Function of Coverage and Mixing Ratio"].

[34] The sub-monolayers; i.e., homogeneous monolayers of reduced coverage.

[35] Some parts of the analysis follow the approach in the work of Rissner et al. [87] who analyzed mixed SAMs with different tail-group substituents.

6.7.1 Sub-Monolayers of TFBD

The conceptually simplest system to study in that spirit is the adsorption of sub-monolayers of TFBD (blue diamonds in figure 31). As discussed before, here $\Delta\Phi$ originates from a bond dipole caused by Pauli-pushback, plus the molecular dipole. The magnitude of a Pushback-dipole depends mainly on the relative, local polarizabilities of substrate and adsorbate – compare Bagus et al. [88] –, neither of which are significantly dependent on the molecular coverage. Hence, every molecule induces basically the same dipole, with a depolarization that is, for instance, also seen for the coverage-dependence of dipolar self-assembled monolayers – compare Monti [89] and Romaner et al. [52]. Thus, one observes a nearly linear $\Delta\Phi(\theta_{\mathrm{TFBD}})$-dependence (blue dashed line).

Deviations from linearity can be traced back to variations of the molecular dipole due to a different arrangement of the hydroxyl groups at different coverages. To show this, we analyzed the contributions of the molecular and bond dipoles to $\Delta\Phi$ for sub-monolayers of TFBD on Ag(111) – see figure 32. The data shows that the deviation from linearity mainly stem from the change of the molecular dipole, whereas the contributions from the bond dipole nearly follows a linear course – actually one finds a slightly parabolic coverage dependence of the bond dipole.

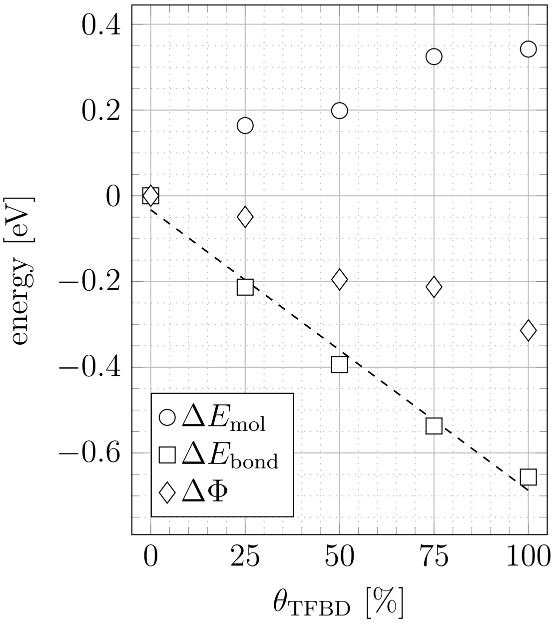

Figure 32: Contributions of the molecular dipole, ΔE_{mol}, and the bond dipole, ΔE_{bond}, to the work function modification, $\Delta\Phi$, for sub-monolayers of TFBD on Ag(111).

6.7.2 Sub-Monolayers of TFBQ

For TFBQ-adsorption on both substrates, $\Delta\Phi(\theta)$ remains essentially constant for coverages down to 50 % (see red squares in figures 31a and 31b). A significant decrease is found only at smaller θ. The region of constant $\Delta\Phi$ may seem surprising at first: Considering that the density of acceptors per area (θ) decreases, this implies that the dipole moment per TFBQ molecule increases. This is, in fact, exactly what one would expect for a Fermi-level pinned situation, where the bond dipole needs to be sufficiently large to shift the LUMO-derived band into resonance with the Fermi-energy (i.e., where the level alignment determines the dipole, rather than *vice versa*). For TFBQ on both metals at coverages between 100 and 50 %, this expectation approximately holds. Conversely, for coverages below 50 % the picture portrayed above collapses and the aforementioned, pronounced decrease of $\Delta\Phi(\theta)$ sets in. Naively, one might expect that this is accompanied by a similarly large shift of the LUMO-peak relative to the Fermi energy. Interestingly, this is not the case. As shown in figure 33, between $\theta = 100$ % and $\theta = 25$ % the LUMO peak shifts only by approx. 28 meV on Cu and 13 meV on Ag (compared to a change in $\Delta\Phi$ by

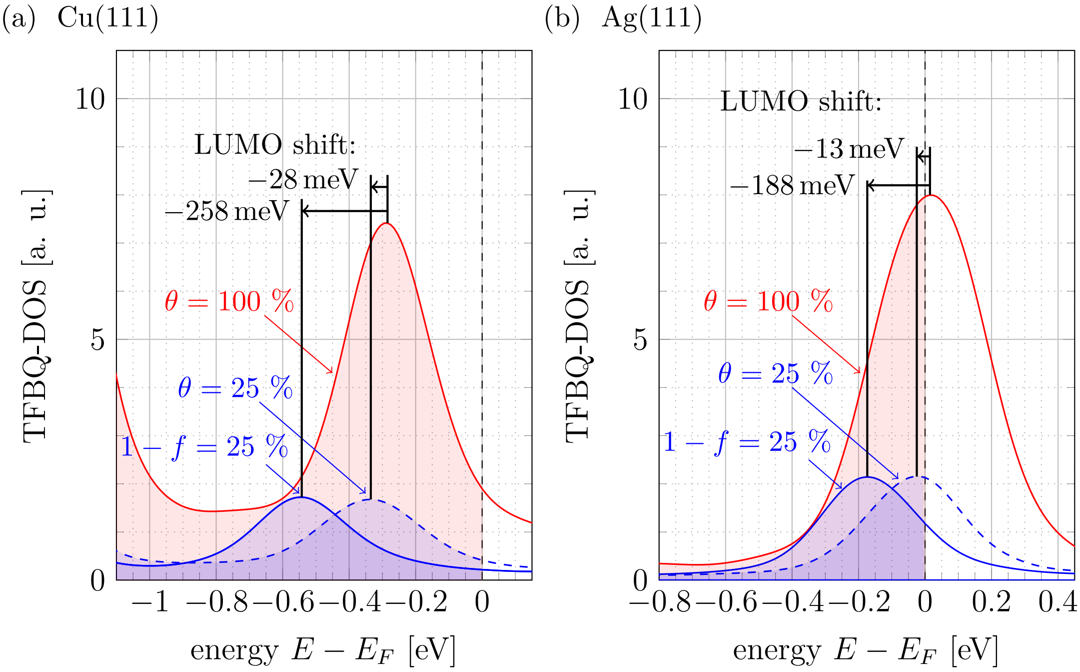

Figure 33: Comparison of the density of states for a TFBQ monolayer with $\theta = 100$ % (red line) and $\theta = 25$ % (blue, dashed line) and for a mixed monolayer with $1 - f = 25$ % (blue line) adsorbed upon (a) Cu(111) and (b) Ag(111). The black arrows indicate the shift of the LUMO-peak.

more than 0.5 eV).

Rather, the reduction of $\Delta\Phi$ originates from the inhomogeneity of the potential above the surface. To illustrate how this pertains to the present systems, we have calculated the adsorption-induced, plane-averaged potential rearrangements $\Delta U(z)$ at the adsorption sites of the TFBQ molecules for selected situations:

$$\Delta U(z) = \frac{1}{A} \iint\limits_{\text{TFBQ site}} \left[U_{\text{sys}}(\vec{r}) - U_{\text{slab}}(\vec{r}) - U_{\text{ml}}(\vec{r}) \right] d^2r \tag{6.4}$$

A	area of a TFBQ adsorption site
U_{sys}	electrostatic potential of the combined system
U_{slab}	potential of the metal without the adsorbed layer
U_{ml}	potential of the monolayer without the metal

For sub-monolayers of TFBQ with $\theta = 100$ % and $\theta = 25$ % adsorbed upon Cu(111) and Ag(111) the corresponding results are shown in figure 34a and 34b. How quickly the electric field above an array of dipoles decays (i.e., how fast a constant vacuum level is reached) depends sensitively on the dipole spacing – compare Natan et al. [51]. With a tightly packed homogeneous layer (red line), essentially no field above the layer is present and potential distribution resembles the case of a plate capacitor – compare red line in figure 34c. The situation changes markedly for sub-monolayers of TFBQ with $\theta = 25$ % (blue, dashed line): Due to the lower packing an electric field is present above the molecular plane affecting $\Delta\Phi$ beyond the Fermi-level pinning picture – compare Hofmann et al. [55]. In other words, the shift of the LUMO is no longer approximately determined by the bond dipole, as the commonly used picture of a plate capacitor modelling the charge rearrangements at the interface breaks down. Now the situation resembles more the case of sparsely packed point charges – compare blue line in figure 34c.

6.7.3 Mixed Monolayers

For mixed monolayers of TFBQ and TFBD (black circles in Figure 6), we find that $\Delta\Phi$ correlates strongly with f, indicating that changing the mixing ratio of these two molecules provides a sensible leverage to tune the work-function. This could not have been the case if $\Delta\Phi$ was determined exclusively by the Fermi-level pinned part of the system (TFBQ). Additionally two effects affect the situation: Due to the larger spacing of the TFBQ molecules in mixed monolayers as for sub-monolayers the plate-capacitor picture breaks down. Further the potential at the TFBQ site is additionally decreased by the potential originating from neighboring TFBD molecules. This effect has been discussed in detail by Rissner at al. [87] for

(a) Cu(111)

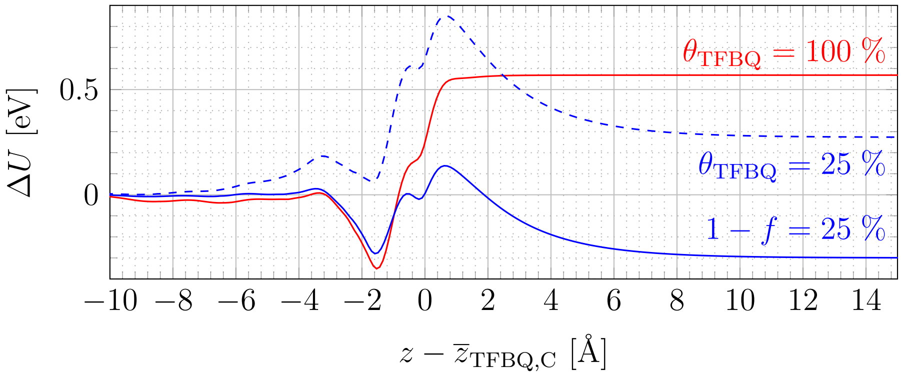

(b) Ag(111)

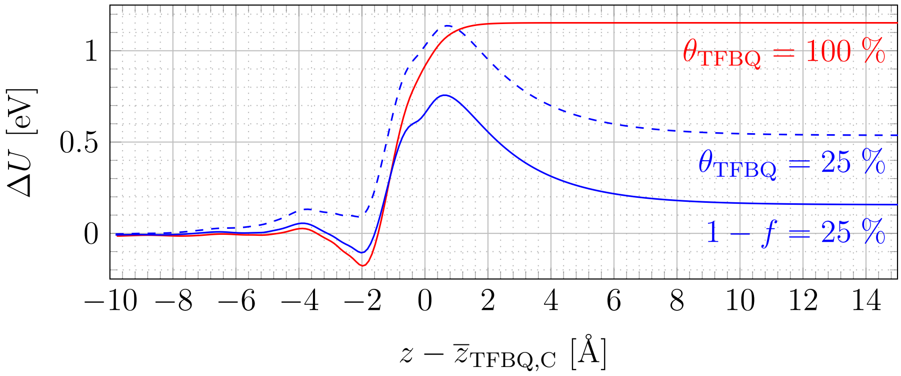

(c) Potential distributions for a plate capacitor and a point charge with corresponding mirror charge.

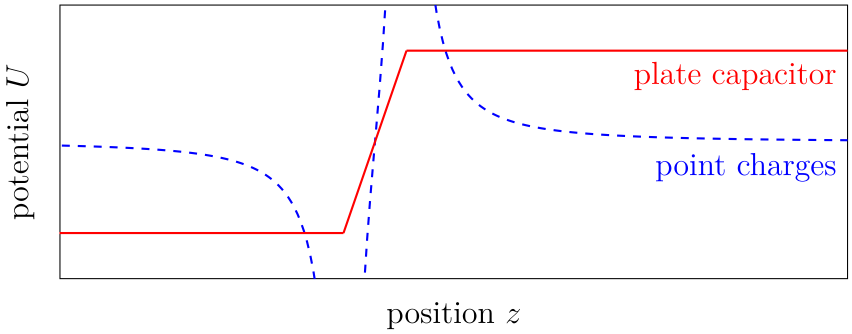

Figure 34: Potential rearrangements $\Delta U(z)$ due to adsorption of TFBQ monolayers with $\theta_{\mathrm{TFBQ}} = 100$ % (red line) and $\theta_{\mathrm{TFBQ}} = 25$ % (blue, dashed line) and for a mixed monolayer with $1 - f = 25$ % (blue line) on (a) Cu(111) and (b) Ag(111). The origins of the abscissa and the ordinate are aligned to the mean position of the carbon atoms of TFBQ and on the vacuum level below the slab. (c) Further sketches of potential distributions for the plate capacitor model and a point charge with corresponding counter charge is shown.

the case of mixed thiolate-bonded monolayers of upright-standing molecules. Here latter effect further affects Fermi-level-pinning.

Break-Down of the Plate Capacitor Model: In the corresponding course of $\Delta U(z)$ – see solid, blue line shown in figures 34a and 34b – the larger spacing of the Fermi-level-pinned molecules is reflected in the potential down-shift above the monolayer. Comparing $\Delta U(z)$ of the mixed monolayer case to the corresponding sub-monolayer case an additional potential down-shift due to the presence of the TFBD molecules is evident. This causes that below a crucial TFBQ fraction, $1-f$, the work function modification $\Delta\Phi$ successively is decreased to the $\Delta\Phi$-value of a homogeneous TFBD monolayer.

Effects on Fermi-Level-Pinning: In mixed monolayers, moreover, the Fermi-level-pinning mechanism is additionally affected by the potential caused by the TFBD molecules. This explain explains the significantly different $\Delta\Phi(f)$ dependences observed for on Cu(111) and Ag(111). In the following a brief explanation of this process is given by considering a TFBQ molecule immersing into the dipole field caused by a TFBD sub-monolayer.

The net charge formed at the TFBD-adsorption site due to the Pauli-pushback effect leads to a dipole field (see dashed, blue arrows in figure 35a). If only the TFBD sub-monolayer is present as adsorbate, this electric field would shift the VL to VL'. Let us now consider the hypothetical situation of a TFBQ molecule immersing into the TFBD dipole field: If the TFBQ molecule after adsorption is located above the TFBD sub-monolayer, the LUMO is shifted to LUMO' as the VL due to the TFBD dipole field – see situation 1 in figure 35. Upon interaction of TFBQ with the metal the Fermi-level-pinning mechanism now brings the LUMO in resonance with E_F – see red arrow shifting LUMO' to LUMO" in figure 35. Corresponding to the Fermi-level-pinning induced charge transfer to TFBQ the VL is shifted – see red arrow shifting VL' to VL" in figure 35 – resulting in the work function, Φ_1. Reducing the adsorption height of the TFBQ molecule the magnitude of the TFBD induced LUMO shift now successively is mitigated. For an adsorption height slightly smaller than that of the TFBD molecules the LUMO shift and, thus, Φ_2 hardly changes – see situation 2 in figure 35. If the TFBQ adsorption height is further decreased – see situation 3 in figure 35 – the effects on the LUMO shift become noticeable resulting in a decreased work function, Φ_3. The two discussed situations of TFBQ slightly and further immersed into the TFBD dipole field resemble the situations of mixed monolayers on Ag(111) and Cu(111). Due to the larger adsorption height of TFBQ in mixed monolayers on Ag(111) with increasing TFBD fraction, f, the

(a) Selected situations for a TFBQ molecule immersing in a dipole field (blue, dashed arrows) caused by a TFBD sub-monolayer:

1. .... above TFBD – i.e., a hypothetical situation.
2. .... slightly below TFBD – resembles situation on Ag(111).
3. .... further below TFBD – resembles situation on Cu(111).

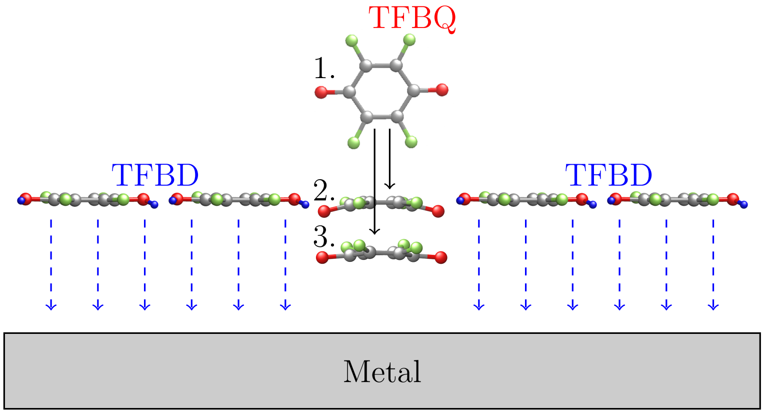

(b) Energy level alignment for the different cases.

VL’ .... VL caused by the dipole field of the TFBD sub-monolayer.
VL” .... VL in mixed monolayers with Fermi-level pinning.
LUMO’ .... LUMO after shift by the TFBD dipole field.
LUMO” .... LUMO in mixed monolayers after Fermi-level-pinning.

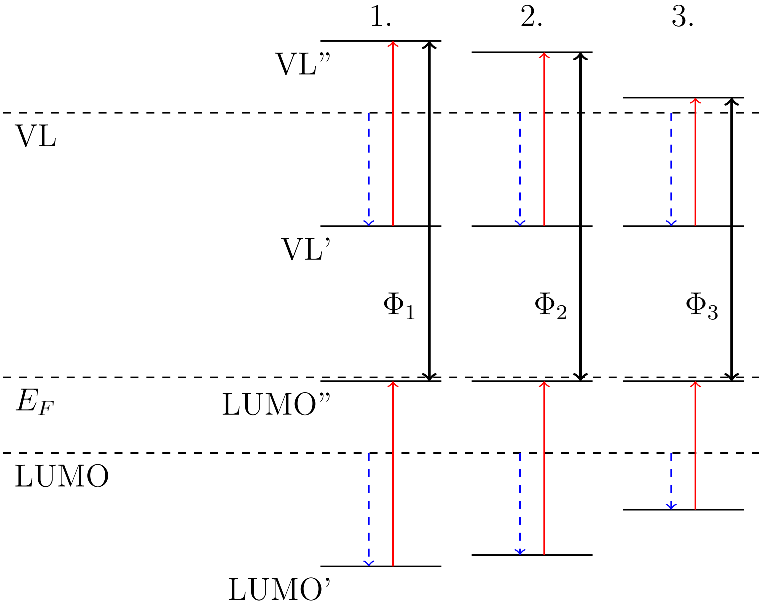

Figure 35: Sketches to understand Fermi-level-pinning in mixed monolayers of TFBD and TFBQ: (a) Side view on selected situations and (b) corresponding energy level alignment due to Fermi-level-pinning.

LUMO is shifted by the TFBD dipole field by a lesser extent than on Cu(111) what is reflected in the work function modification, $\Delta\Phi(f)$, – compare figure 31.

Note that within this idealized picture the LUMO-peak is modelled as a Delta-Distribution. However, due to the interaction of an adsorbed molecule with the substrate and neighboring molecules the molecular energy levels broaden significantly. This causes that the Fermi-level-pinned LUMO-peak is not directly located at E_F – as sketched in figure 35. Further, the LUMO-energy of the separated hypothetical, free standing monolayer in the Schottky-Mott-limit is not a constant for different conformations of the layer. Despite the higher work function of Cu, therefore, it occurs that on Ag the Fermi-level-pinned LUMO-peak is closer to E_F.

6.7.4 Semi-Electrostatic Model for Fermi-Level-Pinning

To simulate the work function dependence on the TFBD fraction, $\Delta\Phi(f)$, of mixed monolayers (containing TFBD and the Fermi-level-pinned TFBQ) we developed a semi-electrostatic model. There we describe the molecules of the monolayer adsorbed on a certain coinage metal surface as point charges, q. The interface dipoles causing the work function modification, $\Delta\Phi$, are modelled via counter charges, $q' = -q$. On a hexagonal grid with fixed spacing d corresponding to the two-dimensional lattice of the TFBQ or TFBD adsorbate on Cu(111) or Ag(111) at a fixed height h above and below a mirror plane the charges q and q' are placed – see sketch in figure 36. Note that we didn't use periodic boundary conditions, but simulated the monolayer as a large cluster.

Up to this point, the model is completely based on electrostatics. Now the quantum-mechanical concept of Fermi-level pinning comes into play that we simulate via self-consistent field iterations starting from the Schottky-Mott-limit – that is the consideration of the separated systems of the free-standing monolayer and the metal slab. The iteration-scheme for this procedure is shown in figure 37. Depending on the EA of the adsorbed molecule the energy of the LUMO in the free-standing monolayer of the Schottky-Mott-limit is located at a certain energy, ϵ, relative to E_F. Due to the interaction with the surface the LUMO-peak broadens. Here, we model the peak as a Gaussian function, with the full width at half maximum, $FWHM = 2 \cdot \ln(2 \cdot \sigma)$. Then q is determined by the integral of that function to E_F:

$$q(\epsilon) = \int_{-\infty}^{E_F} \frac{2}{\sqrt{2 \cdot \pi \cdot \sigma^2}} \cdot \exp\left[\frac{(E-\epsilon)^2}{2 \cdot \sigma^2}\right] dE = \operatorname{erfc}\Big[-\frac{E_F - \epsilon}{\sqrt{2} \cdot \sigma}\Big] \tag{6.5}$$

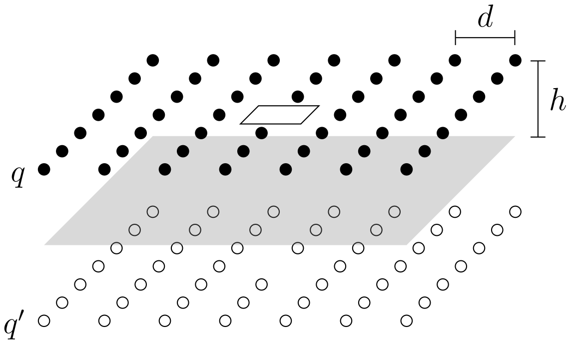

Figure 36: Sketch of the spatial arrangement of the charges (dots) and counter charges (circles) for the calculation of the electron potential at the emptied site (bordered cell).

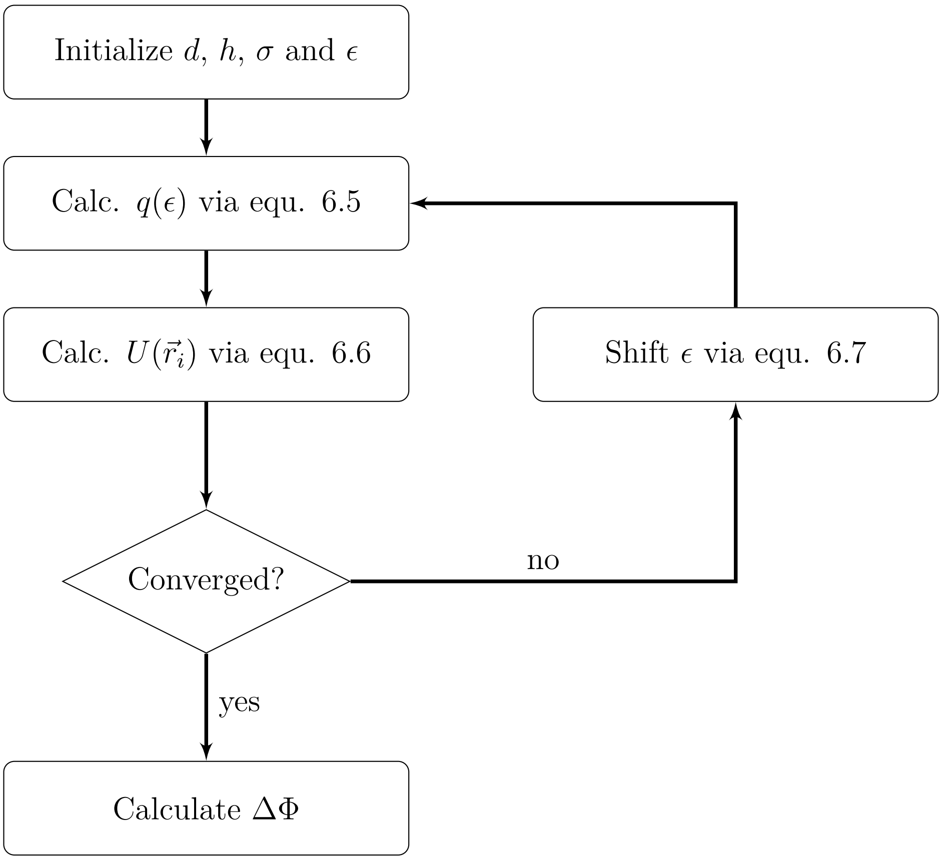

Figure 37: Scheme of the self-consistent cycle for the electrostatic Fermi-level-pinning model. The convergence criteria is that the charge doesn't change.

Then, at the site of a certain centrally located charge i the electrostatic potential due to all other charges j can be calculated:

$$U(\vec{r}_i) = \sum_{j \neq i} \left[\frac{q}{|\vec{r}_i - \vec{r}_j|} + \frac{q'}{|\vec{r}_i - \vec{r}_j'|} \right] \tag{6.6}$$

Now ϵ is shifted by $U(\vec{r}_i)$ to approach a self-consistent situation:

$$\epsilon = \epsilon + U(\vec{r}_i) \tag{6.7}$$

Those steps – calculation of $q(\epsilon)$ and $U(\vec{r}_i)$ and the shift of ϵ – now form the self-consistent cycle that is repeated until the charge is sufficiently converged.
Finally the question arises, how to estimate $\Delta\Phi$ for that system. Every point charge causes a singularity in the potential distribution. Strictly speaking for a cluster $\Delta\Phi$ is zero because for $z > h$ the potential monotonously decreases, $U(x, y, z \to \infty) = 0$. If, however, at a certain centrally located site, (x,y,h), a single charge with its counter charge is removed with for $(x_{\text{empt.}},y_{\text{empt.}},h)$ now a plateau of the potential is formed. The maximum potential above the emptied adsorption site, $U(x_{\text{empt.}}, y_{\text{empt.}}, z_{\text{max.}})$, then can be used to estimate $\Delta\Phi$ for the case of an infinitely extended cluster, if the values of q and q' are converged and if the number of charges modelling the adsorbate is sufficiently large. Comparing the $\Delta\Phi$ predictions of this approach to the plate capacitor model – see equation 2.39 in chapter 2.2.2 – for the case of a charge of 0.1 e at a distance of 1.5 Å in a two-dimensional, hexagonal unit cell and with a lattice constant of 7.7 Å one finds that with increasing number of charges in the cluster the approach converges to the $\Delta\Phi$ value predicted by the plate-capacitor model – see figure 38.

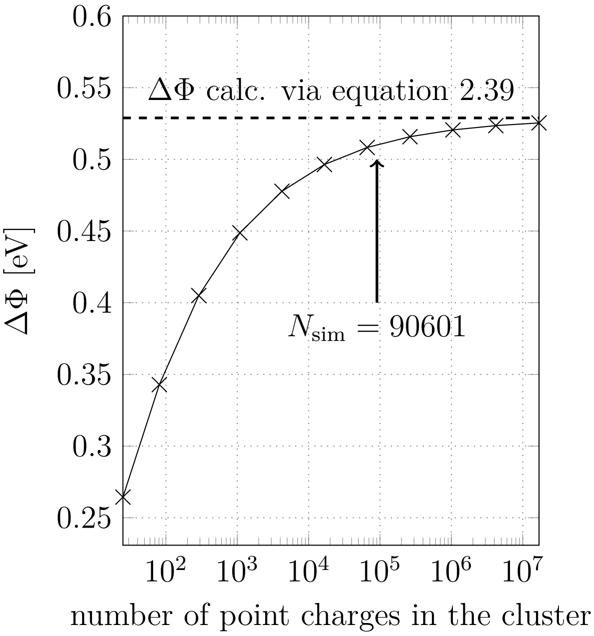

Figure 38: Convergence of the $\Delta\Phi$-estimation-approach with increasing number of point charges in the cluster for a selected case – for detail see text. The number of point charges that was used for the simulations of sub-monolayers and mixed monolayers of TFBQ and TFBD, N_{sim}, is indicated via an arrow.

Using this approach we simulated the $\Delta\Phi(\theta)$ dependence of sub-monolayers of Fermi-level-pinned molecules on a metal surface with increasing coverage, θ, by continuously decreasing the grid spacing, d:

$$d = \sqrt{a^2 \cdot \theta^{-1}} \tag{6.8}$$

a … lattice constant of the two-dimensional, hexagonal unit cell of the TFBQ or TFBD adsorbate.

To simulate $\Delta\Phi$ for mixed monolayers of TFBQ (Fermi-Level-pinning and Pauli-pushback) and TFBD (only Pauli-pushback) we divided the system in it's sub-systems. The approach is sketched in figure 39 for a TFBD fraction of $f = 50\ \%$. The sub-systems are sub-monolayers of TFBD (blue diamond) and TFBQ (red squares) of complementary coverage:

$$\theta_{\text{mixed}} = \theta_{\text{TFBQ}}(f) + \theta_{\text{TFBQ}}(f) = 100\ \% \tag{6.9}$$

To simulate the $\Delta\Phi$ dependence on the TFBD fraction, f, in the sub-systems the TFBD-coverage is increased while the TFBQ-coverage is correspondingly decreased. The point charges of the TFBD-sub-system are only determined by Pauli-pushback and, hence, are kept constant. For the TFBQ-sub-system multiple effects come into play: First charge rearrangements from Pauli pushback and hybrydization lead to a molecule to metal electron transfer. Further, the additional presence of TFBD in such mixed monolayers affects the Fermi-level-pinning mechanism of the TFBQ-LUMO peak: The electric field caused by the Pauli-pushback effect of the TFBD molecules shifts the TFBQ-LUMO down in energy (see dashed, blue arrow) before Fermi-level-pinning takes place (see solid, red arrow).

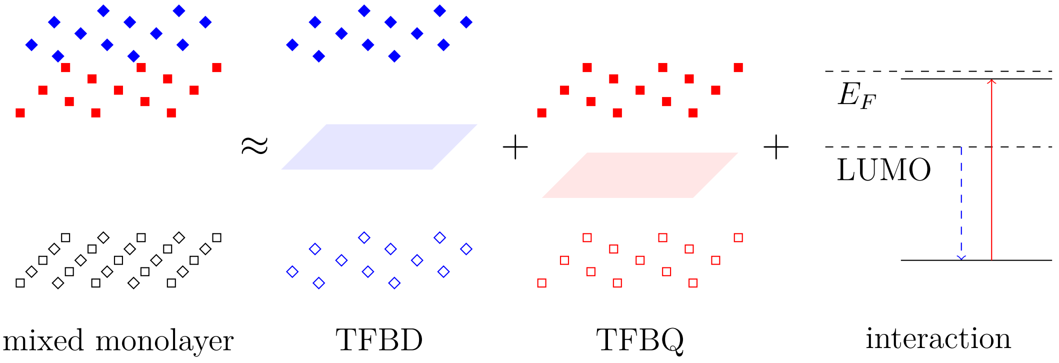

Figure 39: Sketch to understand the semi-electrostatic model of mixed monolayers of TFBQ and TFBD. The mixed monolayer is modelled as sub-monolayers of TFBQ and TFBD with complementary coverage additionally taking into account the effects of the TFBD dipole field on Fermi-level-pinning of the TFBQ-LUMO.

The source code of the model implemented in Python is given in appendix A. With suitable settings of the variables – see the variable "settings" in appendix A – the work function modifications for sub-monolayers and mixed monolayers of TFBQ and TFBD were simulated. The settings of the variables were chosen such to approximate the observed situation of mixed monolayers of TFBQ and TFBD: The spacing of the two-dimensional, hexagonal point charge grid was chosen as the spacing of the molecules in the two-dimensional unit cells on Cu(111) and Ag(111): 7.70 Å for Cu(111) and 7.77 Å for Ag(111). Here we assume that the adsorption height defines the distance of the charges at the molecular sites, q, to the counter charges, q' in the metal. Therefore, the distance, d, in the semi-electrostatic model is approximately half of the adsorption height of the monolayer cases. For TFBQ the distance to the mirror plane, d, was chosen as 1.05 Å for Cu(111) and 1.25 Å for Ag(111) corresponding to the mean adsorption height of the oxygen atoms in the homogeneous monolayer. For TFBD d was chosen as 1.54 Å for Cu(111) and 1.59 Å for Ag(111) corresponding to the mean adsorption distances of all atoms in the homogeneous monolayer. The broadening of the LUMO-peak, σ, was chosen as 0.4 eV (full width at half maximum) corresponding to the observed width of the peaks in the species-projected DOS shown in figure 27. The position of the LUMO in the Schottky-Mott limit, ϵ, and the electron back-transfer to the metal from TFBQ was chosen such to fit the data points and that the LUMO energy after adsorption was close to the peak positions of the species-projected DOS shown in figure 27. Molecular dipoles of TFBD were linearly interpolated corresponding to the results of homogeneous TFBD monolayers of full coverage. Molecular dipoles of TFBQ were neglected.
Note that for the simulation of $\Delta\Phi$ for mixed monolayers on Cu(111) additionally a small linear reduction of the electron back-transfer to the metal from Pauli pushback and hybridization was performed to fit the data points. We assume that this modification is necessitated due to the increased adsorption height of the carbon backbone with f that is observed for Cu(111) but not for Ag(111). That spatial increase of the carbon backbone on Cu(111) likely mitigates the Pauli pushback effect, what is reflected in a reduced net electron transfer from the molecule to the metal.
Despite the performed simplifications the courses of $\Delta\Phi$ predicted by the semi-electrostatic model show good agreement with the results calculated via DFT – see figure 40. The semi-electrostatic model reflects the mechanisms for the energy level alignment in mixed monolayers of TFBQ and TFBD, however, it does not properly describe the situation, due to neglecting the molecular dipole of TFBQ and extended charge distributions.

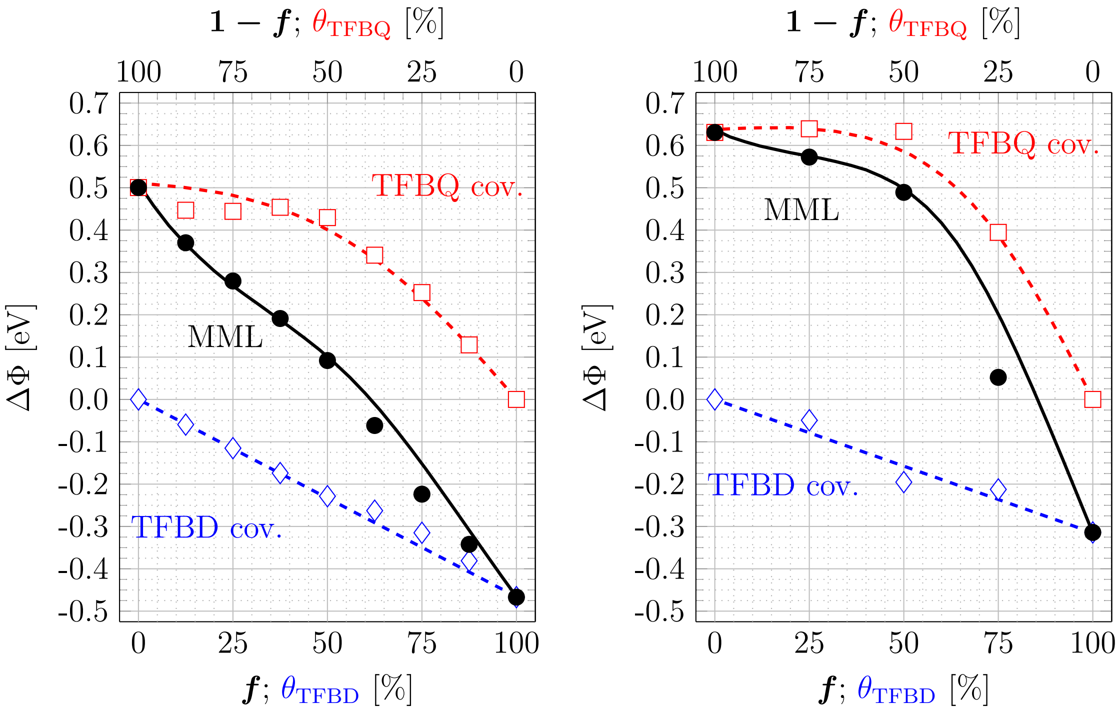
(a) Cu(111)

(b) Ag(111)

Figure 40: $\Delta\Phi(f)$ predicted by the semi-electrostatic model for mixed monolayers (MML, black line) adsorbed upon a (a) Cu(111)- and a (b) Ag(111)-surface. For comparison also $\Delta\Phi(\theta_{\mathrm{TFBQ/TFBD}})$ for the corresponding sub-monolayer cases are plotted (dashed, red and blue line). For details to the simulation settings see text. The results of the DFT calculations are shown as symbols (black dots, red squares and blue diamonds) – compare figure 31.

6.8 Hartree Potential Energy above the Surface

Charge-injection barriers are determined by the energy distance of E_F to the transport level in the organic semiconductor material – approximately, that is the HOMO for holes and the LUMO for electrons. So far we investigated, how the adsorption of a mixed monolayer of TFBQ and TFBD on coinage metal surfaces affects Φ and, thus, E_F. Now we go one step further and focus on the effects of the adsorbate on the transport level in the overlying organic semiconductor layers.

A clean coinage metal surface shows a very homogeneous distribution of the electron potential energy along any direction in the x-y-plane along the surface. If a monolayer of a certain organic molecule is adsorbed, the electron potential energy above the surface changes: Depending on the adsorption mechanism dipoles are formed that cause a corrugation of the electron potential energy above the surface. According to this potential energy "landscape" at a certain distance to the metal surface, z, the transport levels of further deposited layers are shifted in energy. At spatial regions of negative potential energy relative to the vacuum level (VL) upon the surface electron injection barriers are decreased, because the LUMO moves – following the potential energy corrugation – down in energy. Due to the HOMO shift to lower energies hole injection barriers, on the other hand, are increased. Conversely, is the situation for spatial regions of positive potential energy, where the transport level moves up in energy. If in the electron potential energy "landscape" pronounced, local peaks occur, preferred spatial regions for charge-injection can arise. When operating the device, at those "hot spots" due to the strongly increased current density high temperatures may occur causing damage of the device.

In the following, we first analyze the electron potential energy at a fixed distance z to the uppermost metal layer via contour-plots parallel to the surface. For this we calculated the long range electron potential energy above supercell geometries. The long range potential energy is used for regions where no electron density is found.

> "..., the long-range part of the Hartree potential energy is treated by Ewald's method using a Fourier transform, ..." [38]

and is much faster to calculate than the full potential energy.[36] We discuss the corrugation of the this potential energy regarding "hot spot" formation for mixed monolayers of TFBQ and TFBD on the coinage metal surface Cu(111) and Ag(111).

---

[36] For this investigation we didn't use the full electron potential energy, because at that time a proper implementation in FHI-*aims* was not available. However, recently an implementation of the full electron potential energy was developed, which includes exchange-correlation terms affecting especially the potential energy close to the atoms.

We then introduce a measure for the corrugation of the potential energy and discuss it's dependence on z.

6.8.1 Contour Plots at fixed Height

For 4×2 supercell geometries with mixed monolayers adsorbed on Cu(111) the electron potential energy distributions above the surface are shown as contour-plots in figure 41 for selected cases. The red and blue regions in those contour plots indicate negative and positive deviations of the electron potential energy to the vacuum level – see colour-bar for energy values. There the distance to the uppermost metal layer is $z \approx 6$ Å.[37] Corresponding to the LUMO and HOMO shifts, red indicates preferred regions of electron injection. For hole injection favourable spatial regions are coloured in blue. The limiting cases of homogeneous monolayers of TFBQ and TFBD – see figures 41a and 41e – show a small corrugation along the sub-cells of the supercell. In TFBQ monolayers, hole injection barriers are increased over the centers of the molecules. They are decreased in the "valleys" between the molecules. Due to the uniform corrugation of the electron potential energy here no "hot spot" formation is expected. When a single TFBD molecule is introduced into a 4×2-supercell of a homogeneous TFBQ monolayer – see figure 41b –, an additional decrease of the electron potential energy arises over the centers of TFBQ and TFBD molecules that are connected via hydrogen bonds (HB). The amplitude of those peaks is about 0.1 eV higher than for peaks located over TFBQ molecules without HB. For electron transport the increased peak represents a spatial region with decreased electron-injection barrier. When the corrugation is sufficient to affect the propagation of the charge carriers strongly, "hot spot" formation for electron-transport may take place for mixed monolayers with small TFBD fractions, f.[38] For the complementary case of insulated TFBQ molecules in TFBD layers – see figure 41d – especially at the HB to neighboring TFBD molecules decreased hole injection barriers occur at the TFBQ sites. Comparing the depth of those potential energy trenches to that of TFBD molecules without HB, we again find an energy difference of about 0.1 eV what may be sufficient for "hot spot" formation of hole injection.[39] With $f \rightarrow 50$ % – see figure 41c – the potential energy distribution above the surface

---

[37] This value is measured to the mean position of the atoms of the uppermost metal layer.

[38] However, electron-transport in organic semiconductors often is a minor phenomenon. The majority charge-carriers are mostly holes.

[39] To answer the question, whether 0.1 eV energy difference in such distributed charge-injection barriers is enough for "hot spot" formation, we would further have to investigate the dynamics of charge propagation in such potential energy distributions. Because this goes beyond the scope of this thesis, here, we have to leave the answer to this question open.

(a) $f = 0.0$ %.

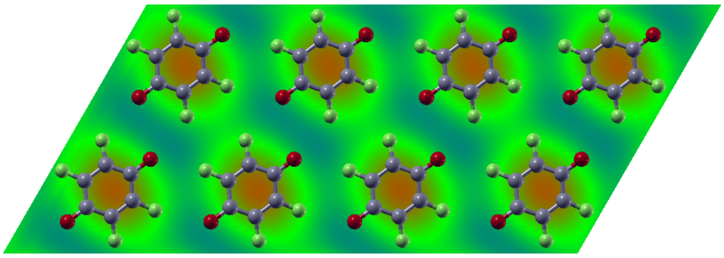

(b) $f = 12.5$ %.

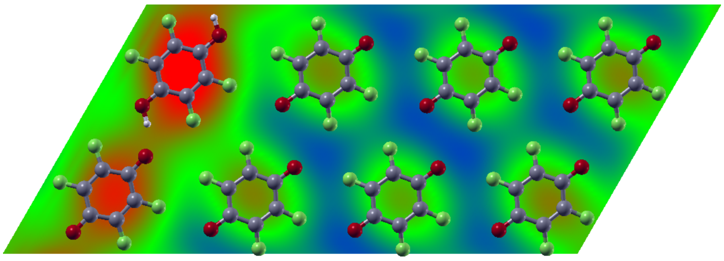

(c) $f = 50.0$ %.

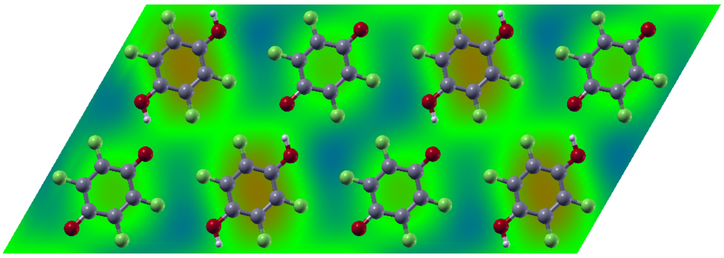

(d) $f = 87.5$ %.

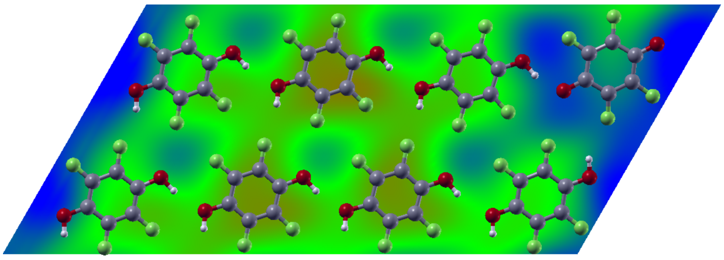

(e) $f = 100.0$ %.

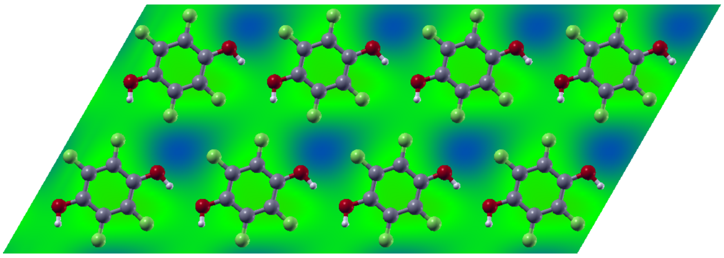

(f) Colorbar.

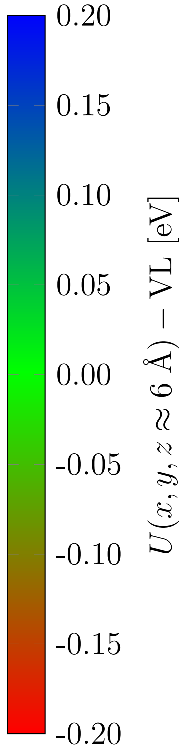

(g) Coord. system

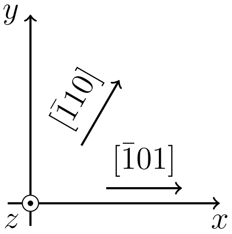

Figure 41: Contour plots of the electron potential energy distribution, $U(\vec{r})$, about 6 Å above the uppermost Cu(111) layer with mixed monolayer adsorbate of f =0.0, 12.5, 50.0, 87.5 and 100.0 %. The zero-point of the potential energy distributions is aligned to the upper vacuum level – green area in the color-plot.

restores homogeneity.

The electron potential energy 6 Å above a Ag(111)-surface with similar mixed monolayer adsorbates is shown as contour-plots in figure 42. For the limiting cases of homogeneous monolayers of TFBQ and TFBD – see figures 42a and 42e – as for Cu(111) one finds a uniform corrugation of the electron potential energy. For a mixed monolayer with a TFBD fraction of $f = 50.0$ % one also finds a distribution of the electron potential energy that strongly resembles the corresponding result on Cu(111). Further with a TFBD fraction of $f = 12.5$ % – see figure 42b – as on Cu(111) one finds that an additional decrease of the electron potential energy occurs over the center of the TFBD molecule. However, on the neighboring site of the TFBQ molecule that is connected via a hydrogen bond the potential energy is increased. This indicates that for small TFBD fractions on Ag(111) "hot spot" formation is more likely than on Cu(111). For high TFBD fractions as $f = 87.5$ % – see figure 42d – a very strong corrugation of the potential energy is observed that is connected with a different local energy minimum that was obtained in the geometry optimization process. Instead to the left and right – i.e, the $[\bar{2}\bar{1}3]$ direction –, here the hydrogen bonds are directed to the upper and lower neighbours – i.e., the the $[\bar{3}21]$ direction. Due to the 4×2 supercell geometry this leads to a distribution, where the electron potential energy is stongly increased along chains of alternating TFBQ and TFBD molecules that are connected via hydrogen bonds. For single TFBQ molecules merely surrounded by TFBD with such chains the increase of the electron potential energy is about 0.2 eV larger than without.

(a) $f = 0.0$ %.

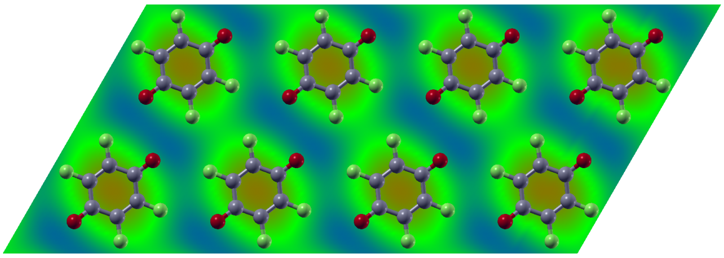

(b) $f = 12.5$ %.

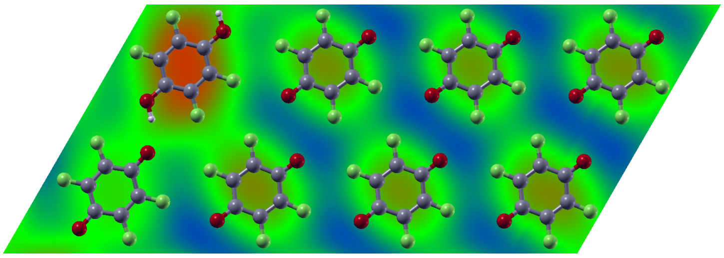

(c) $f = 50.0$ %.

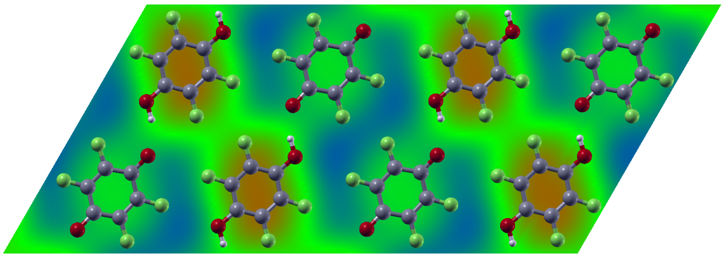

(d) $f = 87.5$ %.

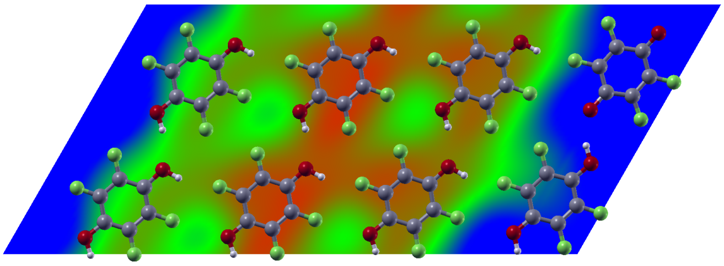

(e) $f = 100.0$ %.

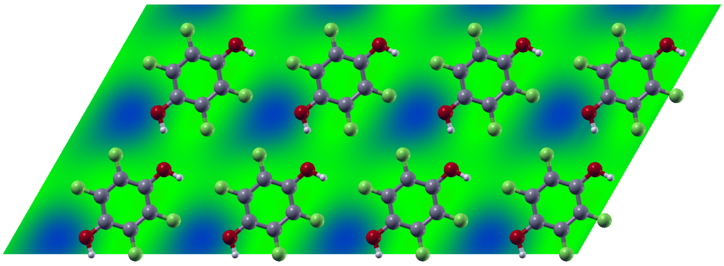

(f) Colorbar.

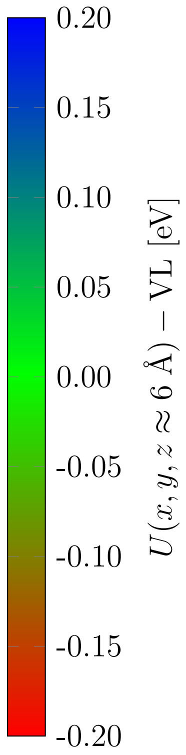

(g) Coord. system.

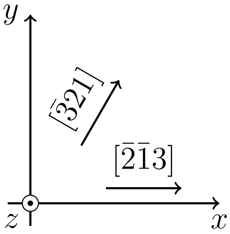

Figure 42: Contour plots of the electron potential energy distribution, $U(\vec{r})$, about 6 Å above the uppermost Ag(111) layer with mixed monolayer adsorbate of f =0.0, 12.5, 50.0, 87.5 and 100.0 %. The zero-point of the potential energy distributions is aligned to the upper vacuum level – green area in the color-plot.

6.8.2 Corrugation Dependence on the Distance to the Surface

The corrugation of the electron potential energy can simply be quantified by the difference of the maximum and minimum value at a certain height z:

$$\Delta U(z) = U_{\max}(z) - U_{\min}(z) \tag{6.10}$$

For mixed monolayers with various TFBD fractions, f =0.0, 12.5, 50.0, 87.5 and 100.0 %, on Cu(111) and Ag(111) $\Delta U(z)$ was calculated. The corresponding results are shown in figures 43a and 43b. There it is apparent that for both coinage metals the corrugation decreases nearly exponentially with distance to the adsorbate z – especially for $z > 7$ Å. Further, one finds that for homogeneous monolayers – $f = 0$ and 100 % – the corrugation decreases much faster with distance z then for the other investigated mixed monolayer cases. This results from the different arrangements of dipoles in homogeneous and mixed monolayers: Parallel dipole-alignments cause a much weaker corrugation of the electron potential energy than anti-parallel, as shown in figures 44a and 44b. Interestingly for mixed monolayers of f =12.5 % and 87.5 % the corrugation is much larger than for f =50 %. For instance at height of $z = 8$ Å above the metal surface – that is a height of about 5 Å to the charge-injection layer – the potential energy corrugation still is larger than 0.1 eV for f =12.5 and 87.5 %. Further, for f =12.5 and 87.5 % strong deviations in $\Delta U(z)$ are apparent between the results regarding Cu(111) and Ag(111): On Cu(111) the lines for the two TFBD fractions are very similar – see orange and cyan lines in figure 43a. Comparing the results on Ag(111) one finds that the corrugation for f = 87.5 % is larger and reaches a few Å further than on Cu(111). For f =12.5 % on the other hand the corrugation is smaller and reaches about 1 Å shorter that on Cu(111) at a corrugation of 0.1 eV.

This shows that the corrugation of the electron potential energy at a certain height z is strongly dependent on the TFBD-fraction in the mixed monolayer and the alignment of the molecules therein. For the estimation of the effect of the electron potential energy on the transport level in overlying organic material the spacing of the first adsorbate layers is crucial due to the exponential decrease of the potential energy.

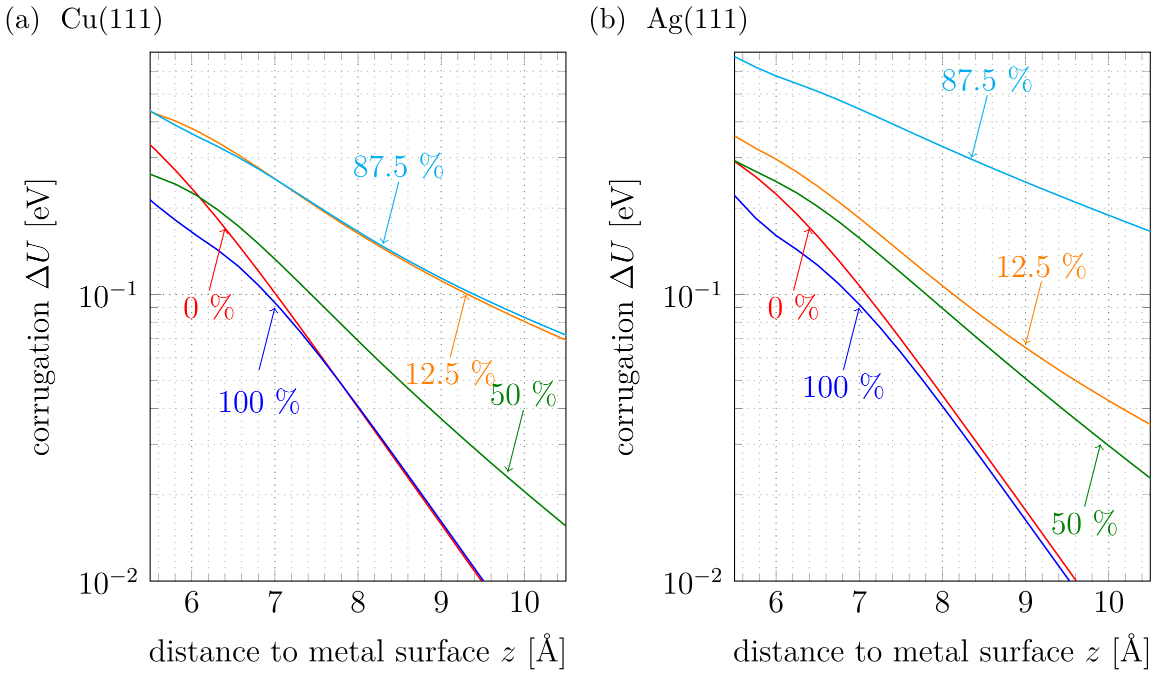

Figure 43: Corrugation of the electrostatic potential above mixed monolayers adsorbed upon (a) Cu(111) and (b) Ag(111). As measure for the corrugation we use the difference between the maximum and minimum values of the potential energy at a certain height z: $\Delta U(z) = U_{\max}(z) - U_{\min}(z)$. The TFBD fractions, f, that belong to the data sets are annotated via arrows.

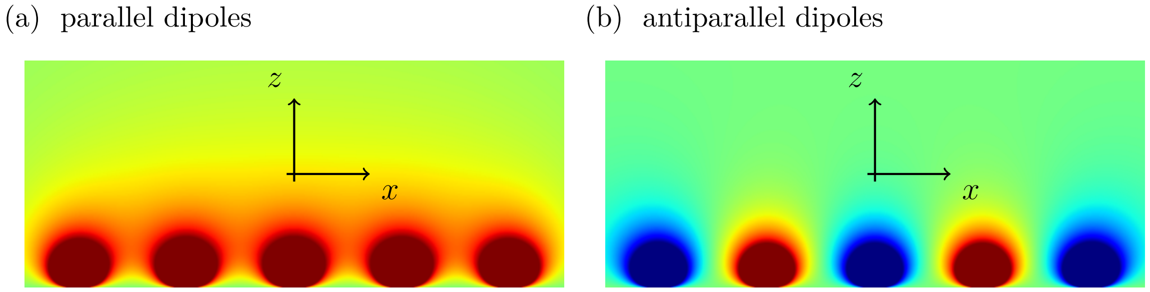

Figure 44: Contour plots of the potential energy distribution of dipole lines with *(a)* parallel and *(b)* anti-parallel orientations of the dipoles. The horizontal x-axis indicates an arbitrary direction in the surface plane.

6.9 Tuning the TFBD Fraction after Adsorption via Hydrogen Pressure Control[40]

Here we analyze by which extent the ratio of the electron-donating molecules, f, in a mixed monolayer containing TFBQ and TFBD can be tuned through conrol of the hydrogen partial pressure, p_{H_2}. As described in the fundamentals to *ab initio* thermodynamics – see section 2.3 –, an interface of a solid and a surrounding gas phase, modelled as isothermal-isobaric ensemble, strives to minimize the excess Gibbs free energy per area γ of the system. Here we consider the situation for the adsorption of hydrogen on a full monolayer of TFBQ, adsorbed on the respective metal – see figure 45a. We implicitly assume that hydrogen preferentially adsorbs

(a) Solid phase serving as reference system. The total energy that belongs to this phase is denoted as E_{solid}.

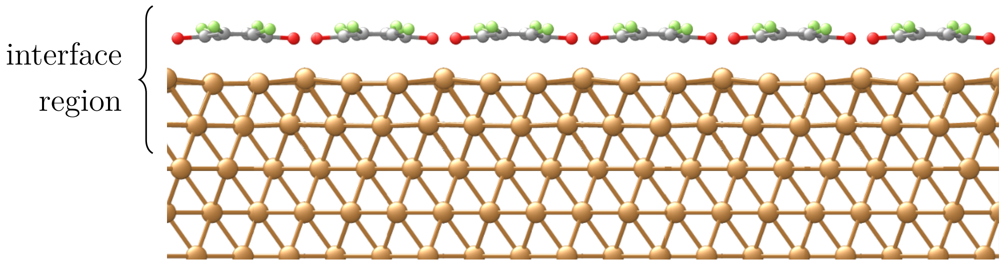

(b) Sketch of a favourable conformation due to interaction with a hydrogen gas phase. The total energy corresponding to the interface region for this particular geometry is denoted as E_{sys}.

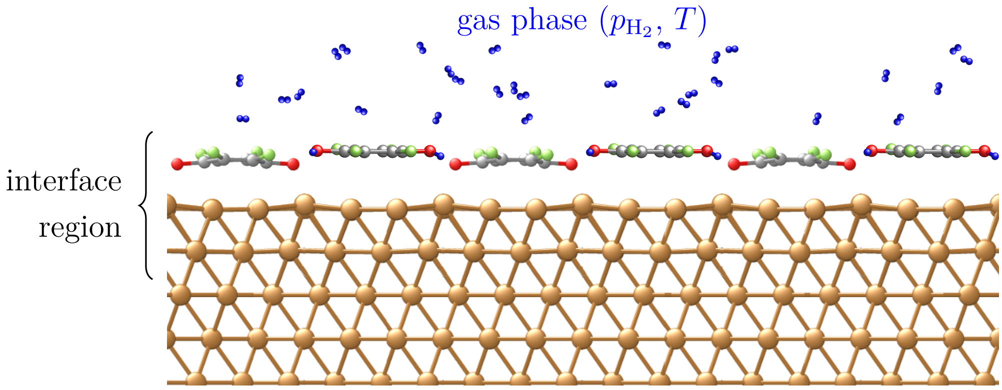

Figure 45: A set of sketches to establish understanding for the systems contributing to the *ab initio* thermodynamics model: (a) Solid phase; (b) Favourable conformation due to interaction with a hydrogen gas phase.

---

[40] This section contains contents of Edlbauer et al. [1, Paragraphs "*Ab Initio* Thermodynamics" and "Mixed Monolayers and Hydrogen Pressure Dependence"].

on the TFBQ molecules (rather than on the metal), forming TFBD in the process – see figure 45b. The organic molecules and the metal are treated jointly as solid phase, considering a fixed packing density (i.e, no desorption of organic material is considered).

In thermodynamic equilibrium, the diol fraction, f will assume the value that minimizes γ at a given temperature, T, and for a given hydrogen pressure p_{H_2}. For any f, γ is then given as:

$$\gamma = \frac{1}{A}(E^{\mathrm{sys}} - E^{\mathrm{solid}} - \mu_{\mathrm{H}_2} \cdot N_{\mathrm{H}_2} + p \cdot V - T \cdot S^{\mathrm{conf}} + F^{\mathrm{vib}}) \tag{6.11}$$

A	area of the investigated supercell
E^{sys}	ground state energy of the entire system
E^{solid}	ground state energy prior to adsorption of H_2, i.e., the energy of a homogeneously TFBQ-covered surface.[41]
p, V	total pressure and volume
μ_{H_2}	chemical potential of hydrogen
N_{H_2}	number of hydrogen molecules reacting with TFBQ to TFBD
S^{conf}	configurational entropy
F^{vib}	vibrational free energy

Note that while this term often refers to a pristine, uncovered surface, here the system prior to adsorption of H_2 consists of the metal with a full monolayer of TFBQ on it. The reaction of TFBQ with a single hydrogen yields a radicalic species, which is highly reactive and unstable.

We, therefore, always consider the complete reduction from TFBQ to TFBD. As a consequence of that and because our 2×2 and 4×2 supercells always contain exactly four or eight molecules ($N_{\mathrm{TFBQ}} \in \{4, 8\}$), respectively, N_{H_2} can be related to f via $f = \frac{N_{\mathrm{H}_2}}{N_{\mathrm{TFBQ}}}$. The mechanical work term, $p \cdot V$, can be safely neglected [58]. An upper estimate for S_{conf} can be provided by assuming that, for a given f, all conformations are degenerate. S_{conf} is then simply proportional to the *logarithmus naturalis* of the number of possible configurations. This is largest for $f = 50$ %, where S_{conf} takes a maximum value of approx. $1.2 \cdot 10^{-6} \frac{\mathrm{eV}}{\mathrm{K\,\AA^2}}$, prompting us to neglect this contribution. F^{vib} describes the change in the vibrational free energy upon adsorption. This term is commonly neglected in literature, mostly due to the high computational effort required to obtain it. However, it cannot be completely ignored here, since the adsorption of hydrogen changes the chemical nature of all bonds of the adsorbate, as it induces the quinone-to-aromat transition. It also qualitatively affects the interac-

---

[41] Note that while this term often refers to a pristine, uncovered surface, here the system prior to adsorption of H_2 consists of the metal with a full monolayer of TFBQ on it.

tion between the organic material and the substrate. The impact of whether there are TFBQ or TFBD molecules in neighboring unit cells on the vibrations can be expected to be negligibly small. Thus, we calculated the vibrational free energy only for homogeneous TFBQ and TFBD monolayers ($F^{\mathrm{vib}}_{\mathrm{TFBD,ads}}$ and $F^{\mathrm{vib}}_{\mathrm{TFBQ,ads}}$) and for an isolated hydrogen molecule ($F^{\mathrm{vib}}_{\mathrm{H_2}}$) and used those values to calculate the changes per reduced molecule:

$$\Delta F^{\mathrm{vib}} = \frac{F^{\mathrm{vib}}}{f} = F^{\mathrm{vib}}_{\mathrm{TFBD,ads}} - F^{\mathrm{vib}}_{\mathrm{TFBD,ads}} - F^{\mathrm{vib}}_{\mathrm{H_2}} \tag{6.12}$$

For homogenous layers of TFBQ and TFBD adsorbed on the metal surfaces, vibrations were calculated within FHI-*aims* numerically at the Γ-point for the molecules in their respective unit cell. Numerical frequency evaluations require displacing each atom in the cell separately in each direction and evaluating the forces acting on these geometries. In this work, only atoms of the molecule were considered; the metal slab was kept fixed in order to keep the computational effort tractable. The displacement was set to 0.25 pm, and evaluation of the forces acting on the atoms was set to $10^{-4}\ \frac{\mathrm{eV}}{\mathrm{Å}}$.[42]

We find that already the zero-point energy shifts the energy balance by approx. 0.43 eV and 0.38 eV for adsorption on Cu and Ag in favor of the quinone-species; including the temperature-dependence, i.e. occupying the vibrations according to Bose-Einstein statistics, has only a comparatively minor impact.

Inserting this into equation 6.11 and considering that for a constant packing density of the monolayer, the term E^{solid} is constant yielding only an energy offset that can be neglected when studying the stability of different TFBD/TFBQ mixing ratios, one obtains:

$$\gamma = \frac{1}{A}\Big(E^{\mathrm{sys}} - f \cdot (\mu_{\mathrm{H_2}} \cdot N_{\mathrm{TFBQ}} - \Delta F^{\mathrm{vib}})\Big) + const. \tag{6.13}$$

Treating hydrogen as an ideal gas, the chemical potential is related to $p_{\mathrm{H_2}}$ and T via [63]:

$$\mu_{\mathrm{H_2}}(p_{\mathrm{H_2}}, T) = \epsilon_{\mathrm{H_2}} + k_B\, T\, \ln\left(\frac{p_{\mathrm{H_2}}\, \lambda_{\mathrm{H_2}}(T)^3}{k_B\, T}\right) \tag{6.14}$$

$\epsilon_{\mathrm{H_2}}$	ground state energy of the hydrogen molecule.
$\lambda_{\mathrm{H_2}}(T)$	thermal De'Broglie wavelength.

---

[42] The corresponding calculations of the vibrational free energy were kindly performed and provided by Oliver Hofmann.

The thermal de Broglie wavelength, $\lambda_{\mathrm{H}_2}(T)$, is given as [64]:

$$\lambda_{\mathrm{H}_2}(T) = \frac{h}{\sqrt{2\pi m_{\mathrm{H}_2} k_B T}} \tag{6.15}$$

m_{H_2} .... molecular mass of the hydrogen molecule.

For each geometry of the configuration space samples then $\gamma(p, T)$ has to be evaluated.[43] Finally, the configuration which minimizes γ at a given condition (p, T) gives the most stable structure. At a given hydrogen pressure and temperature this minimum is obtained from a set of γ evaluations for each supercell geometry within the sampled configuration space. In figure 46 the corresponding lines for γ are plotted at $T = 300$ K for the investigated supercell geometries as a function of p_{H_2}. There one finds that with increased hydrogen pressure the number of chemical defects in the monolayer increases gradually.

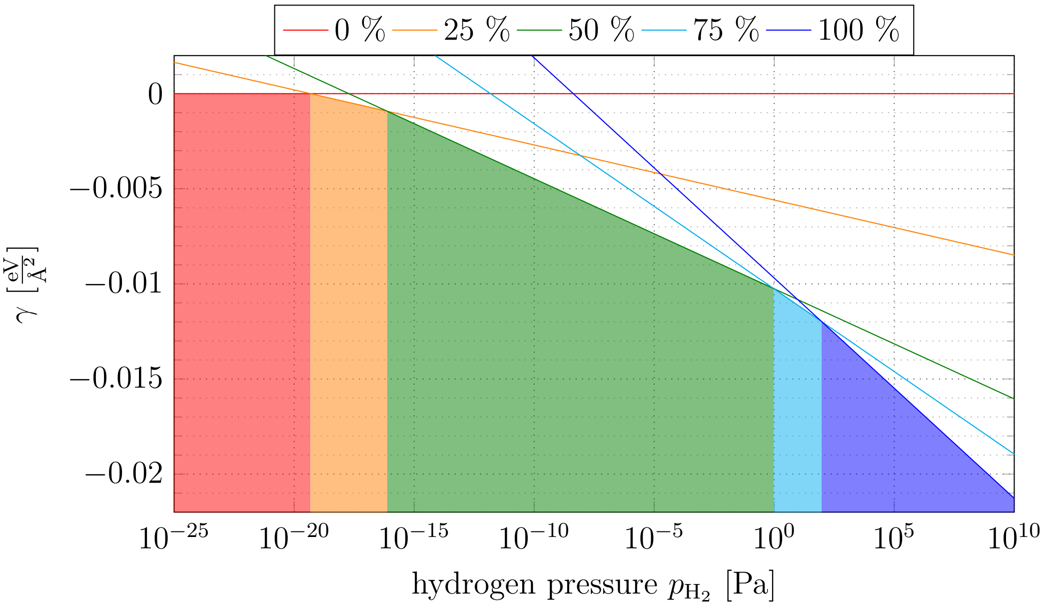

Figure 46: $\gamma(p, T = 300\ K)$ for optimized supercell geometries of mixed monolayers upon Cu(111) – the legend shows the values of f. The filled areas below the lines, separated by their intersection points indicate which geometry is preferred in thermal equilibrium, due to its minimum value of γ.

---

[43] Here we define configuration space as the manifold containing all possible alignments of the investigated system. Because it is impossible to sample the whole configuration space, one has to deal with a few probable configurations, that are (or seem) favourable for the underlying problem. For our problem those configurations are supercell geometries of hexagonal unit cells as described in chapter 6.1.

In figures 47a and 47b, we report min(γ) as surface phase diagram for Cu(111) and Ag(111). It is important to bear in mind that the outlaid thermodynamic model just describes steady state conditions. We do not and cannot make statements about reaction mechanisms or rates, or the timescale required to achieve equilibrium. In practice, to get sufficient yield from the chemical reaction, it may be necessary to activate hydrogen, e.g. through a tungsten filament or elevated temperature. Also, note that since we employed a supercell containing a finite number of molecules, f can only be varied in discrete steps. In reality, of course, a smooth, continuous change of the mixing would be expected.

For a Cu(111) surface – see figure 47a – we find that at room temperature (ca. 300 K) for hydrogen pressures up to 1 Pa $f = 50$ % is predicted. To achieve smaller f, H_2 pressures which are hardly attainable in UHV-equipment, and much less under industrial conditions, would be required. We emphasize, however, that the ratio for a given (p, T) can be adjusted by modifying the relative stability of the molecules. This can be easily achieved through chemical modification: Electron-donating groups as methyl- or hydroxyl-groups stabilize the quinone form, whereas electron-accepting substituents such as halogens stabilize the diol form – compare Streitwieser et al. [23]. If necessary, it should, therefore, be possible to modify acenequinones such that the desired mixing ratio is in a more “convenient” pressure/temperature range.

For the present system (TFBQ/TFBD), our results in fact imply that pure acenequinone layers might be thermodynamically not stable at room temperature in UHV conditions, as they will eventually be reduced by residual hydrogen gas. Increasing the hydrogen pressure to medium vacuum conditions (> 1 Pa) the TFBD fraction can be continuously changed up to $f = 100$ %. At elevated temperature, e.g. at 450 K, almost any mixing ratio, including $f = 0$ %, can be achieved with p_{H_2} ranging from UHV to atmospheric pressure. On Ag(111) configurations with larger TFBD fractions become stabilized compared to adsorption on Cu(111), due to the lower reactivity of the Ag(111)-surface. Consequently, the transition lines from $f = 25$ % to 50 % and $f = 50$ % to 75 % shift to higher temperatures and hydrogen pressures.

(a) p-T-diagram for mixed monolayers of TFBQ and TFBD on Cu(111).

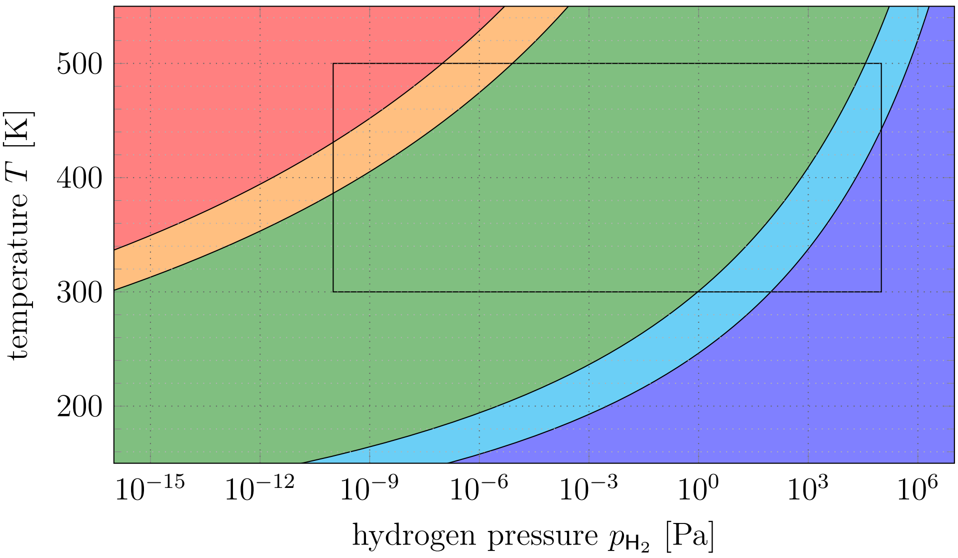

(b) p-T-diagram for mixed monolayers of TFBQ and TFBD on Ag(111).

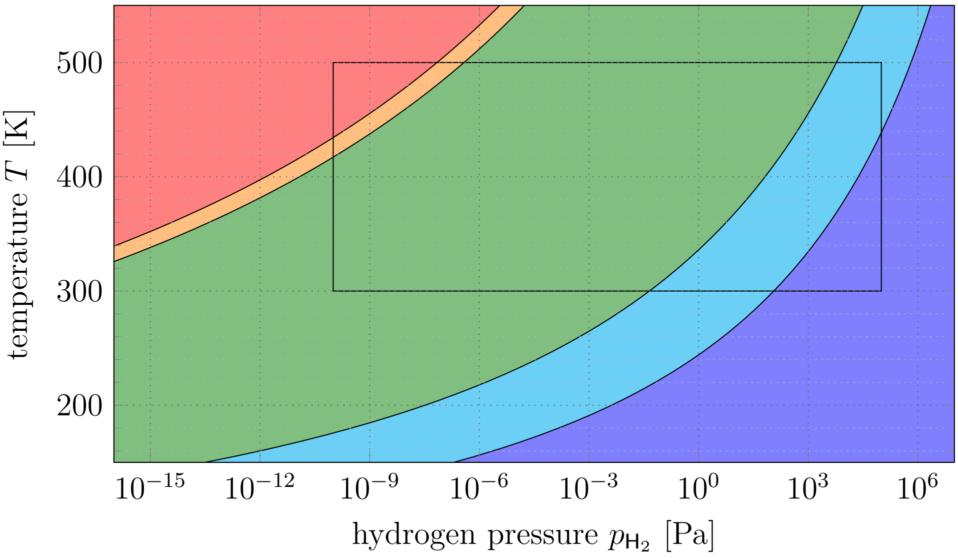

(c) Colorbar.

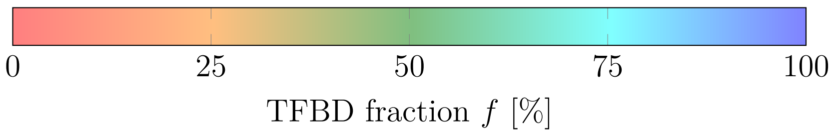

Figure 47: Contour plot of the minimum surface specific Gibbs free energy, γ, as a function of hydrogen pressure and temperature for supercells with different mixing ratios (see (c) colourbar) of mixed monolayer of TFBQ and TFBD adsorbed upon (a) Cu(111) and (b) Ag(111). The box indicates the pressure range from ultra-high to low vacuum and the temperature range from 300 K to 500 K.

7 Conclusion

Within this work we employed DFT and *ab initio* thermodynamics to study the effects of chemical defects on charge-injection barriers at metal / organic semiconductor interfaces. In particular, we focussed on interfaces with a charge-injection layer of acenequinones modifying the energy level alignment at the interface for enhanced hole injection. Due to the reversible, electrochemical reaction of acenequinones with hydrogen it suggested itself to investigate chemical defects introduced via hydrogenation.

As test system we chose mixed monolayers of TFBQ and TFBD adsorbed upon the coinage metal surfaces Cu(111) and Ag(111). We described those mixed charge-injection layers via a supercell and repeated slab approach, where the TFBQ and TFBD molecules were aligned to minimize the total energy of the system. Charge-injection barriers are approximately determined by the energy gap between the Fermi energy, E_F, and the transport levels in the organic semiconductor. Thus, we investigated two factors affecting those barriers: The electrode work function, Φ, determining E_F and the electron potential distribution above the charge-injection layer, $U(\vec{r})$, shifting the transport levels in the organic semiconductor.

Successively increasing the TFBD fraction, f, in the TFBQ charge-injection layer we found that gradual introduction of chemical defects strongly affects the energy level alignment at the interface.

By changing f from 0 to 100 % for both Cu(111) and Ag(111) Φ was modified over a range of about 1 eV. However, we found different $\Phi(f)$ dependences on the two coinage metal surfaces. On Cu(111) the work function modification $\Delta\Phi(f)$ changes nearly linearly from about $+0.5$ eV to -0.5 eV allowing a sensitive tuning of E_F with varying TFBD fraction, f. Contrary, for mixed monolayers on Ag(111) two different regimes in the course of $\Phi(f)$ are observed: Increasing f from 0 % to 50 % the work function, $\Delta\Phi$ drops from $+0.6$ eV only by about -0.1 eV. Raising f above 50 % up to 100 % a strong decrease of $\Delta\Phi$ from $+0.5$ eV to -0.3 eV sets in.

The different courses of $\Delta\Phi(f)$ for the two coinage metal surfaces were traced back to the deviating adsorption height of TFBQ in the mixed monolayers, that is about 0.4 Å higher on Ag(111) than on Cu(111). The different locations of the molecules cause that the TFBQ-LUMO is shifted differently by the dipole field of the neighboring TFBD molecules caused by Pauli pushback. As a consequence, the charge transfer to TFBQ due to Fermi-level-pinning of the LUMO and, thus, $\Delta\Phi$ is smaller with increasing f on Cu(111).

Further, we found that due to the larger spacing of the Fermi-level-pinned TFBQ molecules with increasing f the commonly invoked plate-capacitor picture for the charge rearrangements no longer describes the situation properly. With increasing f the situation rather resembles a matrix of point charges, where a potential drop above the charge-injection layer additionally modifies Φ. To underpin the point charge picture and the effects of the TFBD-potential on Fermi-level-pinning of the TFBQ-LUMO, we set up an electrostatic model where Fermi-level-pinning was simulated via a self-consistent iteration scheme. With simulation variables, suitable for the underlying systems despite the performed simplifications we obtained good agreement with the DFT-results.

From the investigations of the electron potential above the charge-injection layer, $U(\vec{r})$, we found that also the transport levels in the overlying organic semiconductor are strongly affected by the introduction of chemical defects at the interface.

Especially for small mixing ratios (i.e., very small or very high values of $f = 12.5$ % and $f = 87.5$ % we found that a strong corrugation of the electron potential above the charge-injection layer occurs. At height of $z = 8$ Å above the metal surface for instance – that is a height of about 5 Å to the charge-injection layer – the potential corrugation still is larger than 0.1 eV. However, the corrugation and, thus, the inhomogeneity of the electron potential above the surface decreases exponentially with distance to the charge-injection layer. Hence, the spacing of the first layer of the organic semiconductor to the charge-injection layer is crucial for the energy level alignment at the interface. As a consequence for organic layers with a low distance (¡ 5 Å) to the charge-injection layer with those TFBD fractions "hot spot" formation for electron and hole injection cannot be excluded.

For homogeneous monolayers of TFBQ and TFBD (i.e., $f = 0$ % and $f = 100$ %) and for equimolar mixed monolayers (i.e., $f = 50$ %) a smaller corrugation was observed. At $z = 8$ Å for those cases the corrugation was smaller than 0.1 eV. Hence, for those cases we expect a small effect on the transport levels.

We finally employed *ab initio* thermodynamics to connect the fraction of reduced molecules, f, in a mixed monolayer of TFBQ and TFBD to the hydrogen pressure, p_{H_2}, in a gas phase surrounding the electrode with the adsorbed charge-injection layer. Our calculations predict that elevated temperatures ($>$ 450 K) are necessary to obtain a homogeneous TFBQ layer in ultra-high vacuum (UHV). Increasing hydrogen pressure above UHV conditions then a continuous change of the TFBD fraction, f, to 50 % sets in. This $f = 50$ % phase then is stable until a hydrogen pressure in the medium or low vacuum regime. For pressures above that regime a continuous change to a homogeneous TFBD monolayer sets in – for 300 K $< T <$ 450 K.

This, however, does not predict the actual amount of defects in the charge-injection layer at an interface in an organic electronic device, where the electrode is not directly exposed to the atmosphere. For this case hydrogen diffusion to the interface would be the crucial factor determining the composition of the charge-injection layer. It still shows that within the deposition of the charge-injection layer on the metal electrode the hydrogen partial pressure can affect its composition, if thermal equilibrium is achieved sufficiently fast. We note that hydrogen pressure control in the deposition process may be a useful leverage for tuning of the energy level alignment at the interface, if the rate of the reaction of the charge-injection layer with a hydrogen gas phase is much higher than with hydrogen diffusing through the solid. The approach would allow continuous and reversible tuning of the charge-injection layer composition and, thus, the work function after deposition of the layer via hydrogen pressure control. Depositing further organic layers on the charge-injection layer its composition is no longer affected by the gas phase surrounding the system, but only by hydrogen diffusion through the solid.

As a next step it would be interesting to consider additional organic layers deposited on the charge-injection layer. This would allow analyzing the actual shifts of the transport levels at the interface for selected organic materials. Further, it would be interesting to investigate the dynamics of charge-injection – especially how the defect-induced corrugation of the electron potential above the surface affects charge-injection in the organic semiconductor regarding ”hot spot” formation.

We anticipate that our investigations will bring awareness for the importance of chemical defects at metal / organic interfaces and hope, thus, to contribute to more powerful organic electronic devices.

A Source Code of the Semi-Electrostatic model

```
import os;                              import numpy as np
import multiprocessing;                 from scipy import special
import matplotlib.pyplot as plt;        from matplotlib import gridspec

# Useful Constants:
Ang2Bohr = 1.889725989;               Bohr2Ang = 1.0 / Ang2Bohr;
H2eV     = 27.211396053836733;        eV2H     = 1.0 / H2eV;
eps      = 1e-10

# Simulation Parameters:
chargeNum  = 150 # the total number of point charges is (2*inNumber+1)^2
sampleNum  =  25 # number of coverage samples
pinAccNum  =  12 # number of iterations for the divide-and-conquer approach for Fermi-level-
     pinning; accuracy of charge is (1/2)^numChargeAcc
zMaxPotAcc = 1E-2

metals=['Cu', 'Ag'];
choices=['TFBQ coverage', 'TFBD coverage', 'mixed monolayer']

# Reference data from DFT-calculations for comparison:
refdata = {
  metals[0]+' '+choices[0]: np.loadtxt( os.getcwd()+'/refData/cu-cov-tfbq.txt', dtype=float,
       delimiter=',' ),
  metals[0]+' '+choices[1]: np.loadtxt( os.getcwd()+'/refData/cu-cov-tfbd.txt', dtype=float,
       delimiter=',' ),
  metals[0]+' '+choices[2]: np.loadtxt( os.getcwd()+'/refData/cu-mixed.txt',    dtype=float,
       delimiter=',' ),
  metals[1]+' '+choices[0]: np.loadtxt( os.getcwd()+'/refData/ag-cov-tfbq.txt', dtype=float,
       delimiter=',' ),
  metals[1]+' '+choices[1]: np.loadtxt( os.getcwd()+'/refData/ag-cov-tfbd.txt', dtype=float,
       delimiter=',' ),
  metals[1]+' '+choices[2]: np.loadtxt( os.getcwd()+'/refData/ag-mixed.txt',    dtype=float,
       delimiter=',' ) }

progress = 0.0

def main():
# This is the main function, which determines the simulation settings and cases and shows the
     results.

  settings = np.array( [
    # Cu(111)          Ag(111)
    ####################################
    [ 7.70*Ang2Bohr,   7.77*Ang2Bohr ], # spacing [Bohr]
    #################################### TFBQ settings:
    [ 1.05*Ang2Bohr,   1.25*Ang2Bohr ], # height [Bohr]
    [ -0.32*eV2H,      -0.32*eV2H    ], # LUMO-energy bf. ads. [Hartree]
    [ 0.40*eV2H,       0.40*eV2H     ], # FWHM of LUMO-peak [Hartree]
    [ -1.65,           -1.52         ], # backdonation [-e]
    [ 0.0,        -0.00        ], # mol Dip
    #################################### TFBD settings:
    [ 1.54*Ang2Bohr,   1.59*Ang2Bohr ], # height [Bohr]
    [ -0.15,         -0.112      ], # pushback-charge [-e]
    [ 0.32*eV2H,        0.28*eV2H      ], # max. pot. from molecular TFBD-dipole
    [ 0.0,             0.0           ], # rel. mol. dip. pot. of TFBD at TFBQ site
    ####################################
    [ 0.26,           0.06          ]  # modification of the backdonation [-e]
    ] )

  # Run simulations:
  myChoices = [
    choices[0],
    choices[1],
    choices[2]
    ]

  data={} # associative array containing the results for sub-monolayers and mixed monolayers of
       TFBQ and TFBD on Cu(111) and Ag(111)
  for metal in metals:
    for choice in myChoices:
      data[metal+' '+choice] = simulate( settings[:,metals.index(metal)], choice )

  display(data)
  plot(data)
```

```
def updateProgress():
  global progress;
  progress+=100/len(metals)/len(choices);
  print '\r'+'%6.2f' % progress+' % done ...',

def simulate( arguments, mode ):
# This function simulates the work function modification for three possible cases:
# - TFBQ coverage:     simulates Fermi-level-pinning for TFBQ-sub-monolayers
# - TFBD coverage:     simulates the Pauli-pushback-effect for TFBD-sub-monolayers
# - mixed monolayers: simulates mixed monolayers of TFBQ and TFBD, whereas the TFBD-potential
    affects Fermi-level-pinning of TFBQ
  spacing, heightQ, level, fwhm, backdon, molDipQ, heightD, chargeD, molDipD, relMolDipDatQ, CT
      = arguments
  # Reshape settings regarding coverage dependency:
  coverageQ = np.linspace(eps,1.0-eps,sampleNum+1.0);
  coverageD = 1.0-coverageQ;
  spacingQ = np.sqrt(spacing**2/coverageQ)
  spacingD = np.sqrt(spacing**2/coverageD)
  ones     = np.ones(sampleNum+1.0)
  heightQ  = ones * heightQ
  level    = ones * level
  fwhm     = ones * fwhm
  backdon  = ones * backdon
  heightD  = ones * heightD
  chargeD  = ones * chargeD

  # Create pool for multiprocessing:
  nb_cpus  = multiprocessing.cpu_count()
  pool     = multiprocessing.Pool(processes=nb_cpus)

  # Run Fermi-level-pinning or Pauli pushback simulations regarding "choice":
  backdon+=molDipQ*coverageQ
  if   mode == choices[0]: # TFBQ coverage
    zippedArgs = zip( spacingQ, heightQ, level, fwhm, coverageQ, backdon)
    results = pool.map( pinToFermiLevel, zippedArgs );
  elif mode == choices[1]: # TFBD coverage
    zippedArgs = zip( heightD, spacingD, chargeD)
    results = pool.map( pauliPushback,   zippedArgs );
  elif mode == choices[2]: # mixed monolayer
    level += molDipD*coverageD*relMolDipDatQ
    backdon += CT*coverageD; chargeD-=CT*coverageQ
    zippedArgs = zip(spacingQ, heightQ, level, fwhm, coverageQ, backdon, spacingD, heightD,
        chargeD )
    results = pool.map( pinToFermiLevel, zippedArgs );

  # When every simulation has finished, transform data in a nice format and return data:
  pool.close(); pool.join()
  data=np.array(results)
  if   mode == choices[0] or mode == choices[2]: # something with Fermi-level-pinning
    if mode == mode == choices[2]:
      data[:,2]=data[:,2]+coverageD*molDipD;
    data = np.vstack((coverageD*100.0,data[:,2]*H2eV,data[:,0],data[:,1]*H2eV))
    print mode
    print 'TFBQcov: ['+'%6.2f' % coverageQ[0]+' ... '+'%6.2f' % (coverageQ[-1]*100)+'] %'
    print 'Charges: ['+'%6.2f' % data[2,0]+' ... '+'%6.2f' % data[2,-1]+'] -e'
    print data[2,:]
    print 'Levels:  ['+'%6.2f' % data[3,0]+' ... '+'%6.2f' % data[3,-1]+'] eV'
    print data[3,:]
  elif mode == choices[1]: # just Pauli-pushback
    data = np.vstack((coverageD*100.0,(data+coverageD*molDipD)*H2eV))
  return data.transpose()

def pinToFermiLevel( arguments ):
# This function calculates the charge of the molecule by shifting the LUMO-energy in a self-
    consistent way.
# ARGUMENT:       STRUCTURE: UNIT: DESCRIPTION:
#  Spacing         float      Bohr  length of the 2D unit cell lattice vectors
#  Height          float      Bohr  point charge distance to the mirror plane
#  Level           float      H     LUMO energy relative to the Fermi level
#  Broadening      float      H     gaussian broadening of the LUMO-peak (FWHM)
#  Backdonation    float      -e    backdonation due to hydridization and pushback
  WorkFunctionModification = 0.0; argNum=6
  Spacing, Height, Level, Broadening, Coverage, Backdonation = arguments[0:argNum]
  Coords, EmptySite = calcGridWithEmptySite( Height, Spacing, chargeNum )
  itIsMixed = len(arguments) == argNum+3 # indicates mixed monolayer (MML)
  if itIsMixed: # for MML TFBD-pushback potential has to be considered
    OtherSpacing, OtherHeight, OtherCharge = arguments[argNum:argNum+4]
    OtherCoords, OtherEmptySite = calcGridWithEmptySite( OtherHeight, OtherSpacing, chargeNum )
```

```
    Level+=calcPotential( EmptySite+np.array([0,0,Height-OtherHeight]), OtherCoords, OtherCharge )
    WorkFunctionModification += calcPotentialMaximum( OtherCoords, OtherCharge )
    if Coverage>0.98: print str(itIsMixed)+' '+str(Coverage*100)+' %, '+str(H2eV*calcPotential( EmptySite, Coords, Backdonation))+' eV  '+str(Height)+' A, '+str(Backdonation)+' -e'
  # Calculate charge by Divide-And-Conquer approach:
  Charge=1.0; LowerBound=0.0; UpperBound=2.0; # initial guess and boundaries for charge
  for i in range(pinAccNum):
    Potential = calcPotential(EmptySite, Coords, Charge + Backdonation)
    NewLevel  = Level + Potential
    NewCharge = calcCharge(NewLevel, Broadening)
    if  NewCharge > Charge:
      LowerBound = Charge
      Charge = (Charge+UpperBound)/2.0
    else:
      UpperBound = Charge
      Charge = (Charge+LowerBound)/2.0
  Charge = (LowerBound+UpperBound)/2.0 + Backdonation
  WorkFunctionModification += calcPotentialMaximum( Coords, Charge );
  return Charge, NewLevel, WorkFunctionModification;

def pauliPushback( arguments ):
# This function calculates the work function modification caused by the Pauli pushback effect.
  height, spacing, charge = arguments
  return calcPotentialMaximum( calcGridWithEmptySite(height,spacing,chargeNum)[0], charge )

def calcGrid( zPosition, cellWidth, N ):
# This function calculates the cartesian coordinates of the point charges distributed on an hexagonal grid.
# ARGUMENT:    STRUCTURE:  UNIT:  DESCRIPTION:
#  zPosition    float       H      distance of the grid to the mirror plane
#  cellWidth    float       H      lattice constant of a single 2D unit cell
#  N            float       1      the total number of grid points is (2*N+1)^2
  latVec = cellWidth*np.array( [ [ 1.0,               0.0 ], \
                                 [ 0.5, np.sqrt(3.0)/2.0 ] ] )
  indices = np.arange(-N,N+1.0)
  ind1,ind2 = np.meshgrid(indices,indices)
  ind1=ind1.flatten(); ind2=ind2.flatten()
  coords=np.array( [ \
    latVec[0,0]*ind1+latVec[1,0]*ind2,\
    latVec[0,1]*ind1+latVec[1,1]*ind2,\
    zPosition*np.ones(ind1.shape) ])
  return coords.transpose()

def calcGridWithEmptySite( Height, Spacing, Number  ):
# This function calculates the coordinates of occupied point charge sites and the coordinate of an the emptied site in the middle.
  Coords= calcGrid( Height, Spacing, Number ) # coordinates of all charges
  EmptySiteInd = ((2*Number+1)**2) / 2        # index of the emptied site
  return np.delete(Coords,EmptySiteInd,0), Coords[EmptySiteInd,:]

def calcCharge( energy, fwhm ):
# This function calculates the occupation of the LUMO-peak via integration over a Gaussian function in units of [-e].
# ARGUMENT: STRUCTURE: UNIT: DESCRIPTION:
#  energy     float      H     LUMO energy relative to Fermi level
#  fwhm       float      H     full width at half maximum of the peak
  return special.erfc( energy / fwhm * 2.0*np.sqrt(np.log(2.0)) );

def calcPotential( site, sites, chargeS ):
# This function calculates the electrostatic potential for a set of point charges with corresponding mirror charges (mirror plane at z=0) in Hartree.
# ARGUMENT:  STRUCTURE:        unit   DESCRIPTION:
#  site        3x1 np.array      Bohr   coordinate for potential calculation
#  sites       3xN np.array      Bohr   with coordinates of the N point charges
#  chargeS     1x1/N np.array    -e     point charge/s
  distances = np.sqrt(np.sum((sites-site)**2,1));
  mirrorSites = np.copy(sites);
  mirrorSites[:,2] = -mirrorSites[:,2];
  mirrorDistances = np.sqrt(np.sum((mirrorSites-site)**2,1));
  return ( np.sum(chargeS/distances) - np.sum(chargeS/mirrorDistances) );

def calcMeanPotential( mySite, mySites, myCharge, boxWidth ):
  numberOfPoints=3.0;
  totalNumberOfPoints=(2.0*numberOfPoints+1)**2;
  gridSites=mySite+calcGrid( 0.0, boxWidth/np.sqrt(totalNumberOfPoints), numberOfPoints);
  averagedPotential=0.0;
  for gridSite in gridSites:
```

```
    averagedPotential += calcPotential( mySite, mySites, myCharge ) / totalNumberOfPoints;
  return averagedPotential;

def calcPotentialMaximum( sites, charge ):
# This function obtains the averaged maximum potential  above a set of charges in Hartree via a golden section search.
# ARGUMENT:  STRUCTURE:        UNIT:  DESCRIPTION:
#  sites      3xN np.array      Bohr   with coordinates of the N point charges
#  charge     1x1/N np.array    -e     point charge/s
  x=np.mean(sites[:,0]);  y=np.mean(sites[:,1]);
  zMin=max(sites[:,2]); zMax=200.0;
  goldenRatio=(np.sqrt(5)-1)/2;
  shiftedMin=zMax - goldenRatio * (zMax-zMin);
  shiftedMax=zMin + goldenRatio * (zMax-zMin);
  while abs(shiftedMax-shiftedMin)>zMaxPotAcc:
    fMin=abs(calcPotential( np.array([x,y,shiftedMin]), sites, charge ));
    fMax=abs(calcPotential( np.array([x,y,shiftedMax]), sites, charge ));
    if fMin>fMax:
      zMax       = shiftedMax
      shiftedMax = shiftedMin
      shiftedMin = zMax - goldenRatio * (zMax-zMin)
    else:
      zMin       = shiftedMin
      shiftedMin = shiftedMax
      shiftedMax = zMin + goldenRatio * (zMax-zMin)
  zOpt   = (zMin+zMax) / 2
  maxPot = calcPotential( np.array([x,y,zOpt]), sites, charge );
  return maxPot;

def display( data ):
  for content in data:
    print content
    for row in data[content]:
      print str(row[0])+', '+str(row[1])

def plot( data ):
  fig = plt.figure(figsize=(16,9)); gs = gridspec.GridSpec(1,2)
  axes = { metals[0]: fig.add_subplot(gs[0,0]), metals[1]: fig.add_subplot(gs[0,1]) }
  for metal in metals:
    axes[metal].set_ylabel('$\Delta\Phi$ [eV]');
    axes[metal].set_xlabel('$f$ / $\\theta_{TFBD}$ [%]');
    axes[metal].set_title(metal+'(111)')
  color = { choices[0]: 'r', choices[1]: 'b', choices[2]: 'k'}
  for content in data:
    metal=content[0:2]; choice=content[3:]
    print choice
    axes[metal].plot(
      data[content][:,0],data[content][:,1],color[choice]+'-',
      refdata[content][:,0],refdata[content][:,1],color[choice]+'x');
  plt.show()

if __name__ == "__main__":
  main()
```

References

[1] H. Edlbauer, O. T. Hofmann, and E. Zojer, “*Post*-Adsorption Work Function Tuning via Hydrogen Pressure Control.” Submitted to J. Phys. Chem. C at 16.09.2015, 2015.

[2] C. Wöll, ed., *Physical and Chemical Aspects of Organic Electronics.* Wiley, 2009.

[3] Y.-Q. Peng and F.-P. Lu, “Injection of Holes at Indium Tin Oxide/Dendrimer Interface: An Explanation with New Theory of Thermionic Emission at Metal/Organic Interfaces”, *Applied Surface Science*, vol. 252, p. 6275–6279, Jul 2006.

[4] N. Koch, “Organic Electronic Devices and Their Functional Interfaces”, *ChemPhysChem*, vol. 8, p. 1438–1455, Jul 2007.

[5] M. Y. Chan, S. L. Lai, M. K. Fung, S. W. Tong, C. S. Lee, and S. T. Lee, “Efficient CsF/Yb/Ag Cathodes for Organic Light-emitting Devices”, *Applied Physics Letters*, vol. 82, no. 11, p. 1784, 2003.

[6] Q. T. Le, L. Yan, Y. Gao, M. G. Mason, D. J. Giesen, and C. W. Tang, “Photoemission Study of Aluminum/tris-(8-hydroxyquinoline) Aluminum and Aluminum/LiF/tris-(8-hydroxyquinoline) Aluminum Interfaces”, *Journal of Applied Physics*, vol. 87, no. 1, p. 375, 2000.

[7] Y. Cao, G. Yu, I. D. Parker, and A. J. Heeger, “Ultrathin Layer Alkaline Earth Metals as Stable Electron-injecting Electrodes for Polymer Light Emitting Diodes”, *Journal of Applied Physics*, vol. 88, no. 6, p. 3618, 2000.

[8] A. Nakamura, T. Tada, M. Mizukami, and S. Yagyu, “Efficient Electrophosphorescent Polymer Light-emitting Devices using a Cs/Al Cathode”, *Applied Physics Letters*, vol. 84, no. 1, p. 130, 2004.

[9] S. H. Chou, J. Voss, A. Vojvodic, R. T. Howe, and F. Abild-Pedersen, “DFT Study of Atomically-Modified Alkali-Earth Metal Oxide Films on Tungsten”, *The Journal of Physical Chemistry C*, vol. 118, pp. 11303–11309, May 2014.

[10] L. Giordano, F. Cinquini, and G. Pacchioni, “Tuning the Surface Metal Work Function by Deposition of Ultrathin Oxide Films: Density Functional Calculations”, *Physical Review B*, vol. 73, Jan. 2006.

[11] C. Bock, D. V. Pham, U. Kunze, D. Käfer, G. Witte, and C. Wöll, "Improved Morphology and Charge Carrier Injection in Pentacene Field-effect Transistors with Thiol-treated Electrodes", *Journal of Applied Physics*, vol. 100, no. 11, p. 114517, 2006.

[12] B. de Boer, A. Hadipour, R. Foekema, T. van Woudenbergh, M. M. Mandoc, V. D. Mihailetchi, and P. W. M. Blom, "Tuning of Metal Work Functions with Self-assembled Monolayers", pp. 18–25, Sept. 2004.

[13] I. Campbell, S. Rubin, T. Zawodzinski, J. Kress, R. Martin, D. Smith, N. Barashkov, and J. Ferraris, "Controlling Schottky Energy Barriers in Organic Electronic Devices using Self-assembled Monolayers", *Physical Review B*, vol. 54, pp. R14321–R14324, Nov. 1996.

[14] L. Zuppiroli, L. Si-Ahmed, K. Kamaras, F. Nüesch, M. Bussac, D. Ades, A. Siove, E. Moons, and M. Grätzel, "Self-assembled Monolayers as Interfaces for Organic Opto-electronic devices", *The European Physical Journal B*, vol. 11, pp. 505–512, Oct. 1999.

[15] H. Yan, Q. Huang, J. Cui, J. Veinot, M. Kern, and T. Marks, "High-Brightness Blue Light-Emitting Polymer Diodes via Anode Modification Using a Self-Assembled Monolayer", *Advanced Materials*, vol. 15, pp. 835–838, May 2003.

[16] L. Romaner, G. Heimel, J.-L. Brédas, A. Gerlach, F. Schreiber, R. Johnson, J. Zegenhagen, S. Duhm, N. Koch, and E. Zojer, "Impact of Bidirectional Charge Transfer and Molecular Distortions on the Electronic Structure of a Metal-Organic Interface", *Physical Review Letters*, vol. 99, Dec 2007.

[17] S. Duhm, A. Gerlach, I. Salzmann, B. Bröker, R. Johnson, F. Schreiber, and N. Koch, "PTCDA on Au(111), Ag(111) and Cu(111): Correlation of Interface Charge Transfer to Bonding Distance", *Organic Electronics*, vol. 9, p. 111–118, Feb 2008.

[18] B. Stadtmüller, I. Kröger, F. Reinert, and C. Kumpf, "Submonolayer Growth of CuPc on Noble Metal Surfaces", *Physical Review B*, vol. 83, Feb. 2011.

[19] N. Koch, S. Duhm, J. Rabe, A. Vollmer, and R. Johnson, "Optimized Hole Injection with Strong Electron Acceptors at Organic-Metal Interfaces", *Physical Review Letters*, vol. 95, Nov. 2005.

[20] O. Rana, R. Srivastava, G. Chauhan, M. Zulfequar, M. Husain, P. C. Srivastava, and M. N. Kamalasanan, "Modification of Metal-organic Interface using

F_4-TCNQ for Enhanced Hole Injection Properties in Optoelectronic Devices", *physica status solidi (a)*, vol. 209, pp. 2539–2545, Dec. 2012.

[21] S. R. Marder, B. Kippelen, A. K.-Y. Jen, and N. Peyghambarian, "Design and Synthesis of Chromophores and Polymers for Electro-optic and Photorefractive Applications", *Nature*, vol. 388, pp. 845–851, Aug. 1997.

[22] G. Heimel, S. Duhm, I. Salzmann, A. Gerlach, A. Strozecka, J. Niederhausen, C. Bürker, T. Hosokai, I. Fernandez-Torrente, G. Schulze, S. Winkler, A. Wilke, R. Schlesinger, J. Frisch, B. Bröker, A. Vollmer, B. Detlefs, J. Pflaum, S. Kera, K. J. Franke, N. Ueno, J. I. Pascual, F. Schreiber, and N. Koch, "Charged and Metallic Molecular Monolayers through Surface-induced Aromatic Stabilization", *Nature Chemistry*, vol. 5, no. 3, pp. 187–194, 2013.

[23] A. Streitwieser, C. Heathcock, and E. Kosower, *Organische Chemie.* Wiley, 1994.

[24] O. T. Hofmann, G. M. Rangger, and E. Zojer, "Reducing the Metal Work Function beyond Pauli Pushback: A Computational Investigation of Tetrathiafulvalene and Viologen on Coinage Metal Surfaces", *The Journal of Physical Chemistry C*, vol. 112, p. 20357–20365, Dec 2008.

[25] P. S. Bagus, K. Hermann, and C. Wöll, "The Interaction of c_6h_6 and c_6h_12 with Noble Metal Surfaces: Electronic Level Alignment and the Origin of the Interface Dipole", *The Journal of Chemical Physics*, vol. 123, no. 18, p. 184109, 2005.

[26] E. Ito, H. Oji, H. Ishii, K. Oichi, Y. Ouchi, and K. Seki, "Interfacial Electronic Structure of Long-chain Alkane/Metal Systems studied by UV-Photoelectron and Metastable Atom Electron Spectroscopies", *Chemical Physics Letters*, vol. 287, pp. 137–142, Apr. 1998.

[27] P. S. Bagus, V. Staemmler, and C. Wöll, "Exchangelike Effects for Closed-Shell Adsorbates: Interface Dipole and Work Function", *Physical Review Letters*, vol. 89, Aug 2002.

[28] F. Jensen, *Introduction to Computational Chemistry.* John Wiley & Sons, 2006.

[29] L. H. Thomas, "The Calculation of Atomic Fields", *Math. Proc. Camb. Phil. Soc.*, vol. 23, p. 542, Jan 1927.

[30] E. Fermi, "Eine statistische Methode zur Bestimmung einiger Eigenschaften des Atoms und ihre Anwendung auf die Theorie des periodischen Systems der Elemente", *Zeitschrift für Physik*, vol. 48, p. 73–79, Jan 1928.

[31] P. Hohenberg and W. Kohn, "Inhomogeneous Electron Gas", *Phys. Rev.*, vol. 136, p. B864–B871, Nov 1964.

[32] W. Koch and M. C. Holthausen, *A Chemist's Guide to Density Functional Theory.* Wiley-VCH, 2001.

[33] W. Kohn and L. J. Sham, "Self-Consistent Equations Including Exchange and Correlation Effects", *Phys. Rev.*, vol. 140, p. A1133–A1138, Nov 1965.

[34] W. Gös, *Hole Trapping and the Negative Bias Temperature Instability.* PhD thesis, Technischen Universität Wien, Fakultät für Elektrotechnik und Informationstechnik, 2011.

[35] M. J. Frisch *et al.*, "Gaussian∼09 Revision D.01." Gaussian Inc. Wallingford CT 2009.

[36] K. Aidas, C. Angeli, K. L. Bak, V. Bakken, R. Bast, L. Boman, O. Christiansen, R. Cimiraglia, S. Coriani, P. Dahle, and et al., "The Dalton Quantum Chemistry Program System", *WIREs Comput Mol Sci*, vol. 4, p. 269–284, Sep 2013.

[37] G. Kresse and F. J., "Efficiency of Ab-Initio Total Energy Calculations for Metals and Semiconductors Using a Plane-Wave Basis Set", *Comput. Mat. Sci.*, 1996.

[38] V. Blum, R. Gehrke, F. Hanke, P. Havu, V. Havu, X. Ren, K. Reuter, and M. Scheffler, "Ab Initio Molecular Simulations with Numeric Atom-centered Orbitals", *Computer Physics Communications*, vol. 180, pp. 2175–2196, Nov. 2009.

[39] S. H. Vosko, L. Wilk, and M. Nusair, "Accurate Spin-dependent Electron Liquid Correlation Energies for Local Spin Density Calculations: A Critical Analysis", *Canadian Journal of Physics*, vol. 58, p. 1200–1211, Aug 1980.

[40] J. P. Perdew, K. Burke, and M. Ernzerhof, "Generalized Gradient Approximation Made Simple", *Physical Review Letters*, vol. 77, p. 3865–3868, Oct 1996.

[41] O. T. Hofmann, V. Atalla, N. Moll, P. Rinke, and M. Scheffler, "Interface Dipoles of Organic Molecules on Ag(111) in Hybrid Density-Functional Theory", *New J. Phys.*, vol. 15, p. 123028, Dec 2013.

[42] C. Adamo and V. Barone, "Toward Reliable Density Functional Methods without Adjustable Parameters: The pbe0 Model", *J. Chem. Phys.*, vol. 110, no. 13, p. 6158, 1999.

[43] J. Heyd, G. E. Scuseria, and M. Ernzerhof, "Erratum: "Hybrid functionals based on a screened Coulomb potential" [J. Chem. Phys. 118, 8207 (2003)]", *J. Chem. Phys.*, vol. 124, no. 21, p. 219906, 2006.

[44] J. P. Perdew and K. Schmidt, "Jacob's Ladder of Density Functional Approximations for the Exchange-Correlation Energy", *American Institute of Physics*, 2001.

[45] V. A. Parsegian, *Van der Waals Forces: A Handbook for Biologists, Chemists, Engineers, and Physicists.* Cambridge University Press, 2005.

[46] A. Tkatchenko and M. Scheffler, "Accurate Molecular Van Der Waals Interactions from Ground-State Electron Density and Free-Atom Reference Data", *Physical Review Letters*, vol. 102, Feb 2009.

[47] V. G. Ruiz, W. Liu, E. Zojer, M. Scheffler, and A. Tkatchenko, "Density-Functional Theory with Screened van der Waals Interactions for the Modeling of Hybrid Inorganic-Organic Systems", *Physical Review Letters*, vol. 108, Apr 2012.

[48] R. S. Mulliken, "Electronic Population Analysis on LCAO[Single Bond]MO Molecular Wave Functions", *The Journal of Chemical Physics*, vol. 23, no. 10, p. 1833, 1955.

[49] S. M. Sze, *Physics of Semiconductor Devices.* John Wiley & Sons, 2007.

[50] H. Ishii, K. Sugiyama, E. Ito, and K. Seki, "Energy Level Alignment and Interfacial Electronic Structures at Organic/Metal and Organic/Organic Interfaces", *Advanced Materials*, vol. 11, p. 605–625, Jun 1999.

[51] A. Natan, L. Kronik, H. Haick, and R. Tung, "Electrostatic Properties of Ideal and Non-ideal Polar Organic Monolayers: Implications for Electronic Devices", *Advanced Materials*, vol. 19, pp. 4103–4117, Dec. 2007.

[52] L. Romaner, G. Heimel, and E. Zojer, "Electronic Structure of Thiol-bonded Self-assembled Monolayers: Impact of Coverage", *Physical Review B*, vol. 77, Jan. 2008.

[53] G. Witte, S. Lukas, P. S. Bagus, and C. Wöll, "Vacuum Level Alignment at Organic/Metal Junctions: "Cushion" Effect and the Interface Dipole", *Applied Physics Letters*, vol. 87, no. 26, p. 263502, 2005.

[54] S. Braun, W. R. Salaneck, and M. Fahlman, "Energy-Level Alignment at Organic/Metal and Organic/Organic Interfaces", *Advanced Materials*, vol. 21, p. 1450–1472, Apr 2009.

[55] O. T. Hofmann, D. A. Egger, and E. Zojer, "Work-Function Modification beyond Pinning: When Do Molecular Dipoles Count?", *Nano Lett.*, vol. 10, p. 4369–4374, Nov 2010.

[56] J. Rogal and K. Reuter, "Ab initio Atomistic Thermodynamics for Surfaces: A Primer", *Modeling and Simulation of Gas-Surface Interactions for Reactive Flows in Hypersonic Flights , p 2-1—2-18, Educational Notes RTO-EN-AVT-142, Neuilly-sur-Seine2-18, Educational Notes RTO-EN-AVT-142, Neuilly-sur-Seine*, 2007.

[57] P. Herrmann and G. Heimel, "Structure and Stoichiometry Prediction of Surfaces Reacting with Multicomponent Gases", *Advanced Materials*, 2014.

[58] K. Reuter and M. Scheffler, "Composition, Structure, and Stability of RuO_2(110) as a Function of Oxygen Pressure", *Phys. Rev. B*, vol. 65, Dec 2001.

[59] G. Kresse, O. Dulub, and U. Diebold, "Competing Stabilization Mechanism for the Polar ZnO(0001)-Zn Surface", *Phys. Rev. B*, vol. 68, Dec 2003.

[60] M. Chase, J. Davies, C. J. Downey, J. D. Frurip, R. McDonald, and A. Syverud, "NIST Standard Reference Database 13."

[61] K. Reuter and M. Scheffler, "Composition and structure of the RuO_2 (110) surface in an O_2 and CO environment: Implications for the catalytic formation of CO_2", *Physical Review B*, vol. 68, July 2003.

[62] M. V. Bollinger, K. W. Jacobsen, and J. K. Nørskov, "Atomic and Electronic Structure of MoS_2 Nanoparticles", *Phys. Rev. B*, vol. 67, p. 085410, Feb 2003.

[63] D. Loffreda, "Theoretical Insight of Adsorption Thermodynamics of Multifunctional Molecules on Metal Surfaces", *Surface Science*, vol. 600, pp. 2103–2112, May 2006.

[64] W. Nolting, *Statistische Physik: mit 133 Aufgaben mit vollständigen Lösungen.* No. Wolfgang Nolting ; 6 in Grundkurs Theoretische Physik, Berlin: Springer, 6. aufl ed., 2007.

[65] C. Freysoldt, P. Eggert, P. Rinke, A. Schindlmayr, and M. Scheffler, "Screening in Two Dimensions: GW Calculations for Surfaces and Thin Films using the Repeated-slab Approach", *Physical Review B*, vol. 77, June 2008.

[66] H. Monkhorst and J. Pack, "Special Points for Brillouin-zone Integrations", *Phys. Rev. B*, vol. 13, pp. 5188–5192, Jun 1976.

[67] M. E. Straumanis and L. S. Yu, "Lattice Parameters, Densities, Expansion Coefficients and Perfection of Structure of Cu and of Cu–In α Phase", *Acta Crystallogr Sect A Cryst Phys Diffr Theor Gen Crystallogr'*, vol. 25, p. 676–682, Nov 1969.

[68] L. Schimka, R. Gaudoin, J. Klimeš, M. Marsman, and G. Kresse, "Lattice Constants and Cohesive Energies of Alkali, Alkaline-earth, and Transition Metals: Random Phase Approximation and Density Functional Theory Results", *Physical Review B*, vol. 87, Jun 2013.

[69] A. D. Mcnaught and A. Wilkinson, "IUPAC Compendium of Chemical Terminology", Jun 2009.

[70] I. Abraham, R. Joshi, P. Pardasani, and R. Pardasani, "Recent Advances in 1,4-Benzoquinone Chemistry", *Journal of the Brazilian Chemical Society*, vol. 22, no. 3, p. 385–421, 2011.

[71] S. Chowdhury and P. Kebarle, "Electron Affinities of Di- and Tetracyanoethylene and Cyanobenzenes based on Measurements of Gas-phase Electron-transfer Equilibria", *Journal of the American Chemical Society*, vol. 108, p. 5453–5459, Sep 1986.

[72] B. Kotov and V. Potapov, "Ionization Potentials of Strong Organic Electron Acceptors", *Khim. Vys. Energ.*, vol. 6, no. 375, 1972.

[73] T. Heinis, S. Chowdhury, S. L. Scott, and P. Kebarle, "Electron Affinities of Benzo-, Naphtho-, and Anthraquinones determined from Gas-phase Equilibria Measurements", *Journal of the American Chemical Society*, vol. 110, p. 400–407, Jan 1988.

[74] D. Dougherty and S. P. McGlynn, “Photoelectron Spectroscopy of Carbonyls. 1,4-Benzoquinones”, *Journal of the American Chemical Society*, vol. 99, p. 3234–3239, Mar 1977.

[75] Q. Fu, J. Yang, and X.-B. Wang, “On the Electronic Structures and Electron Affinities of the m -Benzoquinone (BQ) Diradical and the o -, p -BQ Molecules: A Synergetic Photoelectron Spectroscopic and Theoretical Study”, *The Journal of Physical Chemistry A*, vol. 115, p. 3201–3207, Apr 2011.

[76] M. Palmer, W. Moyes, M. Speirs, and J. Ridyard, “The Electronic Structure of Substituted Benzenes; Ab Initio Calculations and Photoelectron Spectra for Phenol, the Methyl- and Fluoro-derivatives, and the Dihydroxybenzenes”, *J. Mol. Struct.*, vol. 52, no. 293, 1979.

[77] J. Inukai, M. Wakisaka, M. Yamagishi, and K. Itaya, “Adlayer of Hydroquinone on Rh(111) in Solution and in Vacuum Studied by STM and LEED”, *Journal of The Electrochemical Society*, vol. 152, no. 2, p. E35, 2005.

[78] Y.-G. Kim, J. H. Baricuatro, and M. P. Soriaga, “Molecular Adsorption at Well-Defined Electrode Surfaces: Hydroquinone on Pd(111) Studied by EC-STM”, *Langmuir*, vol. 22, p. 10762–10765, Dec 2006.

[79] S. S. Batsanov, “Van der Waals Radii of Elements”, *Inorganic Materials*, vol. 37, no. 9, p. 871–885, 2001.

[80] R. Hoffmann, “A Chemical and Theoretical Way to look at Bonding on Surfaces”, *Rev. Mod. Phys.*, vol. 60, p. 601–628, Jul 1988.

[81] T. Hughbanks and R. Hoffmann, “Molybdenum Chalcogenides: Clusters, Chains, and Extended Solids. The Approach to Bonding in three Dimensions”, *Journal of the American Chemical Society*, vol. 105, p. 1150–1162, Mar 1983.

[82] G. Heimel, F. Rissner, and E. Zojer, “Modeling the Electronic Properties of π-Conjugated Self-Assembled Monolayers”, *Advanced Materials*, vol. 22, p. 2494–2513, Apr 2010.

[83] R. Stadler and K. W. Jacobsen, “Fermi Level Alignment in Molecular Nanojunctions and its Relation to Charge Transfer”, *Physical Review B*, vol. 74, Oct 2006.

[84] R. Otero, D. Écija, G. Fernández, J. M. Gallego, L. Sánchez, N. Martín, and R. Miranda, “An Organic Donor/Acceptor Lateral Superlattice at the Nanoscale”, *Nano Lett.*, vol. 7, p. 2602–2607, Sep 2007.

[85] S. J. Stranick, A. N. Parikh, Y.-T. Tao, D. L. Allara, and P. S. Weiss, “Phase Separation of Mixed-Composition Self-Assembled Monolayers into Nanometer Scale Molecular Domains”, *The Journal of Physical Chemistry*, vol. 98, p. 7636–7646, Aug 1994.

[86] B. Stadtmüller, D. Lüftner, M. Willenbockel, E. M. Reinisch, T. Sueyoshi, G. Koller, S. Soubatch, M. G. Ramsey, P. Puschnig, F. S. Tautz, and et al., “Unexpected Interplay of Bonding Height and Energy Level Alignment at Heteromolecular Hybrid Interfaces”, *Nature Communications*, vol. 5, Apr 2014.

[87] F. Rissner, D. A. Egger, L. Romaner, G. Heimel, and E. Zojer, “The Electronic Structure of Mixed Self-Assembled Monolayers”, *ACS Nano*, vol. 4, p. 6735–6746, Nov 2010.

[88] P. S. Bagus, D. Käfer, G. Witte, and C. Wöll, “Work Function Changes Induced by Charged Adsorbates: Origin of the Polarity Asymmetry”, *Physical Review Letters*, vol. 100, Mar. 2008.

[89] O. L. A. Monti, “Understanding Interfacial Electronic Structure and Charge Transfer: An Electrostatic Perspective”, *The Journal of Physical Chemistry Letters*, vol. 3, pp. 2342–2351, Sept. 2012.